

Università degli Studi di Perugia
Dottorato di Ricerca in Fisica e
Tecnologie Fisiche
XXV Ciclo



**Silicon pixel detectors
for high precision
measurements**

Candidato:
Stefano Meroli

Relatore

Dott. Leonello Servoli

Cordinatore del corso di Dottorato:

Prof. Maurizio Busso

A.A. 2011/12

Contents

Introduction	1
Chapter 1. Pixel Detectors for Ionizing Particles	3
1.1 Motivation for Pixel Detectors	4
1.2 Working principle of silicon Pixel Detector	5
1.3 Hybrid Pixel Detectors	7
1.4 Monolithic Active Pixel Sensors	10
1.5 Vertical Scale Integration	13
Chapter 2. Interaction of radiation with matter	17
2.1 Passage of charged massive particles through matter	17
2.1.1 Cross section	18
2.1.2 Mean energy loss for massive particles.....	19
2.1.3 Correction to Bethe-Bloch for electrons and positrons	21
2.2 Energy straggling	21
2.2.1 Thick absorber.....	22
2.2.2 Thin absorber.....	23
2.2.3 Energy straggling for electrons and positrons	26
2.2.4 Energy for charge carrier generation in semiconductor material	26
2.2.5 Radiation length	27
2.3 Multiple Coulomb scattering	27
2.4 The interaction of photons	28
Chapter 3. CMS Hybrid Pixel Detectors	33
3.1 Pixel Barrel Modules.....	34
3.1.1 The sensor	35
3.1.2 The High Density Interconnect.....	35

3.1.3 The read-out chip.....	35
3.2 Test setup	36
3.3 Functionality analysis of CMS pixel sensor.....	37
3.4 Sensor absolute calibration of the CMS pixel sensor	39
3.5 Charge particle response for CMS pixel sensor	40
Chapter 4. Radiation Active Pixel Sensor RAPS03	43
4.1 The ESAS and ESAL pixels	44
4.2 The RAPS03 data acquisition system	44
4.2.1 Requirements of the Digital Acquisition System	45
4.2.2 DAQ architecture overview	46
4.2.3 Mechanics.....	48
4.2.4 Software	48
4.2.5 Firmware	49
4.3 Noise analysis	50
4.3.1 Fixed pattern noise FPN	50
4.3.2 Signal pixel noise	52
4.4 X-ray response of the ESAS and ESAL matrix.....	55
4.4.1 Sensor absolute calibration of the ESAS matrix	55
4.4.2 Sensor absolute calibration of the ESAL matrix	59
4.5 Charge particle response for ESAS and ESAL matrix	62
4.5.1 Behavior of the ESAS matrix exposed to high energy electron beam	63
4.5.2 Behavior of the ESAL matrix exposed to high energy electrons beam	64
4.6 Spatial resolution and detection efficiency	65
4.6.1 Beam test setup.....	68
4.6.2 Spatial resolution measurement	69
4.6.3 Detection efficiency measurement.....	70
Chapter 5. Commercial CMOS Active Pixel Sensor.....	73
5.1 Noise analysis of Micron MT9V011	74
5.2 Sensor characterization with calibrated x-ray sources	76
5.3 Sensor absolute calibration.....	79
5.4 Charge particle response for MTV9V011 sensor.....	80
Chapter 6. Vertical integration technologies for Pixel Detectors	84
6.1 The two-layer 3D CMOS APS detector.....	85

6.2 Simulation activity	85
6.3 Functional characterization.....	87
6.4 Signal to noise evaluation: x-rays analyses.....	88
6.5 Charge particle response for the RAPS04 sensor	90
Chapter 7. Precision physics measurements with silicon Pixel Detectors	94
7.1 The grazing angle method	94
7.1.1 Grazing angle method for charge collection efficiency measurements.....	98
7.1.2 Grazing angle method for the sensitive region thickness measurement.....	105
7.1.3 Grazing angle method for energy loss measurement	106
7.1.4 Grazing angle method for spatial resolution measurements	110
Conclusion	116

Introduction

The research carried out during the three years of my Ph.D. course has been focused on solid-state radiation sensors, and more precisely on silicon pixel detectors. Pixel based sensors offers several advantages over the more traditional silicon microstrips or other position sensitive detectors, among which the inherently 2-D coordinate measurement that, joined with the small sensitive volume, leads to a true 3-D point in space. The pixel size could also be reduced to reach small intrinsic spatial resolution values (order of micron or less). The subject of my activity has been the characterization, through the development of innovative methodologies and instruments, and design and optimization of different flavors of pixel sensors, read-out by standard CMOS technology, either as a separate chip than integrated on the same silicon substrate of the sensing element, for the detection of different types of ionizing radiation.

Several classes of sensors have thus been studied, from the well known Hybrid Pixel Detectors, to the CMOS Active Pixel Sensors, to the modern many-tiers pixel detectors developed using a 3D Vertical Scale Integration technology. Complex test setups have been developed as well as dedicated algorithms to extract the important parameters of each sensor, among which Equivalent Noise Charge, Signal to Noise ratio for Minimum Ionizing Particles, detection efficiency and spatial resolution.

A modified grazing angle method with medium energy charged particle beams (i.e. few hundreds MeV electrons) has been developed to probe deeply the sensor characteristics, opening the possibility to carry out precision measurements of the interaction between ionizing radiation and matter, and of physical processes with unprecedented accuracy. Applying this technique some electronic properties of silicon pixel detectors have been measured, like diffusion coefficient, carriers lifetime and charge collection efficiency profiles.

Chapter 1.

Pixel Detectors for Ionizing Particles

Advances in particle tracking have always lead to breakthroughs in experimental methods and hence to a new quality of experiments. A prominent example of this statement is the Nobel-awarded invention of the multi-wire proportional chamber by G. Charpak in 1968 [1.1, 1.2], which for the first time allowed the electronic detection of particle tracks to an accuracy in the order of a mm and below. Later (~1975) spatial resolutions in the order of $100\mu\text{m}$ were obtained with drift chambers. These detectors typically had a read-out density of $0.05\text{ channels/cm}^2$. So called vertex drift chambers improved the resolution of such chambers down to about $50\mu\text{m}$ with a read-out density of 0.1 channels/cm^2 . These devices enabled the detection of decay vertices, and hence measurements of the lifetimes of long lived (~ picoseconds) particles. Silicon microstrip detectors were developed in the early eighties [1.3]. With this new type of detectors, spatial resolutions in the order of $10\mu\text{m}$ became accessible for the first time. The identification of secondary vertices and hence of particle lifetimes became precision measurements. These devices had a channel density of the order of 100 channels/cm^2 . Pixel detectors [1.4], finally, belong to this category of instruments leading the way to a new frontier in measurement techniques and hence in physics. At the Large Hadron Collider (LHC), close to the interaction point, no other detector instrument is capable to cope as well with the high density and rate of particle tracks and stand the fierce radiation environment. Pixel detectors return true three-dimensional space points, a necessity for pattern recognition and tracking in the LHC environment near the interaction point. The channel density increases by more than an order of magnitude compared to strip detectors to about $5000\text{ channels/cm}^2$. Fast read-out of such a large (in terms of channels) and complex system required new technologies and methods, which have been developed during the past decade.

1.1 Motivation for Pixel Detectors

The term *pixel detector* describes devices with the detector elements subdivided into an array of independent cells. Each segmented electrode is called a pixel. This term stands for a picture element and historically was reserved for imaging devices in the visible light spectrum. Pixel devices, delivering true two-dimensional pictures, are of great interdisciplinary importance, including scientific applications and consumer electronics products. The variety of pixel devices, given the sensitivity of silicon for visible light, is the core of the huge commercial market for camcorders and other electronic image capture devices.

In particle tracking, pixel detectors are best suited to provide high granularity and unambiguous particle track reconstruction. Pixel detectors, so far used as vertex detectors in High Energy Physics (HEP), employ silicon sensors in the form of Charge Coupled Devices (CCDs) and Hybrid Pixel Detectors (HPDs). CCDs for charged particle tracking are closely related to those used in video cameras while HPDs are application-specific variants being developed particularly for the LHC experiments as elements of vertex detectors being compatible with very high track densities and with harsh radiation environment. Both types of detectors require separate front-end electronics, which has an important impact on some of their performance parameters, e.g. in terms of read-out speed, amount of material traversed by particles, fabrication yield, etc.

Pixel detectors are generally classified as passive and active sensors. Active pixel sensors are those equipped individually with a first stage of signal amplification integrated directly within the pixel area. This approach is advantageous since it makes it possible to perform some processing operations independently on each pixel before signals are transferred to the common processing blocks placed on the periphery of the detector or to the external off-detector units. In the case of passive pixel sensors, the pixels provide only charge collection capability and the sensed charge needs to be transferred through the common read-out lines to the processing circuitry placed outside the area of the pixel array.

The part sensitive to radiation, i.e. the detector, and the read-out electronics can be processed separately on different substrates, which are connected together during the whole detector system assembling. The front-end electronics and the pixel detector are fully separated in the case of HPDs. The full integration of the read-out electronics and the detector is only achieved for monolithic pixel detectors. In this case, both components are fabricated using a planar process, for which all steps are carried out on the same substrate. Most implementations of pixel-based detectors feature extremely low values of the detector capacitance, seen at the input of the read-out electronics, enabling low noise operation of the first stage amplifier, allowing even with much smaller signals, a satisfactory SNR. An efficient detection capability is possible exploiting active layers 20 times thinner than the typical thickness of 300 μm . Formerly, in using devices

with thin active layers, it was habitual to leave them mechanically thick. Recently, thinned devices are proposed for HEP detectors taking advantage of the development of etching techniques and handling of such thin structures. This approach will result in a significant reduction of multiple scattering improving the tracking performance.

Pixel detectors offer granularity several orders of magnitude higher than a typical microstrip detector. This may accept higher hit densities before effects related to ambiguous hit position reconstruction and cluster merging starts to affect the track reconstruction algorithm. For this reason, pixel-based vertex detector planes can be placed much closer to the interaction point, resulting in much better precision of event reconstruction.

Radiation hardness is also in favor of a pixel detector with respect to microstrip detectors. For long-strip detectors, the limiting parameter is the increase of the shot noise due to the increased leakage current after irradiation. In this case, the signal can be overwhelmed by noise. On the other hand, for pixel detectors the “strip length” is reduced by about two orders of magnitude. Thus, the noise associated with the leakage current is correspondingly reduced making pixel detectors useful for application where extremely hostile radiation conditions prevail.

Certain future applications, and their experimental conditions lead to demanding design requirements. A possible solution consists in integrating the detecting elements with the front-end electronics on the same silicon substrate using standard, easily accessible CMOS processes used for fabrication of integrated circuits [1.5, 1.6]. Devices following this principle have been yet proposed for commercial use for still photography and video applications at the beginning of 90’s. They are called CMOS Active Pixel Sensors (APS). Originally, their performance lagged behind those of CCDs, however, after many improvements during recent years, they serve now as cheap and powerful solutions for imaging systems and become viable competitors for CCDs.

1.2 Working principle of silicon Pixel Detector

In the previous section the pixel detector has been introduced in quite general terms. In this section some details on the operation of silicon pixel detectors are given in order to provide the minimal tools for the discussion of pixel detectors and their applications. To describe the operation of a silicon pixel detector one may consider a 300 μm -thick n-doped (i.e. doped with the addition of a pentavalent impurity, like phosphorus) silicon wafer assuming that each pixel is a p-implant (i.e. doped with a trivalent impurity, like boron). The doping must be such as to largely overcome the intrinsic carrier densities in silicon at room temperature ($\approx 10^{10} \text{ cm}^{-3}$) and will therefore determine the abundance of free electrons (holes) in the

n-zone (p-zone). The resistivity ρ of doped silicon depends only on the dopant density N and on the majority carrier mobility μ according to

$$\rho = \frac{1}{eN\mu} \tag{1.1}$$

where e is the elementary charge. The interface region between the n-doped and the p-doped regions will be emptied of free charges through the following mechanism: the majority carriers in each region will diffuse through the junction and recombine with the opposite sign charge carriers. This will generate an electric field due to the excess charge from the immobile doping atoms, which counterbalances the diffusion and establishes an equilibrium. This equilibrium, characterized by the absence of charges which can move freely, extends to some thickness W (depletion zone), which depends on the dopant concentration N of the lower doped bulk material and on the voltage V across the junction according to

$$W = \sqrt{2\epsilon_0\epsilon_{Si}(V/eN)} = \sqrt{2\epsilon_0\epsilon_{Si}(V\mu\rho)} \tag{1.2}$$

Charges are built up on both sides of the junction and therefore the depletion zone can be seen as a charged capacitor of value C per unit area:

$$C = \epsilon_0\epsilon_{Si}/W = \sqrt{\epsilon_0\epsilon_{Si}N/2V} \tag{1.3}$$

Increasing the reverse bias voltage V increases the thickness of the depletion zone and reduces the capacitance of the sensing element, and both these effects increase the signal to noise ratio (SNR). Fully depleted detectors (i.e. those with the depletion zone extending to the whole thickness of the silicon layer) will give the best SNR.

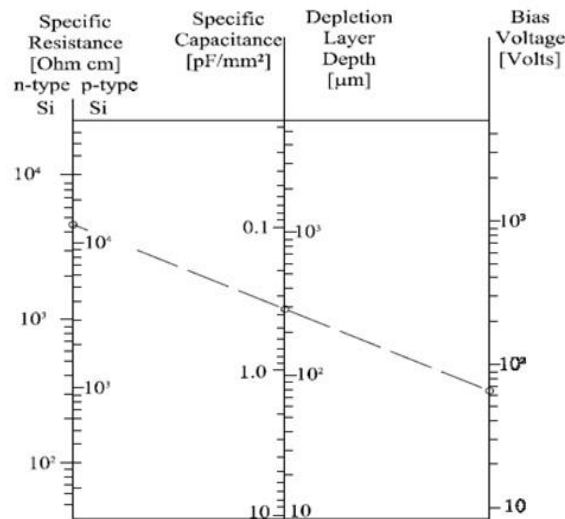


Figure 1.1 Nomogram showing relations between the most important parameters for silicon junction detectors operation.

The nomogram shown in Figure 1.1 correlates most of the parameters which have been discussed so far. Any straight line in the Figure 1.1 correlates the values of the different parameters (elaborated from [1.7]). A 300 μm -thick n-type silicon substrate with p-implants is a set of pn junctions which act as independent diodes. If these diodes are reversely polarized, e.g. applying a positive voltage on the n-side and connecting each p-implant to ground through its read-out amplifier, very little current flows through them. The majority carriers experience a barrier due to the externally applied voltage. The minority carriers (holes in this example) are constantly removed out of the depleted region by the field in the junction, thus generating a small current, known as dark current. As the carriers are thermally generated, this current depends on temperature and is also known as thermal background current.

Particles crossing the silicon detector, or photons absorbed in it, generate charged carriers (on average 1 electron-hole [e-h] pair per 3.68eV of energy deposited). If these carriers are generated in the depletion zone, they lead to a current signal much larger than the thermal background current and which is therefore detectable. The depletion zone hence constitutes the active volume of the detector. In the undepleted regions, on the contrary, there is too low an electric field to collect charges in a short time and too many majority carriers which facilitate charge recombination.

To understand how this current is generated and how it can be detected, the case of a relativistic particle crossing the 300 μm -thick silicon detector is considered. The particle loses energy through many collisions with the electrons of the crystal and generates in 300 μm -thick silicon detector ≈ 80 e-h pairs per micrometer of path in a few micrometer wide cylinder around its trajectory. These charges drift under the action of the external electric field at a speed which depends on the electric field but saturates at values $\approx 10^7$ cm/s for fields close to 10^4 V/cm. The charges are therefore collected in less than 10ns, resulting in a current of about $0.5\mu\text{A}$. During the drift the charges do not exactly follow the electric field-lines, but diffuse as a consequence of the random thermal motion in the crystal lattice. Spread of the arrival position of the charge due to this effect can be described as a Gaussian distribution with standard deviation

$$\sigma = \sqrt{2Dt} \tag{1.4}$$

which results in a spread of a few micrometers at the collecting electrode, assuming a typical electron diffusion constant of $36\text{cm}^2/\text{s}$ and a transit time of the carriers of 10ns. The diffusion constant is higher for electrons than for holes, as it scales with the mobility.

1.3 Hybrid Pixel Detectors

The intensive growth of the Hybrid Pixel Detectors (HPDs) was initiated and is still driven by the development for the LHC detectors, where very fast and radiation hardened devices are required [1.8]. The

fabrication of this type of pixel sensor is very similar to the fabrication of a microstrip sensor. In the pixel case the implants have a higher segmentation. This simple change of the sensor design has many consequences at the system level and offers a variety of applications. The detector part consists essentially of a microstrip detector structure, each strip being subdivided into some number of short pieces, which constitute the pixels. The sensor array and the matching read-out chip are processed independently and are connected together only in the final step. In this way the material and processes can be individually optimized for the actual purpose i.e. detector and electronics. This approach makes it possible to achieve fast enough read-out and radiation hardness compatible with the LHC environment. The detector substrate is high resistivity silicon, although other materials than silicon, e.g. diamond, are also considered.

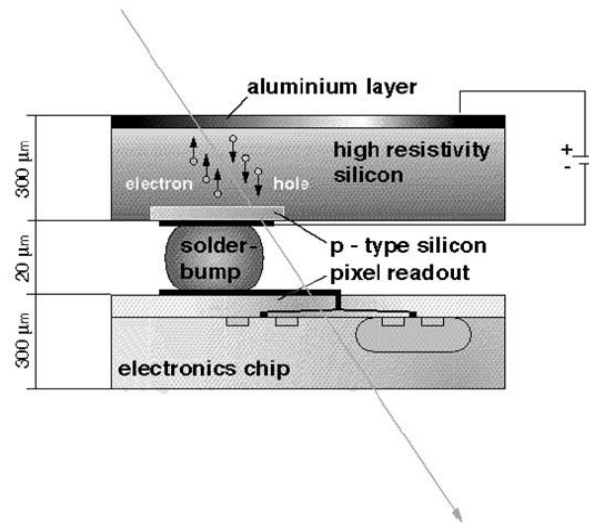


Figure 1.2 Sketch of a “blown-up” hybrid pixel detector

The read-out electronics is built in an industrial CMOS foundry and it can be similar in architecture to the classical front-end topology for microstrip detectors. The connection of the detector and the read-out electronics is customarily done by means of the flip-chip bonding technique, where small balls of solder, indium or gold, establish the electrical and mechanical connection between each detection element and its read-out circuit.

The two-dimensional high-density connectivity is the key characteristics of the hybrid pixel detector and has three main consequences that are illustrated in Figure 1.2:

- The connectivity between the sensor and the mating read-out chip must be vertical;
- There must be exact matching between the size of the pixel and the size of the front-end electronics channel;
- The electronics chip must be very close (10-20 μm) to the sensor.

As shown in paragraph 1.2, the operation of the HPDs obeys to Eq. (1.2), (1.3), and (1.4), but constraints which result from the topology of the assembly must be considered too. To deplete the sensor a sufficiently high bias voltage must be applied on the backside plane while all the pixels are grounded.

Any electronics chip must have some ancillary logic to extract the signal from the front-end channels, organize the information, and transmit it out. This logic cannot be distributed to all pixel cells, but has to be concentrated and is normally placed close to one edge of the chip.

Since the chip is very close to the sensor, designers must pay special attention to avoid the following:

- Large static voltage (i.e. bias voltage) on the front side or on the edge of the sensors that may give rise to destructive sparks. This implies that the guard ring structure which helps to confine the high-voltage region should be on the backside of the sensor.
- Large high-frequency signals on the electronics that may induce detectable signals on the pixel metallization. This implies using low swing logic signals (e.g. LVDS) and minimizing the coupling capacitance between the sensor and the digital busses.

HPDs have the disadvantage of high complexity of millions of interconnections and they introduce extra material in the active area. Moreover, HPDs are characterized by the relatively high power dissipation reaching a few hundred mW/cm^2 and relatively large size of a single cell needed to integrate required complex functionality of the read-out circuitry.

Other peculiar characteristics of the pixel detectors are related to the small dimensions of the sensing elements. Each pixel covers, in fact, a very small area ($\approx 10^{-4}\text{cm}^2$) over a thin ($\approx 300\mu\text{m}$) layer of silicon. It therefore exhibits a very low capacitance ($\approx 0.2 - 0.4\text{pF}$), which is dominated by the coupling to the neighboring pixels rather than to the backside plane. The low capacitance is one of the key advantages of pixel detectors since it allows fast signal shaping with very low noise. It is common to obtain single pixel noise of about 200e for electronics operating at 40MHz and therefore an SNR exceeding 100 for fully depleted 300 μm -thick sensors. This is a very comfortable situation as it allows operation in absence of spurious noise hits. A detection threshold set at, e.g., 10σ noise, gives in fact full efficiency and very low probability that a noise fluctuation exceeds the threshold. This may be looked at as a very idealized situation as other sources of fake hits could be conceived (e.g. electronics pickup, cross talk, low-energy photons), but measurements [1.9] prove that a spurious hit probability of $<10^{-8}$ per pixel can be reached under experimental conditions. Another way of taking advantage of the excellent SNR is to consider that the detector is robust enough to tolerate even a considerable signal loss.

This extends the application of the hybrid pixel detector in two directions:

- To sensors which have a poor charge collection or a limited active thickness (e.g. diamond, GaAs, Cd(Zn)Te);
- To crystalline silicon sensors damaged by high irradiation flux.

In the latter case the collected charge is diminished through two effects: the trapping of drifting carriers due to radiation-induced defects in the crystal lattice and the reduction of the depletion depth due to the increase of the space charge [1.10].

Finally, smallness of the pixel means smallness of the reverse current flowing through it at depletion (typically $0.1\mu\text{A}/\text{cm}^2$). This reduces the parallel noise and allows operation even after considerable irradiation. After 10^{15} particles per square centimeter the reverse current density increases to $\approx 30\mu\text{A}/\text{cm}^2$, rendering large sensing elements difficult to operate. In summary, the HPD is the ideal detector to work in the very hostile environment which exists close to the interaction region of a particle accelerator because:

- It is radiation hard (i.e. it survives at high fluence of particles);
- It provides nonambiguous three-dimensional measurements with good time resolution;
- It provides the space resolution which is needed to measure short-lived particles.

HPDs have been shown to work in particle physics experiments [1.11, 1.12]. This success has triggered the design and the construction of detectors approaching few square meters of sensitive area and 100 millions of channels [1.13-1.15] to be operated in intense particle fluxes. Freedom in the choice of the sensitive material has also favored the application of HPDs in other fields, like medical diagnostics [1.16, 1.17].

1.4 Monolithic Active Pixel Sensors

Monolithic Active Pixel Sensors (MAPS) constitute a novel technique for silicon position sensitive detectors. The sensors are fabricated in a standard CMOS process used for modern integrated circuits manufacturing. The baseline architecture of the proposed device is similar to a visible light CMOS camera, emerging recently as a substantial competitor to standard CCDs for digital photography and video applications [1.18]. The new element, distinguishing MAPS from classical detectors on a fully depleted and high resistivity substrate, is the charge collection achieved from a lightly doped undepleted epitaxial layer used as the active volume. The signal sensed in the MAPS detector is a current pulses induced on pixel electrodes, quite small in amplitude and of short duration. The current is induced on some number of the adjacent pixels, which are closest to the particle impact point. The current is integrated on a collection diode producing a voltage drop whose magnitude depends on the distance between a given pixel and the impact point. The total amount of charge available from a single event depends on the thickness of the epitaxial layer. The charge liberated in the highly doped substrate, on which the epitaxial layer is grown, is mostly lost due to fast recombination of carriers. However, some fraction of this charge diffusing from the substrate to the epitaxial layer can still be collected.

The design and fabrication of MAPS follows the developments in microelectronic industry. The current trends, related to scaling down the technology feature size, are to reduce also the thickness of the epitaxial layer. This translates into less charge, which can be collected but is particularly compensated by the good noise performance. The epitaxial layer is available in numerous modern CMOS VLSI processes, featuring twin tubs, where it is grown on a highly, usually p++ type doped substrate.

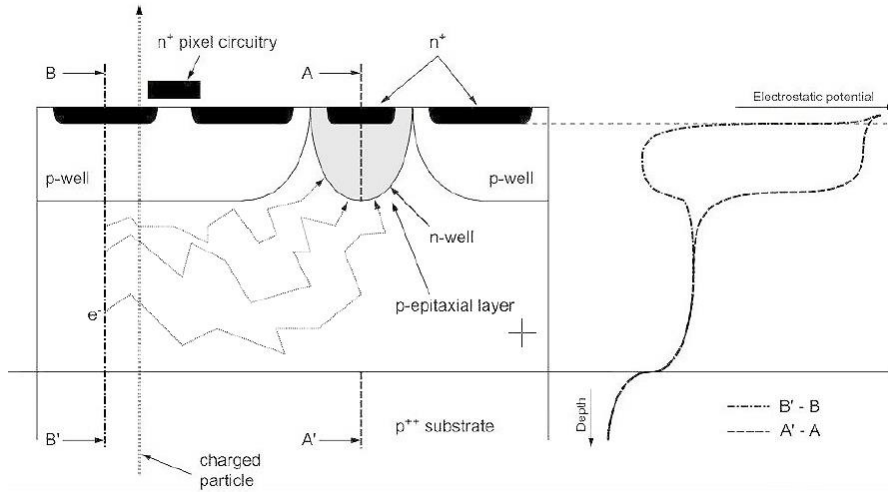


Figure 1.3 Sketch of the structure of MAPS for charged particle tracking. The charge-collecting element is a floating n_{well} diode on the p -type epitaxial layer. Because of the difference in doping levels (about three orders of magnitude), the p_{well} and the p^{++} substrate act as reflective barriers and the generated electrons can be collected by the $n_{\text{well}}/p_{\text{epi}}$ diode.

The principle of this new structure is sketched in Figure 1.3. This figure shows the cross section through the wafer sandwich-like structure composed of the substrate, the epitaxial layer, the n_{well} and p_{well} . Another information in Figure 1.3 is the distribution of the electric potential with its minimum in the region of the n_{well} . Since, there is no strong electric field, the charge carriers, generated after the impact, diffuse at thermal velocities towards the collecting diodes. In the new device, the charge generated by the traversing particle is collected by the $n_{\text{well}}/p_{\text{epi}}$ diode, created by the floating n_{well} implantation reaching the epitaxial layer. This structure forms a potential well that attracts electrons. The active volume, i.e. epitaxial layer, is underneath the read-out electronics allowing a 100% fill factor, as required in tracking applications. One constraint of the proposed approach is the limitation of the design at the pixel level to NMOS transistors only, whereas both types of transistors are used at the chip periphery. This is a consequence of the use of n_{well} implantation areas for the collecting diodes.

In the last years even more MAPS were fabricated using a non epitaxial layer and relatively high resistivity substrate [1.19]. In this case a supporting silicon wafer is uniformly p -type doped and is directly used for n_{well} and p_{well} implantations (twin-tub process). There is no potential barrier in the bulk, therefore a larger charge spread is expected. Hence, contrary to what happens when an epitaxial substrate is present, the sensitive region has no clear limit in depth and this effect increases the total amount of charge collected in the $n_{\text{well}}/p_{\text{sub}}$ diode, potentially compensating for a larger charge spread.

In Figure 1.4 it is shown the cross section of silicon wafers used for the fabrication of CMOS monolithic pixel sensors. On the left, the structure of epitaxial type wafer is shown. On the right the non-epitaxial, high resistivity wafer is presented.

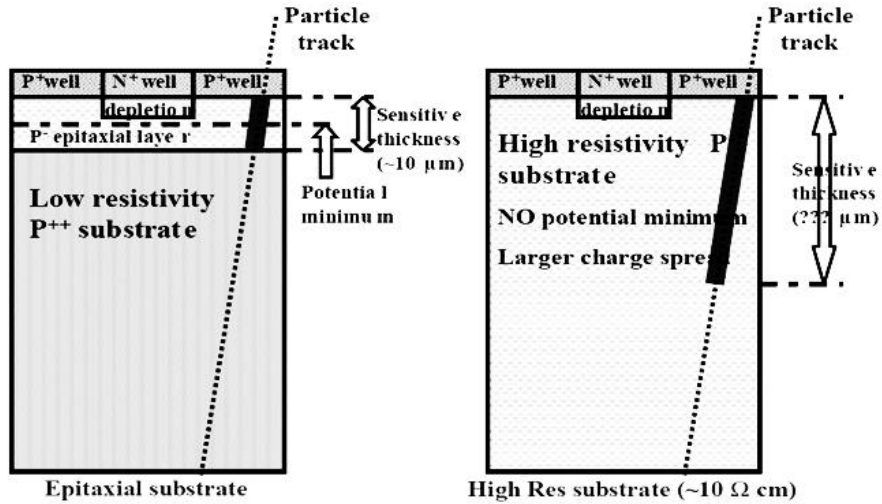


Figure 1.4 Cross section of silicon wafers used for the fabrication of CMOS monolithic pixel sensors. On the left, the structure of epitaxial type wafer, on the right the non-epitaxial type with high resistivity wafer.

The basic single cell read-out architecture of a MAPS detector is shown in Figure 1.5(a). The transistor M_{rst} resets the diode to the reverse bias, the transistor M_{sel} is a row switch, and while the transistor M_{sf} constitutes one part of the source follower. The current source for the source follower and the column selection switch are located outside the pixel. Such a pixel configuration provides capability of continuous charge integration within time between two consecutive reset operations. The small size of a single pixel, which contains in the basic configuration only the charge collecting diode and three transistors used for signal read-out, allows assembling active arrays with a tight read-out pitch of $20\mu\text{m}$ or less.

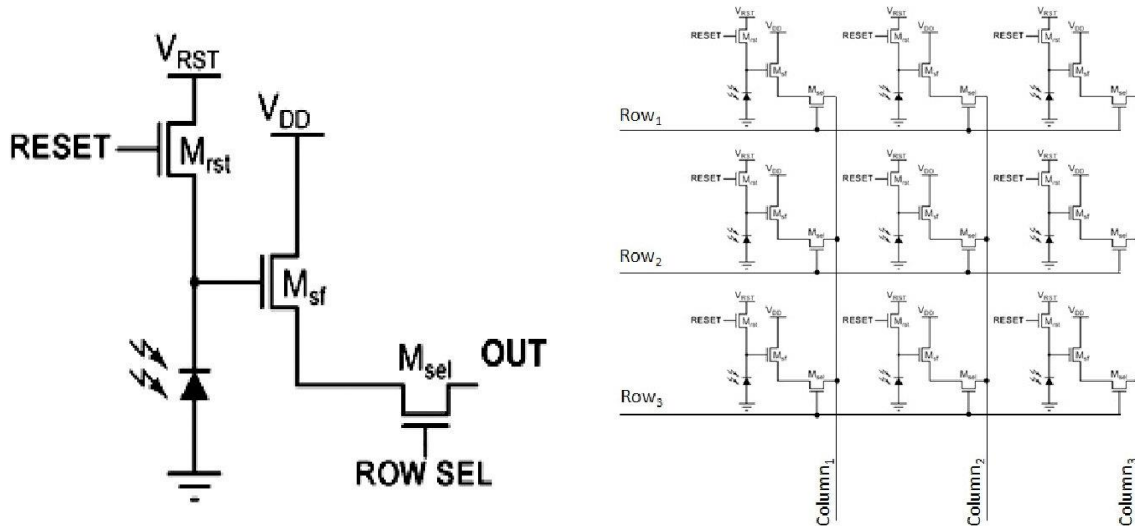


Figure 1.5 (a) Electrical scheme of a standard three transistor APS, and (b) a simple 3x3 pixels matrix.

In Figure 1.5(b) a simple 3x3 pixels matrix is presented. After noise optimization, taking into account the actual working conditions, i.e. read-out frequency and single pixel sampling, equivalent noise charges of below $10e$ are achievable even for operation at room temperature. The compact layout in combination with the measured high SNR results in a very good spatial resolution as required by new HEP experiments. The

device can also eventually be thinned down to very small thickness ($\sim 100\mu\text{m}$ or less) in order to reduce multiple scattering. After production the device is ready to be used without any complicated and expensive post processing bump-bonding.

Another important characteristic of the MAPS detectors is low power operation, which is achieved by the activation of the circuitry in each pixel only during the read-out and, contrary to CCDs, there is no power dissipation due to high frequency clock signals driving large capacitances.

1.5 Vertical Scale Integration

Detectors for particle tracking can be revolutionized by 3D-IC technology [1.20]. The advantage of this approach is that different 3D-IC vertical levels (called tiers) can be individually manufactured and optimized, by independently fabricating 2D process, and then bonded together after precise alignment and thinning and interconnecting them through deep metal vias known as through silicon vias (TSV).

Theoretically, heterogeneous wafers, i.e., from different foundries or even different process families may be combined, optimally distributing tasks like photon sensing, analog amplification, and digital processing. The sensor layer may be tailored specifically to the needs dictated by the radiation to be detected. Factors affecting sensor optimization include material, pixel granularity, and the choice of front or back side illumination. Each pixel can then be equipped with read-out electronics comprising tens or hundreds of transistors distributed on separate tiers.

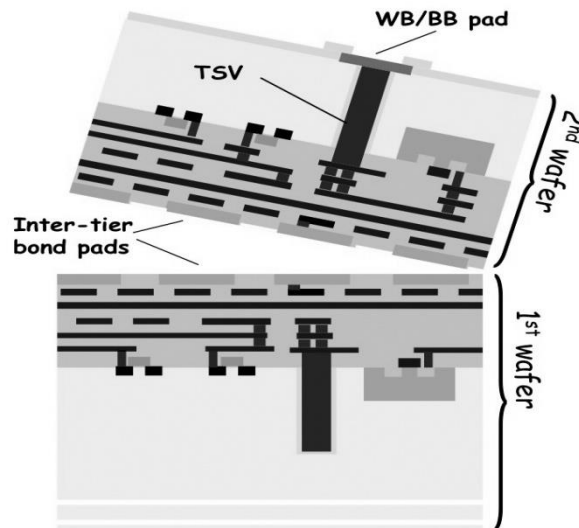


Figure 1.6 Schematic cross-section of the two tiers

A fully processed sensor layer (made with high resistivity silicon for operation in depletion) can be attached to a 3D multi-tier read-out circuit in a separate step. Thus, a side benefit of the 3D-IC development is emergence of die-to-wafer or die-to-die fusion bonding techniques that may be used as a replacement of In or PbSn bump bonding.

Vertical integration technologies have already become quite popular among IC designers, as they can alleviate some important performance limitations correlated with CMOS feature size scaling. They are already widely used in the design of high density storage devices and promise to provide a means to overcome the bandwidth bottleneck in modern microprocessors by vertically integrating processor and memory subsystems in a single chip.

Another possible application of 3D-IC technology, proposed by the INFN Perugia group, is for realizing particle tracking detectors based on CMOS Active Pixel Sensors layers, monolithically integrated in a all-in-one chip, featuring multiple, stacked and fully functional detector layers capable to provide momentum measurement (particle impact point and direction) within a single detector [1.21, 1.22]. In particular, instead of using different tiers of the stacked 3D structure for heterogeneous integration (namely, by devoting different tiers to the sensing layer, and to the analog and digital circuitry), identical fully-functional CMOS APS matrix detectors, including both sensing area and control/signal elaboration circuitry, could be stacked in a monolithic device by means of TSV connections. This will result in a very low material detector, thus dramatically reducing multiple scattering issues. The information coming from thinned multiple stacked layers could be usefully exploited to extend the detection capability of the monolithic sensor. In principle, such a detector would be capable of giving accurate estimation not only of the impact point of a ionizing particle, as well as of its incidence angle. A single detector allowing particle momentum measurement therefore could be built, at the same time being a low material detector multiple scattering effects are expected to be negligible, since incoming particles have to cross only few micrometers of bulk silicon.

References

- 1.1 G. Charpak, *Particle detection by gas discharges*, J. Phys., 30:c2–c86, 1969.
- 1.2 G. Charpak, *Development of multiwire proportional chambers*, CERN Courier, 6:174–176, 1969.
- 1.3 J.B.A. England et al., *A silicon strip detector with 12 μ m resolution*, Nucl. Inst. and Meth., A 196, (1986) 149-151.
- 1.4 L. Rossi, P. Fischer, T. Rohe, and N. Wermes, *Pixel Detectors: From Fundamentals to Applications*, Springer, Berlin, Heidelberg, 2006.
- 1.5 R. Turchetta et al., *A monolithic active pixel sensor for charged particle tracking and imaging using standard VLSI CMOS technology*, Nucl. Instr. and Meth. A 458 (2001) 677-689.
- 1.6 W. Dulinski et al., *CMOS monolithic active pixel sensors for minimum ionizing particle tracking using non-epitaxial silicon substrate*, IEEE Nucl. Sci. Trans. Vol. 51, (2004) 1613-1617, [doi 10.1109/TNS.2004.832947](https://doi.org/10.1109/TNS.2004.832947).
- 1.7 J.L. Blankenship, C.J. Borkowski, *Silicon Surface-Barrier Nuclear Particle Spectrometer*, IRE Trans. Nucl. Sci. 7(3), (1960) 190–195.
- 1.8 L.H.H.Scharfetter, *Active Pixel Detectors for the Large Hadron Collider*, PhD thesis, Leopold Franzens Innsbruck University, Austria, (1996).
- 1.9 E.H.M. Heijne, *Semiconductor micropattern pixel detectors: a review of the beginnings*, Nucl. Instr. and Meth A 465, (2001) 1–26.
- 1.10 M. Moll, *Radiation damage in silicon particle detectors—microscopic defects and macroscopic properties*, PhD Thesis, Universitat Hamburg, Germany (1999). DESY-1999-040.
- 1.11 E.H.M. Heijne et al, *Element Hybrid Silicon Micropattern Pixel Detector Array*, Nucl. Instr. and Meth A 349, (1994) 138–155.
- 1.12 K.H. Becks et al, *First operation of a 72 k element hybrid silicon micropattern pixel detector array*, Nucl. Instr. and Meth A 418, (1998) 15–21.
- 1.13 The ATLAS Collaboration, *Technical design report of the ATLAS pixel detector*, CERN/LHCC/98-13 (1998).
- 1.14 The CMS Collaboration, *CMS tracker technical design report*, CERN/LHCC/98-6 (1998).
- 1.15 The ALICE Collaboration, *ALICE technical design report of the inner tracker system*, CERN/LHCC/99-12 (1999).
- 1.16 G. Dipasquale, et al., *Characterisation of a single photon counting pixel system for imaging of low-contrast objects*, Nucl. Instr. and Meth A 458, (2001) 352–359.

- 1.17 P. Fischer et al., *A counting pixel chip and sensor system for X-ray imaging*, IEEE Trans. Nucl. Sci. 46(4), (1999) 1070–1074.
- 1.18 E.R.Fossum, *CMOS Image Sensors: Electronic Camera-On-A-Chip*, IEEE Trans. on Electron Devices, Vol.44, No.10, (1997), pp.1689-1698.
- 1.19 D. Passeri et al., *Characterization of CMOS Active Pixel Sensors for particle detection: beam test of the four sensors RAPS03 stacked system*, Nucl. Instr. and Meth. A 617 (2010) 573–575.
- 1.20 P. Garrou, C. Bower and P. Ramm, *Handbook of 3D Integration*, Wiley-VCH, (2008)
- 1.21 D. Passeri, L. Servoli, S. Meroli, *Analysis of 3D stacked fully functional CMOS Active Pixel Sensor detectors*, JINST 4 (2009) P04009.
- 1.22 D. Passeri et al., *3D monolithically stacked CMOS active pixel sensor detectors for particle tracking applications*, JINST 7 (2012) C08008 doi:[10.1088/1748-0221/7/08/C08008](https://doi.org/10.1088/1748-0221/7/08/C08008).

Chapter 2.

Interaction of radiation with matter

Radiation is detected by its interaction in matter. Every detection system has the same structure: it starts with the interaction of the radiation with the detection medium; the result of the interaction is transformed into signals, which are read-out and usually recorded. These interaction processes depend on both the type and energy of the incoming particles.

Physical phenomena allowing detection often involve soft electrons or photons, or atomic and molecular excitations. The fundamental mechanism on which radiation detectors are based is the dissipation of a fraction of the incoming radiation energy inside the detecting material. The transferred energy is distributed among excited states, which are capable of generating carriers (for instance electrons-holes in semiconductors, ion pairs in gaseous devices, photons in scintillating media, etc.). These carriers are processed by appropriate read-out elements (for instance front-end electronics for semiconductor detectors and for gaseous devices, or photomultipliers for scintillating materials, etc.). Hence, the required radiation information, such as momentum, energy and velocity, can be obtained. This is the reason why the analysis and the development of silicon detectors needs an extensive knowledge of the physics that describe the radiation interaction with matter. Following will be briefly addressed an overview of basic concepts.

2.1 Passage of charged massive particles through matter

A fast relativistic charged particle traversing matter loses energy in discrete amounts in independent and stochastic single collisions. It interacts with the electrons and nuclei of atoms. The two major effects that characterize the passage of a charged particle through a thickness of material are an energy loss by the particle and a deflection of the same from its incident direction. The interaction mechanism varies with the energy, the mass and the charge of the incoming particle and the characteristics of the target too. In the following we will focus on the particles that have mass. The interaction mechanisms are essentially:

1. Inelastic collisions with the atomic electrons of the material;
2. Elastic scattering from nuclei;
3. Nuclear reactions;
4. Emission of Cherenkov radiation;
5. Bremsstrahlung.

Inelastic collisions with orbital electrons are almost exclusively responsible for the energy loss of heavy particle in matter. In these collisions, energy is transferred from the particle to the atom causing an ionization or an excitation. For light charged particles, e.g. electrons and positrons, there are two main processes contributing to the continuous energy loss: ionization and bremsstrahlung. The bremsstrahlung process is inversely proportional to the squared mass of the incident particle, thus it substantially accounts for radiation losses only for electrons. At electron energies above a few tens of MeV, bremsstrahlung dominates completely other processes [2.1, 2.2].

2.1.1 Cross section

As mentioned above the main interaction mechanism between a charged particle and the crossed material is the collision. Mainly the collisions occur with the atomic electrons of the crossed medium, rarely with the nuclei. In all cases the collisions cause the transfer of an amount of energy from the incident particle to the target and a deflection of the same: the struck atom goes in an excited state and, if the energy is large enough, the hit electron can be detached from its atom creating an ion (primary ionization). If this electron reaches an energy enough large, can be itself a cause for ionization (secondary ionization). In this case the secondary electron is referred as δ -ray. We do not have to think to a collision between two bodies as a contact between their mass, rather as the effect of the electromagnetic interaction between the charged particles. In this scenario is clear that a particle can also interact with electron far from itself (the so called distant collision) and the definition of the collision process is a difficult problem to solve.

The quantity that characterizes the collision process is the *cross section*. Considering a beam of particles with a uniform distribution and F particles per unit of time impinging on a target particle. If we look at the average number of particle N_s scattered into the solid angle $d\Omega$ in the unit of time we can define the differential cross section as:

$$\frac{d\sigma}{d\Omega}(E, \Omega) = \frac{1}{F} \frac{dN_s}{d\Omega} \quad (2.1)$$

The total cross section will be the integral over the entire solid angle:

$$\sigma(E, \Omega) = \int \frac{d\sigma}{d\Omega} d\Omega \quad (2.2)$$

This quantity has the dimension of an area and can be considered as the section normal to the beam direction outside of which the particle is not deflected. However, despite this definition, the cross section is just a measure of the interaction's probability: the larger is this quantity the greater is the probability to have an interaction. According to this last definition the cross section can be defined not only for collisions but also for other kind of interactions.

2.1.2 Mean energy loss for massive particles

The collisions are casual, of course, but their number per macroscopic path length is generally large and this is the reason why average quantities are generally used. One of the most important quantity is the mean energy loss per units length, often called stopping power. Many theories have been developed during the first half of the twentieth century in order to characterize this quantity. The correct quantum-mechanical calculation was first described, around 1932, by Hans Bethe, Bloch and other authors who gave the formula:

$$-\frac{dE}{dx} = 2\pi N_a r_e^2 m_e c^2 \rho \frac{Z}{A} \frac{z^2}{\beta^2} \left[\ln \left(\frac{2m_e \gamma^2 v^2 W_{\max}}{I^2} \right) - 2\beta^2 - \delta - 2\frac{C}{Z} \right] \quad (2.3)$$

with:

$$2\pi N_a r_e^2 m_e c^2 = 0.1535 \text{ MeVcm}^2/\text{g}$$

r_e : electron radius (2.817×10^{-13} cm)

M_e : electron mass

N_a : Avogadro's number

Z : atomic number of absorbing material

A : atomic weight of absorbing material

z : charge of incident particle

β : v/c of incident particle

ρ : density of absorbing material

γ : $1/\sqrt{1-\beta^2}$

δ : density correction

C : shell correction

I : mean excitation potential

W_{\max} : maximum energy transferable in a single collision

W_{\max} can be calculated using the equation:

$$W_{\max} = \frac{2m_e c^2 \eta^2}{1 + 2s\sqrt{1 + \eta^2} + s^2} \quad (2.4)$$

where: $s = m_e/M$ and $\eta = \beta\gamma$.

The mean excitation energy I depends by the orbital frequency of the absorbing material and there is not a precise formula to calculate that value. However values of I for several material have been deduced from measurements [2.3]. The last two terms in the parentheses of Eq. (2.3) are the density and the shell corrections and they have been inserted in the original formulation of Bethe-Bloch in order to enhance the

prediction of the formula at certain range compared to the experimental results. The density correction takes into account the effect of the electric field produced by incoming particles and is more evident at high velocity. Instead, the shell correction is noticeable when the velocity of incident particle is comparable to the orbital velocity of the bound electrons of the target material. At this low energy some other complicated effects come into play and the Bethe-Bloch formula breaks down. When the velocity is comparable with the speed of orbital electrons of the target material the energy loss reach a maximum depending on the sign of the charge (Barkas effect) and for lower energy drops sharply. At higher energy (that means higher velocity) dE/dx is dominated by the $1/\beta^2$ factor and decreases until $\beta \cong 0.96c$ where a minimum is reached. Particles with this energy are usually indicated with the name of minimum ionizing particle (MIP).

Increasing the energy the losses do not increase so much due to the density effect (Fermi plateau) until the radiative components, such as the Cherenkov radiation and Bremsstrahlung, start to be relevant. The Cherenkov radiation arises when a charged particle in a medium moves faster than the speed of light in that same medium ($\beta c > c/n$, with n : index of refraction): in such case an electromagnetic shock wave is created, just as an aircraft that moves faster than sound.

Especially for light particles, such as electrons or positrons at very high energy, the Bremsstrahlung emission represents the main energy loss mechanism. The deflection and the deceleration of the particle due to the interaction with the nuclei of the target cause the emission of photons; this effect is much greater as lighter is the particle and higher is the atomic number of target material. While ionization loss rates rise logarithmically with energy, Bremsstrahlung losses rise linearly and dominate at high energy (just only above few tens of MeV in most material for electrons). In Figure 2.1 it is shown the mean energy loss (also known as stopping power) for muons that traverse a copper target in the range of few hundreds of keV to tens of TeV.

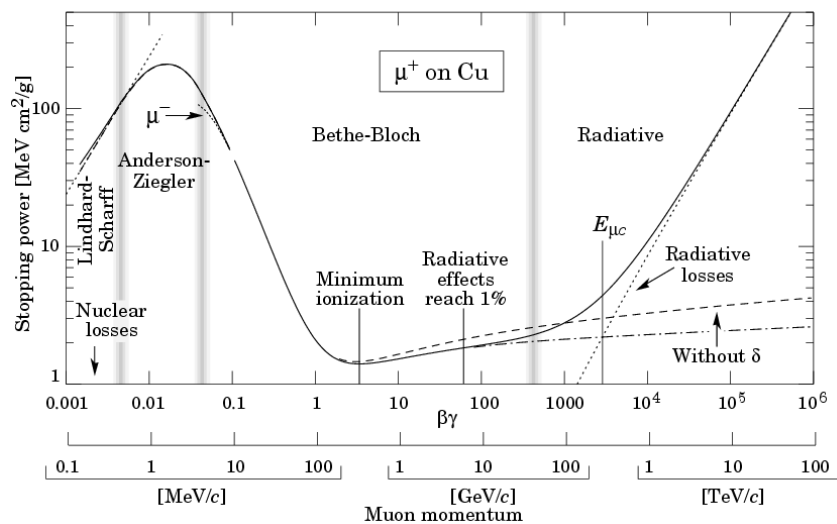


Figure 2.1 Stopping power for positive muons in Copper [2.4]

2.1.3 Correction to Bethe-Bloch for electrons and positrons

Electrons or positrons needs particular consideration. First, their small mass implies the possibility of a large deflection due to a single collision too; moreover the collisions are between identical particles, so that the calculation must take into account their indistinguishability. As result the maximum transferable energy in a single collision becomes:

$$W_{\max} = T_e / 2 \quad (2.5)$$

with T_e : kinetic energy of the incident particle, and the Bethe-Bloch formula can be rearranged as:

$$-\frac{dE}{dx} = \frac{2\pi N_a r_e^2 m_e c^2 \rho Z}{A\beta^2} \left[\ln \frac{\tau^2(\tau+2)}{2\left(\frac{I}{m_e c^2}\right)^2} + F^\pm(\tau) - \delta - 2\frac{C}{Z} \right] \quad (2.6)$$

with:

$$\tau = \frac{T_e}{m_e c^2} \quad (2.7)$$

$$F^-(\tau) = 1 - \beta^2 + \frac{\tau^2 - (2r_e + 1) \ln 2}{8(\tau + 1)^2} \quad (2.8)$$

$$F^+(\tau) = 2 \ln 2 - \frac{\beta^2}{12} \left(23 + \frac{14}{\tau + 2} + \frac{10}{(\tau + 2)_2} + \frac{4}{(\tau + 2)^3} \right) \quad (2.9)$$

where suffix “+” means positrons and “-” means electrons.

2.2 Energy straggling

Up to now, in this chapter, the discussion of energy loss has been concerned mainly with the mean energy loss suffered by charged particles when passing through a thickness of matter.

The amount of energy loss is a stochastic quantity with two sources of variations i.e. the amount of energy transferred in a single collision and the actual number of collisions. The number of collisions fluctuates according to the Poisson law i.e. for N collisions the number of collisions varies as \sqrt{N} . The relative variation of the collision number is inversely proportional to \sqrt{N} , so in the limit of very thick absorbers, the fluctuations in the energy loss due to the number of collisions vanish. However, for a finite thickness medium, the actual value of the collision number fluctuates. The distribution of the energy loss is called the

straggling function, and only for a thick layer it has a nearly Gaussian form. In general, the distribution is non-symmetric, skewed towards high values, with a long tail in the direction of high values of energy depositions. The probability of individual interactions with large amounts of energy transferred is strongly reduced, which implies the mean value of the distribution higher than the most probable one. Theoretically, the calculation of the energy loss distribution for a given thickness is a difficult mathematical problem and is generally divided into two cases: thick absorbers and thin absorbers.

2.2.1 Thick absorber

For thick absorber the number of collisions along the path of incoming particles is large. If we assume that the energy lost in each collision is not so large to alter the velocity of incident particle, the overall sum of all losses will be the sum of a large number of random variable with the same probability distribution. For the central limit theorem a sum like that approaches to the Gaussian distribution [2.5]:

$$f(x, \Delta) \propto \exp\left(\frac{-(\Delta - \langle \Delta \rangle)}{2W_m \xi (1 - \beta^2 / 2)}\right) \quad (2.10)$$

with x : thickness of absorber, Δ : energy loss, $\langle \Delta \rangle$: mean energy loss and

$$\xi = 0.1535 \cdot \frac{\rho z^2 Z}{A \beta^2} x \quad [\text{MeV}] \quad (2.11)$$

When the thickness of the absorber is very large, the assumption that the velocity does not change along the path becomes invalid.

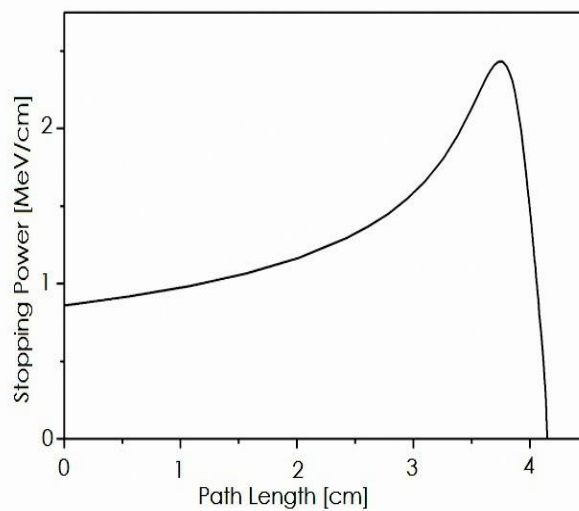


Figure 2.2 Typical Bragg curve showing the variation of stopping power as a function of the penetration depth [2.1].

From the Figure 2.1 it is clear that when a particle slows down in matter, its rate of energy loss change as its kinetic energy changes: in particular, below the MIP condition, the more the particle slow down, the more it releases energy and the more it will be slowed; at the end, if the target is large enough, the particle will be completely stopped. Figure 2.2 shows an example of how the stopping power varies along the path of a particle beam until it is completely stopped; this kind of curves are known with the name of *Bragg curves*.

2.2.2 Thin absorber

In contrast to the thick absorber case, the distribution for thin absorbers, where the number of collisions N is too small for the Central Limit Theorem to hold, is extremely complicated to calculate.

This is because of the possibility of large energy transfers in a single collision which adds a long tail to the high energy side of the energy loss probability distribution thus giving it a skewed and asymmetric form. Figure 2.3 illustrates this general shape. It may be characterized schematically by the position of the maximum of the distribution function (Δ_p) and by the full width at half maximum (w). Note that the mean energy loss no longer corresponds to the peak but is displaced because of the high energy tail.

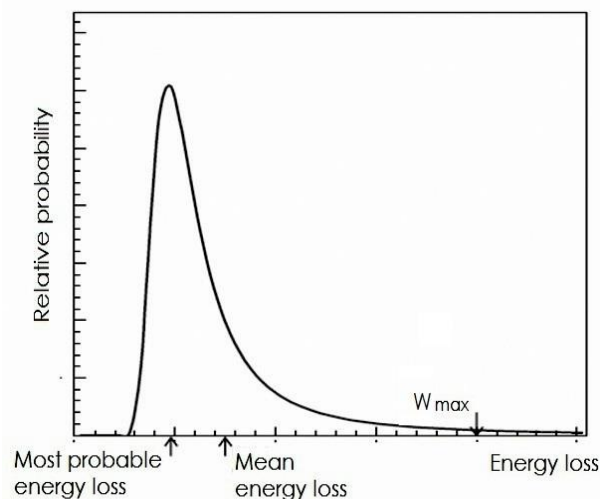


Figure 2.3 Straggling functions in silicon for 500 MeV pions, normalized to unity at the most probable value.

Theoretical calculations of this distribution have been carried out by Landau and Vavilov [2.6, 2.7]; these solutions have a different region of applicability and the discriminating parameter is the ratio $k = \langle \Delta \rangle / W_m$.

Landau solved this problem for $k \leq 0.01$ making the assumptions that:

1. The maximum energy transfer is infinite $W_m = \infty$;
2. The electron binding energy in a collision is negligible, in other words the electrons involved in collisions are treated as free and the distant collision is ignored;
3. The particle velocity remains approximately the same;
4. Taking only the first term of Eq. (2.3), the mean energy loss $\langle \Delta \rangle$ is approximated to the ξ parameter.

He derived the expected energy loss distribution by solving an integral transport equation:

$$\frac{df}{dx}(x, \Delta) = \int_0^{\infty} W(E)[f(x, \Delta - E) - f(x, \Delta)] dE. \quad (2.12)$$

Here $f(x, \Delta)$ represents the distribution probability that the incident particle will lose an amount Δ of energy when crossing a layer of thickness x . This function is usually called *straggling function*. $W(E)dE$ represents the probability per unit path length of a collision transferring energy E to an electron in the material.

The function $W(E)dE$ is not generally known but Landau was able to derive an approximate solution by using the free electron (Rutherford) cross section:

$$W(E) = \frac{\xi}{x} \cdot \frac{1}{E^2} \quad (2.13)$$

The Landau distribution is therefore given by

$$f_L(x, \Delta) = \frac{\varphi(\lambda)}{\xi} \quad (2.14)$$

with $\varphi(\lambda)$ a universal function of the variable λ only

$$\varphi(\lambda) = \frac{1}{\pi} \int_0^{\infty} e^{(-\pi y/2)} \cos(y \ln y + \lambda y) dy \quad (2.15)$$

and

$$\lambda = \frac{\Delta - \langle \Delta \rangle}{\xi} - \beta^2 - \ln(k) - 1 + C_E \quad (2.16)$$

where C_E : Euler constant equal to 0.5772.

The Landau distribution, $f_L(\Delta)$, is asymmetric with a tail extending to W_m with a maximum for $\lambda=0.229$ and $w_L=4.018\xi$.

The energy loss corresponding to the maximum of the function $f_L(\Delta)$ is the most probable energy loss [2.4]

$${}_L A_p = \xi \left[\ln \frac{2m_e c^2 \beta^2 \gamma^2}{I^2} + \ln \frac{\xi}{I} + 0.2 - \beta^2 - \delta \right] \quad (2.17)$$

Subsequently Vavilov derived an improved solution which takes in account the spin of the incident particle.

For the collision cross section Vavilov used the form

$$W(E) = \frac{\xi}{x} \cdot \frac{1}{E^2} \left(1 - \frac{\beta^2 E}{E_{MAX}} \right) \quad (2.18)$$

Vavilov also demonstrated that his solution tends to the Landau function for $k \leq 0.01$, region where $\langle \Delta \rangle$ is approximated by ξ . For $k > 10$ the number of collisions is very large and, for the Central Limit Theorem, the Vavilov function coincides with a Gaussian distribution.

Further corrections to the theory taking into account the fact that the electrons in the material are not free have been proposed by Blunck and Leisegang [2.8], Shulek [2.9] and Bichsel [2.10]. For solid state materials, comparisons with experimental observations have been made: while the most probable energy loss agrees rather well with the prediction of the theory, the width of the distribution is broader than expected and cannot be accounted for by electronic noise or imperfect resolution. The effect is particularly noticeable for very thin absorbers [2.11], of the order of a few hundred micrometers or less of thickness. The modified energy loss distribution can be improved by using a modified cross section to take into account the electron binding energy.

The modified energy straggling function can be therefore expressed as [2.12]:

$$f(x, \Delta) = \frac{1}{\sigma \sqrt{2\pi}} \int_{-\infty}^{+\infty} f_L(x, \Delta - \tau) \exp\left(-\frac{\tau^2}{2\delta_2}\right) d\tau \quad (2.19)$$

In other words the experimentally observed energy spectrum can be calculated by convolving the Landau distribution with a normal distribution of variance δ_2 . The results of the convolution is a broader distribution with a peak value usually increased by a small amount compared to the Landau theory. Shulek et al. [2.9] propose the form

$$\delta_2 = \frac{8}{3} \cdot \frac{\xi}{x} \sum_i I \cdot f_i \ln \frac{2m_e c^2 \beta^2}{I_i} \quad (2.20)$$

as an estimate of the effect, where I_i is the effective ionization potential of the i -th shell and where f_i is the fraction of electrons in that shell. The resulting improved energy loss distribution has an overall value of w , which is roughly given by: $\sqrt{w_L^2 + 5.56 \cdot \delta_2}$

As the material thickness decreases, δ_2 becomes more and more the dominant term, which determines the overall w of the straggling function. Conversely, it is not expected to provide an additional broadening of the distribution at large thicknesses.

2.2.3 Energy straggling for electrons and positrons

As for the stopping power, a correction should be considered in the case of electrons or positrons. Mainly due to the fact that after collision is impossible to distinguish between the incoming electron and the electron of the struck atom, and the fact that the mass of the particles into play is the same, the cross section and the other quantity from which the Landau-Vavilov solution comes out must be modified. By the same procedure used by Landau but starting from the correct cross section, the energy straggling function becomes:

$$f^{\pm} = f_L(\Delta, x) \exp[\alpha^{\pm}(\lambda + \ln \alpha^{\pm})] \quad (2.21)$$

where:

$$\begin{aligned} \alpha^+ &= \left(\frac{\xi}{E_K} \right) \beta^2 \left[2 - \frac{1}{(\gamma + 1)^2} \right] \\ \alpha^- &= \left(\frac{\xi}{E_K} \right) \cdot \left[\frac{2\gamma - 1}{\gamma^2} \right] \end{aligned} \quad (2.22)$$

The suffix “+” or “-“ means respectively the case of positrons or electrons, and E_K is the kinetic energy of beam.

2.2.4 Energy for charge carrier generation in semiconductor material

The energy W required to create an e-h pair in a semiconductor by a charged mass particle traversing the medium depends on the band gap energy E_g of the material and hence, although only slightly, on the temperature. The measurements of this quantity show a nearly linear dependence on the band gap energy, and the linear fit to the data obtained for different materials gives [2.13]

$$W(E_g) = [1.76 + 1.84 \cdot E_g] eV \quad (2.23)$$

The energy for charge carrier generation is always higher than the band gap energy due to the possible additional excitation of phonon and plasmon states. Phonon excitation transfers energy to the lattice, and the energy transferred appears finally as heat in the detector. The plasmon is the quantum of the valence electron density oscillations with a mean energy of 17eV for silicon. The valence electrons are those of the M-shell and they are only weakly bound to the atoms. Thus, they may be considered as a dense and nearly homogeneous density gas, i.e. plasma of negative charge carriers in the semiconductor material volume. The mean energy W to create an e-h pair has been calculated and measured in experiments including high energy charged particles and x-ray photons [2.13, 2.14]. The mean energy W required to create an e-h pair in silicon is $W \approx 3.68eV$.

2.2.5 Radiation length

Energy loss due to radiation emission is negligible for heavy particles with masses significantly higher than the mass of the electron. However, a high energy electron or a high energy photon incident on matter initiates electromagnetic cascades by bremsstrahlung and e^+e^- pair production processes, respectively. The characteristic amount of matter traversed for these related interactions is called the radiation length X_0 , which is usually measured in g/cm^{-2} . This is a scaling variable used for the probability of occurrence of bremsstrahlung or pair production, and for the variance of the angle of multiple Coulomb scattering. The average energy loss due to bremsstrahlung for an electron of energy E is related to the radiation length by

$$\frac{dE}{dx} = \frac{1}{X_0} E \quad \rightarrow \quad E(t) = E_0 \exp\left(-\frac{t}{X_0}\right) \quad (2.24)$$

where E_0 : initial energy of the incident particle. Thus, the radiation length is a mean distance over which a high energy electron loses all but $1/e$ of its energy by bremsstrahlung. The probability for a e^+e^- pair to be created by a high energy photon equals to $7/9 X_0$. The value of radiation length depends on the atomic number Z of the material. A useful approximation convenient for quick calculations of the radiation length is given by

$$X_0 = 716.4 \frac{A}{Z(Z+1)\ln(287/\sqrt{Z})} \quad (2.25)$$

and can be found tabulated by Y.S. Tsai [2.15]

Eq. (2.25) is a heuristic expression providing 2.5% agreement with more accurate and advanced estimations. The radiation length for silicon is $X_0 \approx 9.36 \text{ } \mu\text{g}/\text{cm}^{-2}$. The radiation length in mixtures or compounds of materials having different properties is calculated as a weighted mean of contributions from each constituent.

2.3 Multiple Coulomb scattering

In addition to inelastic collisions with the atomic electrons, particles passing through matter suffer repeated elastic Coulomb scattering from nuclei although with a smaller probability. Considering that usually nuclei have mass greater than the incoming particle, the energy transfer is negligible but each scattering centre adds a small deviation to the incoming particle trajectory. Even if this deflection is small the sum of all the contribution adds a random component to the particle path which proceeds with a zig-zag path (see Figure 2.4). As result, a beam after a thickness of material shown a divergence greater than the incoming one.

Three situations can be considered:

1. *Single scattering*. When the thickness is extremely small and the probability to have more than one interaction is negligible. This situation is well described by the Rutherford formula:

$$\frac{d\sigma}{d\Omega} = \left(\frac{1}{4\pi\epsilon_0} \right)^2 \frac{z^2 e^4}{M^2 c^4 \beta^4} \frac{1}{\sin^4(\theta/2)} \quad (2.26)$$

2. *Plural scattering*. When the number of Coulomb scattering increases but remains under few tens of interactions. This is the most difficult case to deal with, several works have been done by different authors (see [2.16] for further information).
3. *Multiple scattering*. When the thickness increases and the number of interactions become high the angular dispersion can be modeled as Gaussian.

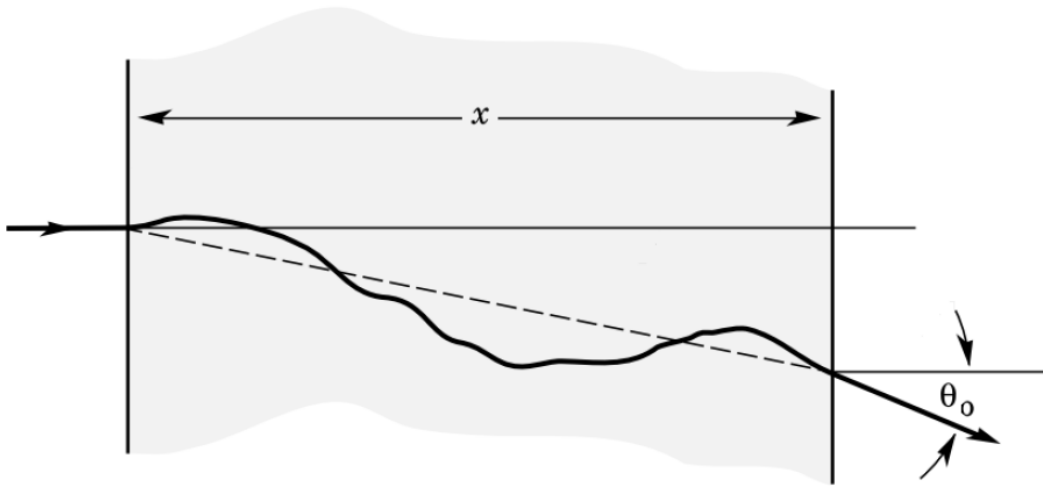


Figure 2.4 Effect of multiple Coulomb scattering.

Referring to multiple scattering, that is the most common situation for silicon detectors, naming Θ the solid angle into which is concentrated the 98% of the beam after a thickness x of material, if we define $\theta_0 = \Theta/\sqrt{2}$ as the projection of Θ on a plane, the angular dispersion can be calculated by the relation:

$$\theta_0 = \frac{13.6}{\beta c p} z \sqrt{x/X_0} [1 + 0.038 \ln(x/X_0)] \quad (2.27)$$

where p : momentum and X_0 : radiation length.

2.4 The interaction of photons

The behavior of photons in matter is completely different from that of charged particles. In particular, the photon's lack of an electric charge makes impossible the many inelastic collision with atomic electrons so

characteristic of charged particles. For this kind of radiation the most important mechanism of interaction are:

1. Photoelectric effect;
2. Compton and Rayleigh scattering;
3. Pair production.

As consequence of such kind of interactions a photon that interacts with the target is completely removed from the incident beam. Moreover, due to the smallest cross section of all this kind of reactions, *x-ray* or *γ-ray* are many times more penetrating than charged particles. The attenuation of the incident beam is exponential with the thickness of the absorbing medium and can be expressed by the following relation:

$$I(x) = I_0 \exp(-x\mu_l) \quad (2.28)$$

where μ_l : linear attenuation coefficient, I_0 : incident beam intensity and x : thickness. The linear attenuation coefficient is related to the cumulative cross section by the relation:

$$\mu_l = \eta_A \sigma_{tot} \quad (2.29)$$

where η_A : number of atoms per unit of mass and σ_{tot} : total cross section. The total or cumulative cross section σ_{tot} is the sum of all the cross sections of the interactions mentioned above. A plot of this quantity is shown in Figure 2.5 where the different components have been highlighted.

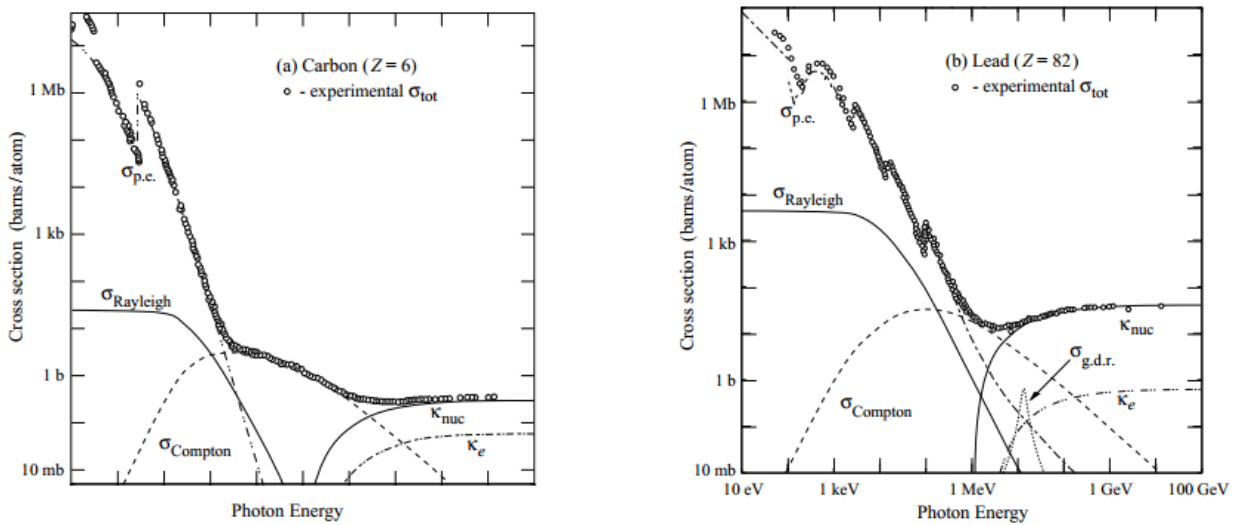


Figure 2.5 Cross sections of photons in Carbon (a) and Lead (b) in barns/atom.

In photoelectric absorption, a photon disappears being absorbed by an atomic electron. The process results in ionization by subsequent ejection of the electron from the atom. The energy of the liberated electron is the difference between the photon energy and the energy needed to extract the electron from the atom i.e. the binding energy of the electron. The recoil momentum is absorbed by the nucleus to which the ejected electron was bound. If the resulting photoelectron has sufficiently enough kinetic energy, it may be a source

of a secondary ionization occurring along its trajectory, and in the case of the semiconductor material, it may create further e-h pairs. If the electron does not leave the detector the deposited energy corresponds to the energy possessed by the incident photon. This feature of the photoelectric effect allows to calibrate the gain of the detector chained with its read-out system if the energy required to create a single e-h pair is known. The range R of the electron having the kinetic energy E is of the order of some micrometers, as given by the follow equation [2.17]:

$$R[\mu m] = 40.8 \cdot 10^{-3} (E[keV])^{1.5} \quad (2.30)$$

Thus the cloud of generated charge is confined close to the photon absorption point. Normally there may be escaping photons, which can leave the detector volume, leading to a lesser amount of energy deposited. These photons are actually the fluorescence photons emitted by de-exciting atoms. Photons of fluorescence radiation are emitted by atoms after the ejection of a deep shell (K, L) electron. The incident photon creates a vacancy in the shell that can be filled by an outer orbital electron, giving rise to the emission of the characteristic x-rays photons of the fluorescence radiation. The missing energy, which is conveyed by the escape photons leads to, so called escape peaks in the measured energy spectrum. Photon interaction coefficient for photoelectric absorption depends strongly on the atomic number of the absorbing material. The relevant cross section increases roughly as Z^3 . For silicon, the photoelectric effect is the dominant process for photon energies below 100keV.

The Compton scattering instead involves the free electrons. Inside matter the electrons are bound to an atom; however, if the photon energy is high with respect to the binding energy, this latter energy can be ignored and the electrons can be treated as essentially free. When Compton scattering occurs, the electron is scattered away in conjunction with a new photon with lower energy than the incoming one. In Rayleigh scattering the photon interact with the whole atom and the only effect of this interaction is a deflection of the incoming photon; it does not participate to the absorption and for most purposes can be neglected.

At very high energy another effect starts to be relevant: the pair production. In this process the photon interacts with an electron or a nucleus producing a positron-electron pair. In order to produce the pair the photon must have at least an energy of 1.022MeV. In Figure 2.5, with k_{nuc} and k_e , are shown the two components of the pair production cross section, respectively for the interaction with nuclei or electrons. Another possible interaction, but usually negligible compared to the previous ones is the Photonuclear reaction; in this case the photon interact directly with the nucleus. The related cross section is shown in Figure 2.5 in dotted line ($\sigma_{g.d.r.}$). The above cross section in barns/atom (1barn = 10^{-24} cm², approximately the section of an uranium nucleus) expresses the probability of an interaction. A more suitable quantity, often used to characterize the absorption of a photon shower, is the mass attenuation coefficient. The mass attenuation coefficient is defined as:

$$\mu_m = \frac{\mu_l}{\rho} = \frac{\eta_A}{\rho} \sigma_{a,tot} \left[\frac{g}{cm^2} \right] \quad (2.31)$$

with ρ : density of the material.

References

- 2.1 William R. Leo, *Techniques for Nuclear and Particle Physics Experiments*. Berlin and Heidelberg: Springer, 1987.
- 2.2 Claude Leroy, Pier Giorgio Rancoita, *Principles of radiation interaction in matter and detection*. Singapore: World Scientific Publishing, 2004.
- 2.3 International Commission on Radiation Units and Measurements. [Online]. <http://www.icru.org/NK>
"http://www.icru.org/" <http://www.icru.org/>
- 2.4 Particle Data Group PDG, *Passage of particle through matter*, Nuclear and Particle Physics, vol. 33, no. 27, pp. 258-270, July 2006.
- 2.5 S. M. Sze, Kwok Kwok Ng, *Physics of Semiconductor Devices*. John Wiley & Sons, 2007.
- 2.6 L. Landau, *On the Energy Loss of Fast Particles by Ionization*, J. Phys. USSR **8** (1944) 201.
- 2.7 P.Vavilov, *Ionization losses of high energy heavy particles*, Soviet Physics JETP **5** (1957) 749.
- 2.8 Blunck and S. Leisegang, *Zum Energieverlust schneller Elektronen in dünnen Schichten*, Z. Physik **128** (1950) 500.
- 2.9 P. Shulek et al., *Fluctuations of Ionization Loss*, Sov. J. Nucl. Phys **4** (1967) 400.
- 2.10 H. Bichsel, *Straggling of Heavy Charged Particles: Comparison of Born Hydrogenic Wave Function Approximation with Free-Electron Approximation*, Phys. Rev. B **1** (1970) 2854
- 2.11 H. Esbensen et al., *Random and channeled energy loss in thin germanium and silicon crystals for positive and negative 2-15-GeV/c pions, kaons, and protons*, Phys. Rev. B **18** (1978) 1039.
- 2.12 Hancock et al., *Energy loss and energy straggling of protons and pions in the momentum range 0.7 to 115 GeV/c*, Phys. Rev. A **28**, (1983) 615–620.
- 2.13 R.C.Alig, S.Bloom, C.W.Struck, *Scattering by Ionization and Phonon Emission in Semiconductors*, Phys. Rev. B, Vol.22, No.12, (1980), pp.5565-5582.
- 2.14 G.W.Fraser et al., *The X-ray Energy Response of Silicon*, Nucl. Instr. and Meth., A **350**, (1994), pp.368-378.
- 2.15 Yung-Su Tsai, *Pair production and bremsstrahlung of charged leptons*, Reviews of Modern Physics, vol. 46, no. 815, 1974.
- 2.16 E. Keil, E.Zeitler, and W. Zinn, *Zeitschrift für Naturforschung A*, vol. 15A, no. 1031, 1960.
- 2.17 I.M.Bronstein, B.S. Fraiman, "Determination of the Path Lengths of Slow Secondary Electrons", Sov. Phys. Solid State, Vol.3, (1961), pp.1188-1197.

Chapter 3.

CMS Hybrid Pixel Detectors

The CMS tracking system consists of two sub-detectors [3.1]: the silicon strip and the silicon pixel detector, the latter being the innermost subsystem of the CMS detector. Its purpose is to provide high resolution track hits as close as possible to the interaction point. The large charged track density close to the beam requires the usage of a pixel system, which can provide three dimensional hit information while keeping the pixel occupancy low. The CMS pixel detector design is based on the following general principles: precise hit reconstruction to allow for a precise vertexing, radiation hardness of all components to overcome the radiation damage during several years of operation, minimal material budget to minimize multiple scattering of the particles, low noise electronics to reduce the number of fake hits, minimal hit losses, and affordable costs. The overall detector layout is shown in Figure 3.1.

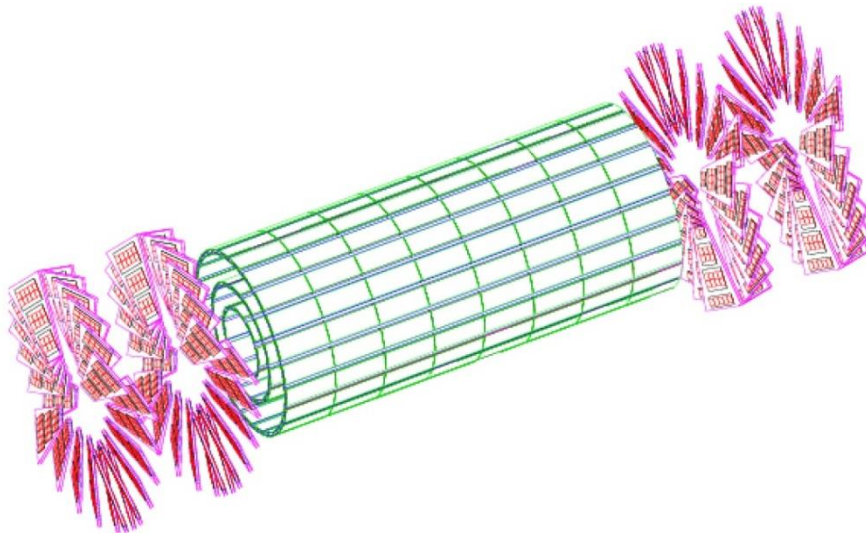


Figure 3.1 Layout of the CMS pixel detector with three barrel layers (drawn in green) and four forward disks (drawn in red).

3.1 Pixel Barrel Modules

All barrel modules are built out of the following components. The silicon sensor is electrically connected to 16 read-out chips (ROCs) [3.2]. The connection between sensor and ROCs is made of indium bumps [3.3], which connect each sensor pixel with a pixel unit cell (PUC) on the ROC. On top of the sensor a High Density Interconnect (HDI) serves as an interface to the front end electronics. The connection is established over two cables: the power cable for the necessary supply voltages and the signal cable for the control signals and the analogue read-out. The chip on the HDI, which organizes the read-out of all the ROCs, is called Token Bit Manager (TBM) [3.4].

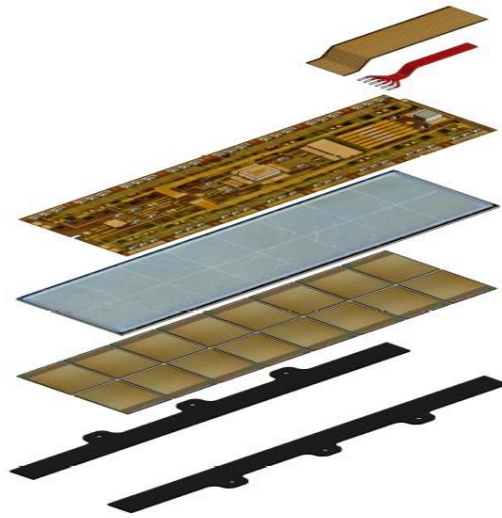


Figure 3.2 Exploded view of a pixel barrel module.

The connection of the HDI to the ROCs is done with the help of wire bonds. At the very bottom, the base stripes provide the necessary mechanical rigidity and are used to mount the module onto the support and cooling structure. In Figure 3.2 the components, from top to bottom, are: the signal cable, the power cable, the HDI, the silicon sensor, the 16 ROCs and the base stripes. The main properties of a full barrel module are summarized in Table 3.1.

Table 3.1 Properties of the full CMS Pixel Barrel Modules

Size	66.6 mm × 26 mm
Weight	3.5 g
# Pixels	66560
# ROCs	16
# Pixels per ROC	52 · 80 = 4160
Pixel size	100 μm × 150 μm
Sensor thickness	285 μm

3.1.1 The sensor

Due to elastic scattering with electrons, charged particles lose part of their energy when traversing some material. By applying an electrical field to the semiconductor, the generated charge carriers start to move along the electrical field-lines. This current itself induces a signal in the collecting electrode, which is detectable by the read-out electronics. For the CMS pixel detector, silicon was chosen as the sensor material with n+ implantation on a n-type substrate [3.5]. To achieve a good spatial resolution, an almost squared pixel size of $100\mu\text{m} \times 150\mu\text{m}$ was implemented. The sensor thickness is $285\mu\text{m}$, which results in an ionization charge of roughly 23000 electron for a minimum ionizing particle traversing the sensor at a right angle. To fully deplete the unirradiated sensor, a bias voltage of roughly 150V has to be applied, whereas for the irradiated sensor up to 600V will be necessary.

3.1.2 The High Density Interconnect

The HDI distributes the different signals (like clock or trigger) and voltages to all ROCs. Since the module includes analogue as well as digital parts, three voltages are required: analogue and digital voltage plus the high voltage for the sensor. These voltages are supplied via the power cable (the lower cable in Figure 3.2). The communication of the HDI with the front end electronics is handled over a multi-channel Kapton cable. A chip placed on the HDI, called TBM, has to organize the read-out of all ROCs. After having received a trigger, it sends a token to all ROCs, which tells them to send their hits to the TBM. The TBM itself adds a hit counter and some status bits to the data stream. The whole information of a read-out is sent as analogue signal to the optical links. The modules are read out in a zero suppression mode, i.e. for each hit its position and pulse heights are sent to the front end electronics.

3.1.3 The read-out chip

The purpose of the *PSI46* ROC is to read out the ionization charge of the sensor pixels at the bunch crossing frequency of 40MHz and to store the information during the CMS detector latency [3.2]. The ROC is divided into two parts: the active area with one PUC per sensor pixel to read out the collected charge, and the periphery with the control interfaces and data buffers to store the hit information. The active area is organized in 26 double-columns and 80 rows and is therefore able to read out 4160 pixels. Each sensor pixel is connected to the corresponding PUC through an indium bump bond. If a sensor pixel is traversed by a charged particle, the collected ionization charge induces a voltage signal in the PUC. If the amplified signal exceeds a tunable threshold, the periphery of the corresponding double-column periphery is notified. The double-column periphery itself starts the read-out mechanism, which stores the position of the hit pixel as well as the pulse height and the bunch crossing in buffers. If the module receives a trigger signal for the corresponding bunch crossing, this hit information is added to the analogue signal.

The testing of the read-out mechanism is much simplified by the possibility to directly inject a calibration voltage to the preamplifiers, which allows to qualify a module without an external source. The amplitude of the injected signal is controlled by the *Vcal* DAC, its timing by the *CalDel* DAC. The signal from the sensor or the internal calibration mechanism first passes the preamplifier and the shaper. If the comparator finds that the amplitude exceeds some reference voltage, a hit is generated. The reference voltage can be adjusted for each ROC by the *VthrComp* DAC. An individual pixel correction to this global threshold can be applied by setting the four trim bits, which will lower the threshold depending on the value of the *Vtrim* DAC. The comparator of a pixel can be disabled by setting a mask bit.

3.2 Test setup

To reliably test several hundreds of modules, it was necessary to develop a stable test suite covering all kinds of module operation aspects. The sensor under test, used in this work to check the functionality of the implemented algorithms, is a reduced version of the pixel module, featuring only one ROC connected to 80 x 52 pixel (1/16 of the standard module dimension).

The test setup consists of the following pieces (see Figure 3.3)

- A desktop PC with a Ubuntu 10.10 operating system;
- A reduced pixel module;
- One electronics testboard, especially designed to test the pixel sensor;
- A Keithley high-voltage supply;
- A cooling box to regulate the ambient temperature and humidity during module testing.

The testboard provides the sensor with the necessary supply voltages and electrical signals (like clock, trigger, etc..). To analyze the read-out of the module, it includes two 12-bit Analogue to Digital Converters, which sample the analogue signal in the interval $[-2048, +2047]$, with 1 ADC unit corresponding to 0.128mV. The central control unit of the testboard is formed by a Field Programmable Gate Array (FPGA) with an implemented processor.

The cooling box offers space for four modules. The temperature within the volume that contains the modules is adjusted by use of four water cooled, high-performance Peltier elements. To lower the humidity, Nitrogen is provided to the cooling box through two flow regulators. The Peltier elements and the N₂ flow regulators are connected to controller channels of a *JUMO Imago 500* process and program controller. The temperature is measured with a Platinum resistance thermometer (Pt-100) connected to the controller. Two program channels are allocated to regulate either heating or cooling. The communication between the controller and the PC is established with an RS422/485 serial interface.

The algorithms have been implemented in a C++ software package called *psi46expert* which runs on a standard PC. For data storage and analysis the ROOT framework [3.6] was used. The presence of a processor inside the FPGA on the testboard allows to run parts of the test algorithms directly on the

testboard. This speeds up the tests by reducing the data transfer between PC and testboard, which is carried out over an USB connection. Especially interactive algorithms, where the test flow depends on the results of previous measurements profit a lot.

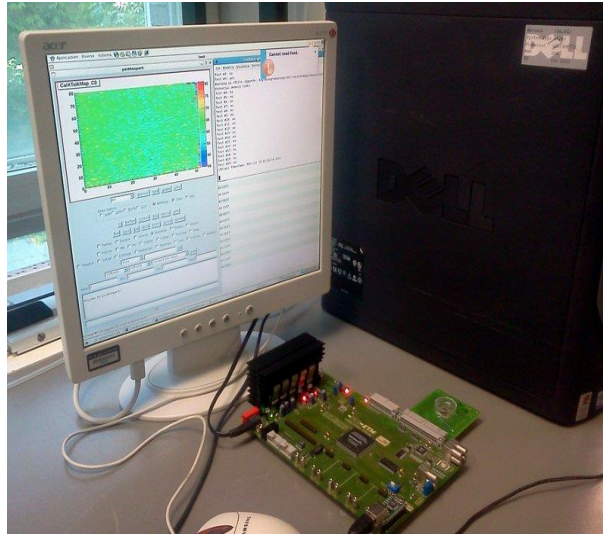


Figure 3.3 Picture of the test setup

3.3 Functionality analysis of CMS pixel sensor

To check the correct hardware functionality of the sensor, functionality tests have been carried out. In particular, the pixel read-out and the address decoding of the 4160 pixels on the sensor have been extensively tested. For the pixel read-out test it is verified that sending a calibration pulse to the enabled pixel, results in the corresponding hit information in the analogue signal. For this, the pixel is read out 10 times with V_{cal} set to a value of 200 in the low range. If the hit does not show up in the analogue signal all ten times, the pixel is called *dead*.

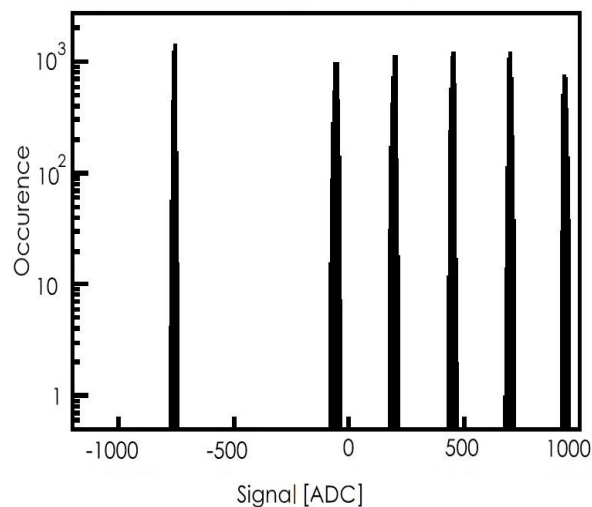


Figure 3.4 Address levels of all pixels in the ROC under test.

For the analog decoding test the pixel address levels have been checked. An individual pixel address consists of five clock cycles in the analogue signal: two cycles encode the double-column index and three the index within a double-column [3.7]. Each clock cycle can take six different levels. To decode correctly the pixel address, these levels have to be well separated. To check this, the levels of all pixels in a ROC are measured and overlaid in a histogram as shown in Figure 3.4. In this histogram, a simple algorithm searches for separated peaks. If exactly six of them have been found, the decoding limits are placed in the centers between two neighboring peaks. These limits are used in the second part of the test, which records the analogue read-out of each pixel and checks whether the pixel generates the address which corresponds to its physical position on the ROC.

To identify noisy pixels, which potentially have to be masked, the noise of each single pixel is measured. The noise is determined by measuring the so called *S-curve*, which is the response efficiency of the pixel as a function of the amplitude of the calibration signal. For an ideal pixel without any noise, this would be a simple step-function: zero efficiency below the signal threshold and full efficiency above. The effect of the noise is to smear out this step function. If the noise is assumed to be Gaussian, the S-curve has the shape of an *error function*, with a width proportional to the noise. These data points are then fit with an error function and the width and the position of the 50% point are extracted, see Figure 3.5(a). The width is first converted to Vcal DAC units (1 Vcal DAC = 1.20mV) and afterwards to electrons (1 Vcal DAC \approx 65e). The noise level of the default size pixels turns out to be 158e (Figure 3.5(b)).

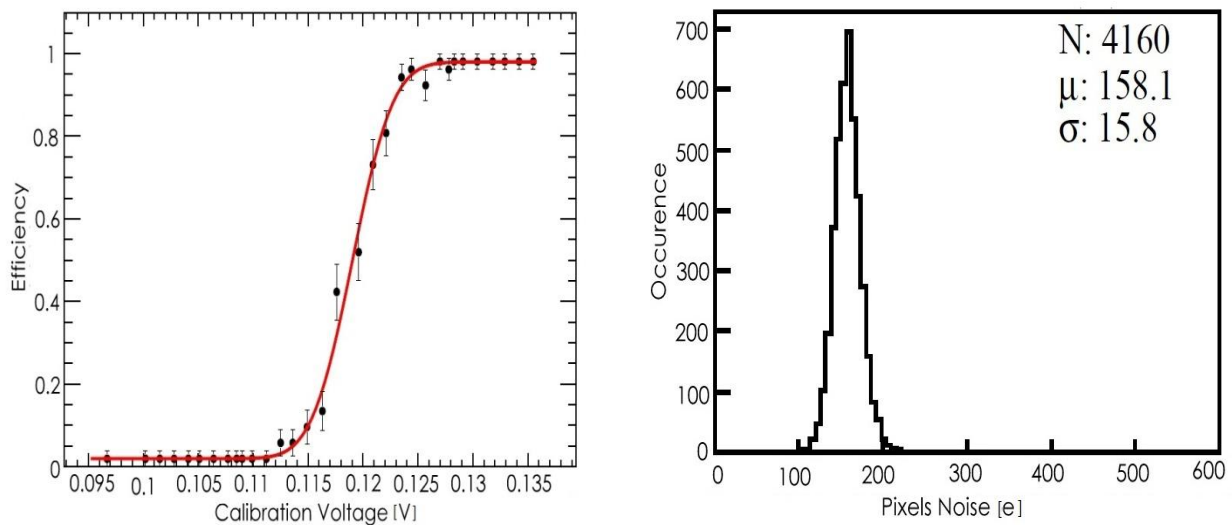


Figure 3.5 (a) S-curve fit with an error function to determine the noise of a pixel. (b) Noise levels determined from the width of the S-curve shown for all pixels.

To test the bump bonding quality, a fast algorithm using the possibility to send a calibration signal through the sensor was devised [3.8]. The calibration signal can either be injected directly to the preamplifier (using switch 1 in Figure 3.6) or to a pad on the ROC surface (using switch 2 in Figure 3.6). Choosing the second option, the calibration signal induces a charge in the sensor, which mimics a hit in the sensor pixel. Ideally, this hit is detected if the bump bond is present and not if the bump bond is missing. For large enough amplitudes of the calibration signal, a hit is triggered although the bump is missing. These hits are supposed to originate from cross-talk via a parasitic coupling between the calibration voltage line and the

preamplifier. Based on practical experience, the comparison between the signal taken by direct calibration signal injection (both switches open and pixel under test disabled) and via the silicon sensor is measured.

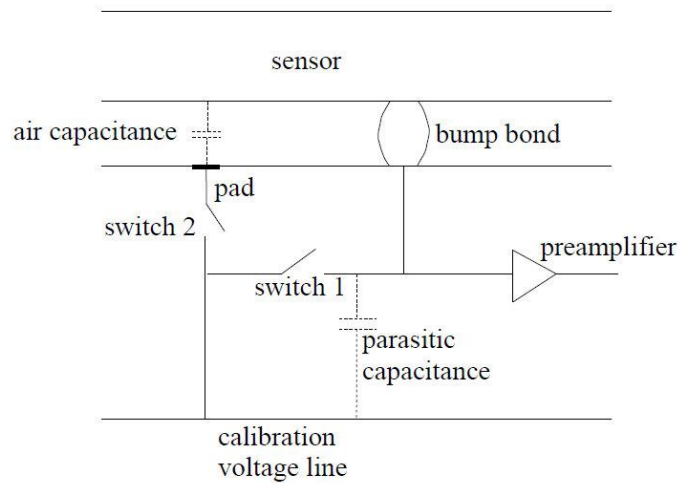


Figure 3.6 Sketch of the PUC components relevant for the bump bonding test

If the bump bond is missing, both thresholds are more or less equal, otherwise the difference amounts to around -30 ADC. The threshold difference distribution of all tested pixels is shown in Figure 3.7(a). The distribution terminates at -13 ADC, where the border between good and bad pixels was set, and presents two entries near the zero representing two bad defects. In Figure 3.7(b) the position in the sensor of these two bad bonding defects is shown.

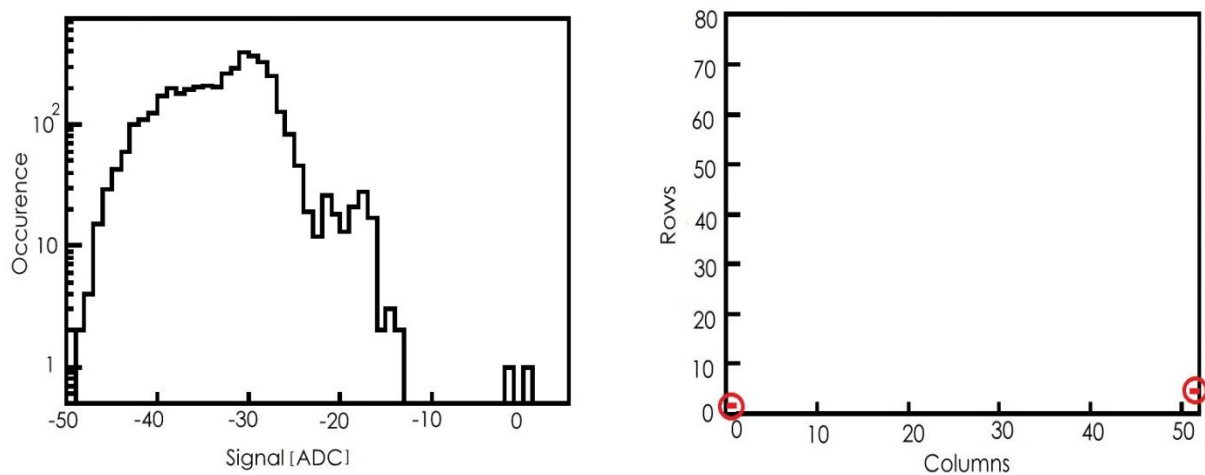


Figure 3.7 Bump bonding test: (a) Distribution of the threshold difference. (b) Map of the bad bump bonds identified. In red the position of the two bad bump bonds.

3.4 Sensor absolute calibration of the CMS pixel sensor

The sensor absolute calibration was performed in the laboratory with the help of a variable energy x-ray source to estimate the number of collected electrons corresponding at 1 ADC. The used source consists of an Amptek EDIX 40 x-ray tube featuring a maximum voltage of 40kV and a maximum current of 200 μ A,

which excites characteristic x-rays from one of two possible targets (molybdenum and silver) producing from five to seven thousand electron-hole pairs in silicon.

In Figure 3.8(a) it is drawn the signal distribution and its fit with the theoretical model, when the sensor is hit by the photons reemitted by an silver target at its typical fluorescence lines. Due to the large dimension of the pixel unit, the charge is always collected by one pixel and charge sharing effect is not appreciable. It is clearly visible the peaks generated by the charge deposited by the photons; the main one is generated by the 22.0keV photons but it is also appreciable the effect of the 24.9keV photons as well.

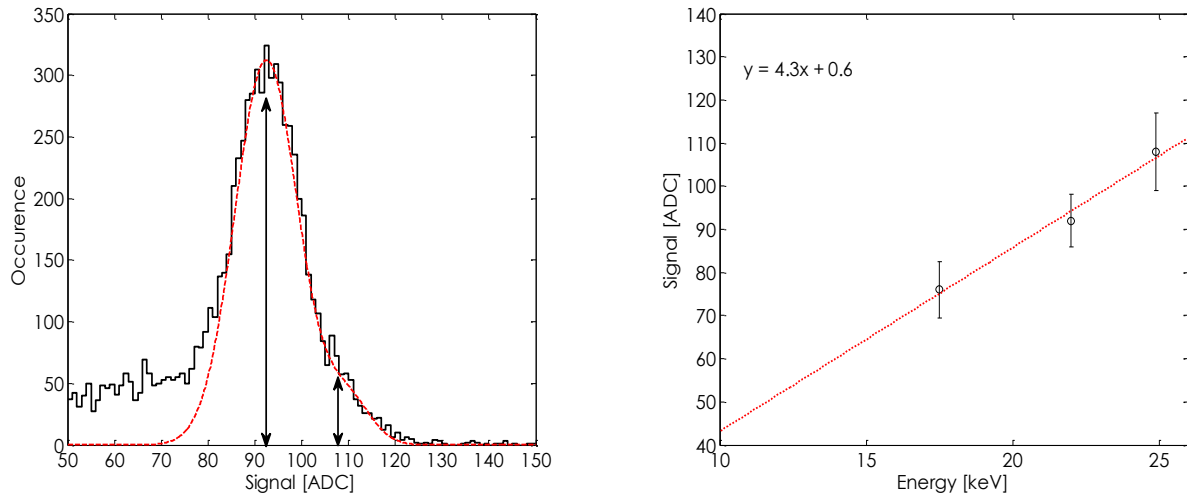


Figure 3.8 (a) Signal distribution of the detected signal due to the silver target emissions. (b) Ionization charge as a function of the Vcal DAC for the ROC under test.

This procedure is repeated for the Molybdenum target and the resulting points in the ionization charge as function of the Vcal signal are fit with a straight line as shown in Figure 3.8(b). The slope is found to be 64.97 ± 10.5 e/ADC while the offset is 87e. Hence a Vcal ADC value of 60 corresponds on average to 3900e and consequently to 14keV.

3.5 Charge particle response for CMS pixel sensor

The detector was put in December 2011 on the 496MeV electron beam at the Beam Test Facility in Frascati to measure the response to a MIP. Figure 3.9(a) shows the map distribution of the electrons hitting the sensor; due to a partial misalignment with respect the beam direction, the majority of the hits lie on the right part of the sensor.

To estimate the amount of signal-sharing among adjacent pixels, for each frame the sum of the signals of the 3x3 submatrix centered on the seed pixel is computed and it is used to normalize the signal of each pixel of the submatrix. In Figure 3.9(b) is shown the distribution of the average fraction for the 3x3 submatrix; most of the signal is concentrated into the seed pixel (84%).

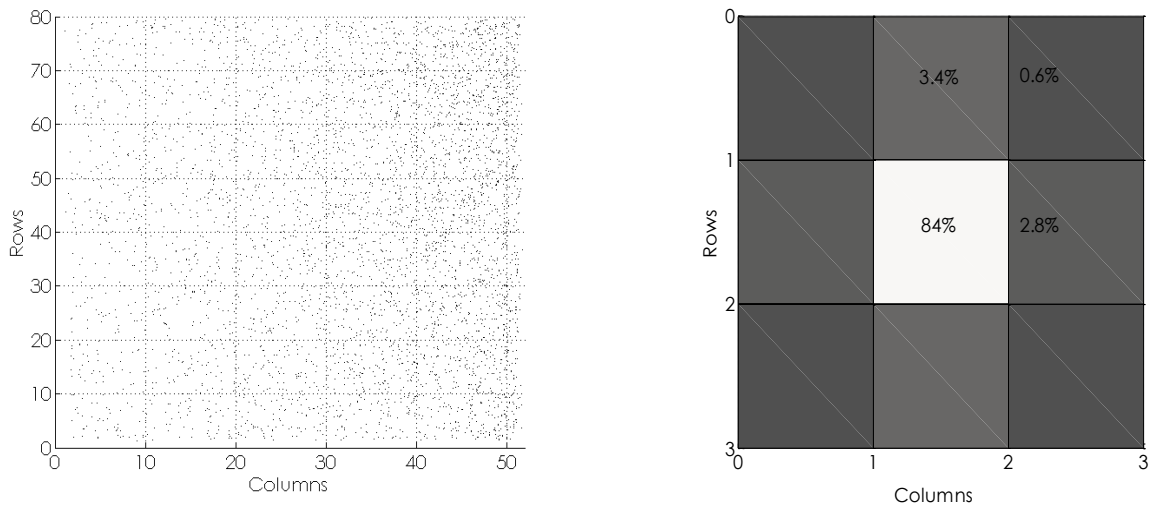


Figure 3.9 (a) Map distribution of the electrons hitting the sensor. (b) Distribution of the collected charge in the 3x3 submatrix around the impact point.

In Figure 3.10 the signal distribution of a 3x3 submatrix, when the sensor is exposed to a 496MeV electrons beam, is shown. The distribution is fitted with a Landau function convoluted with a Gaussian in accordance with the theory reported in Chapter 2. The acquisition threshold is about the 15% of the peak in the main pixel and it does not significantly modify the signal distribution. The peak is located at 384 ± 2 ADC and using the absolute calibration given from the x-ray (65 ± 10.5 e/ADC) we can convert this value in terms of electron-hole pairs resulting in 24950 ± 4165 e. This value is slightly higher than the expected due to the multiple scattering which the electrons suffer in the silicon and to a non-orthogonality between sensor and beam direction.

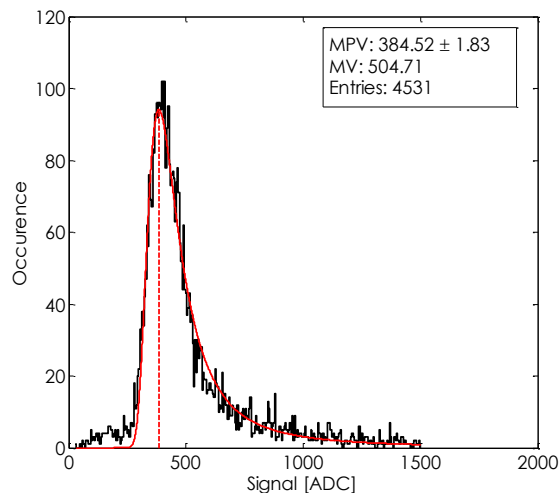


Figure 3.10 Signal distribution of the 3x3pixels cluster exposed to a 496MeV electrons

References

- 3.1 CMS, *the Compact Muon Solenoid: Technical proposal*, CERN-LHCC-94-38.
- 3.2 H. C. Kastli et al., *Design and performance of the CMS pixel detector read-out chip*, Nucl. Instr. and Meth. A 565 (2006) 188–194.
- 3.3 C. Broennimann et al., *Development of an indium bump bond process for silicon pixel detectors at PSI*, Nucl. Instr. and Meth. A 565 (2006) 303–308.
- 3.4 E. Bartz, *The 0.25- μm token bit manager chip for the CMS pixel read-out*, presented at 11th Workshop on Electronics for LHC and Future Experiments (LECC 2005), Heidelberg, Germany, 12-16 September 2005.
- 3.5 Y. Allkofer et al., *Design and performance of the silicon sensors for the CMS barrel pixel detector*, Nucl. Instr. and Meth. A 584 (2008) 25–41.
- 3.6 *ROOT: an object oriented data analysis framework*, <http://root.cern.ch/>.
- 3.7 K. Gabathuler, *PSI46 pixel chip - external specification, internal document of the CMS Barrel Pixel collaboration* (2004).
- 3.8 A. Starodumov et al., *Qualification procedures of the CMS pixel barrel modules*, Nucl. Instr. and Meth. A 565 (2006) 67–72.

Chapter 4.

Radiation Active Pixel Sensor RAPS03

The RAPS03 is the third prototype of a series of pixels sensor developed within a collaboration among the Università di Perugia, the Università di Parma and the Istituto Nazionale di Fisica Nucleare (INFN) of Perugia in order to analyze the capability of such class of sensors in the detection of ionizing particles [4.1]. The RAPS03 chip implements a 6.55mm^2 detector matrix for direct-charge particle revelation, with fast and re-configurable read-out electronics. It counts about 64k APS pixels, featuring $10\times 10\mu\text{m}^2$ size (Figure 4.1). The structure is divided into 4 sub-matrices (called ESAS and ESAL), each counting 128×128 pixels and equipped with its own read-out logic, so that the sensor features 4 parallel analog outputs. The matrices are read row by row from the lower left corner to the upper right. Also some other test structures, aimed at comparison with alternative architectures and characterization of electronic devices on the chip are included.

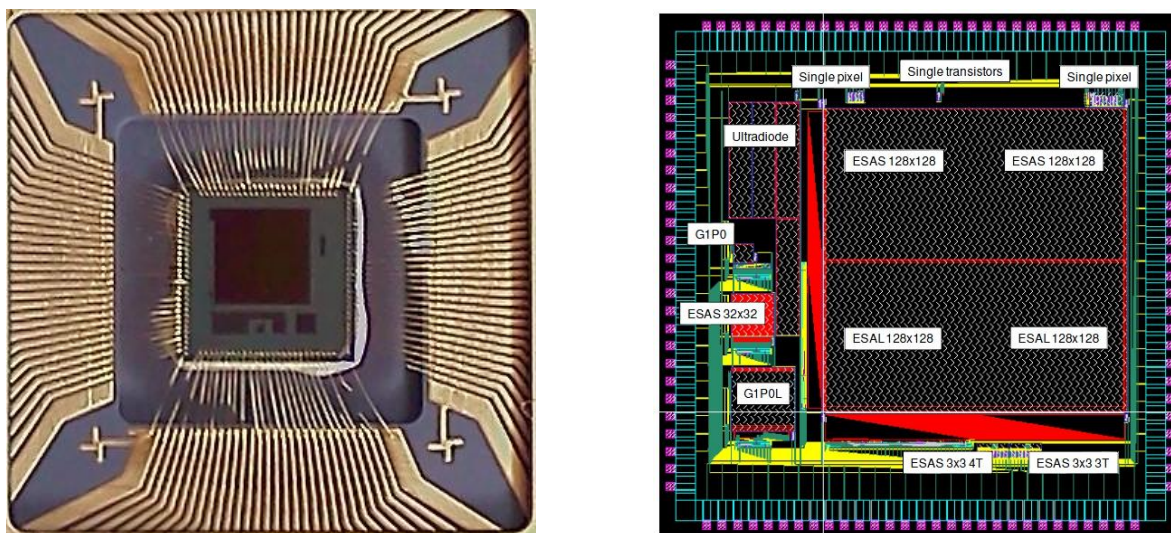


Figure 4.1 (a) Picture of the RAPS03 detector; (b) layout of the RAPS03 chip.

Two alternative pixel topologies were implemented in different sub-matrices, differing in the photodiode size (geometrical fill factor ranging from 4% up to 77%). The system is capable of continuous detection (typical of imaging/trigging applications), but can also be coupled with an external trigger (needed for some HEP applications). Reset and integration periods are digitally configurable time intervals in a very

large range (from 1 to 4×10^6 clock cycles). The detector can thus be used in both highly and dimly illuminated environment. All pixels are reset simultaneously (global shutter approach) and then serially read by means of an analog multiplexer. The column source-follower circuits can be biased by setting an external voltage (V_{pol}), allowing for adapting the tradeoff between read-out speed and dynamic range to the actual illumination condition.

The following work is focused on the four 128×128 matrices; for this reasons only the layout of the corresponding pixels will be described in detail.

4.1 The ESAS and ESAL pixels

The ESAS and ESAL pixels feature the standard three transistors architecture and $10 \times 10 \mu\text{m}^2$ area. The difference among the two layouts is the dimension of the photodiode n_{well} ; for the ESAS (see Figure 4.2(a)) the n_{well} , placed at the centre of the pixel, is $2 \mu\text{m}$ by $2 \mu\text{m}$ with an area of $4 \mu\text{m}^2$; for the ESAL the n_{well} embraces almost all the pixel with about $77 \mu\text{m}^2$ area occupancy (see Figure 4.2(b)). The two different solutions have been chosen in order to evaluate the differences among a pixel with minimum capacitance and a pixel with the maximum fill factor. In the first case the pixel should have a better charge voltage conversion factor but an higher noise; in the second case the higher capacitance reduces the noise but the charge voltage conversion factor is lower as well [4.2].

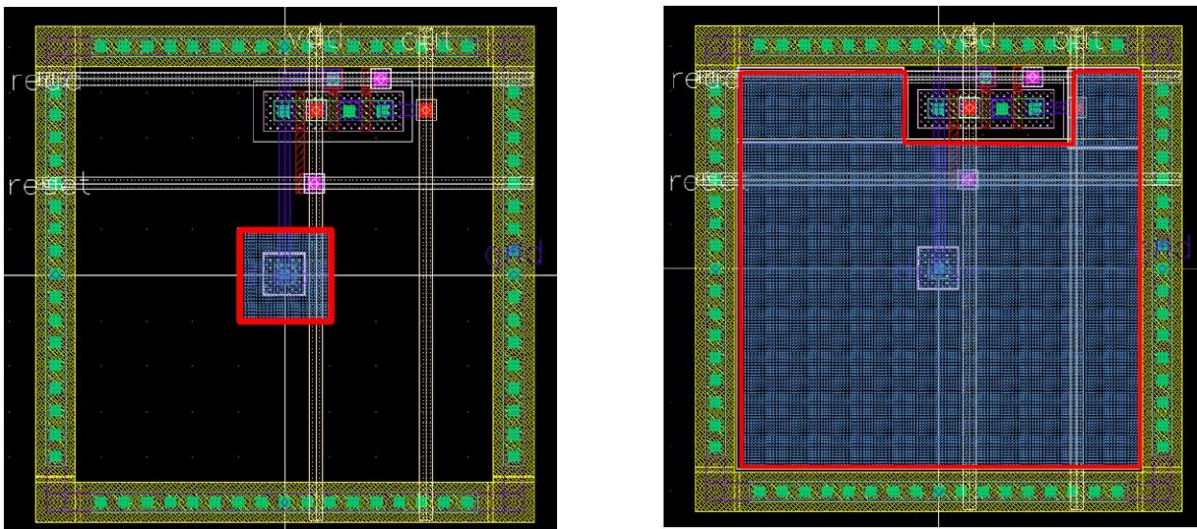


Figure 4.2 (a) Layouts of the ESAS and (b) the ESAL pixels, the red line indicates the dimension of the n_{well} .

4.2 The RAPS03 data acquisition system

As already mentioned all the matrices have analog outputs, hence, in order to read, record and elaborate the signal detected by the sensor, we need an analog to digital conversion system. Such a conversion has to be performed off-chip. The Figure 4.3 shows the typical shape of an analog output of a RAPS03 matrix.

During the reset interval T_{rst} the output buffer is disconnected from the matrix and the output voltage is equal to the lower saturation voltage of the buffer. Then the buffer is connected with the first pixel of the matrix, showing as output the voltage of that pixel. After a given integration interval T_{int} the scanning of the matrix starts. On the output line is then available, for a period of an entire clock cycle T_{ck} , the voltage of one pixel of the matrix.

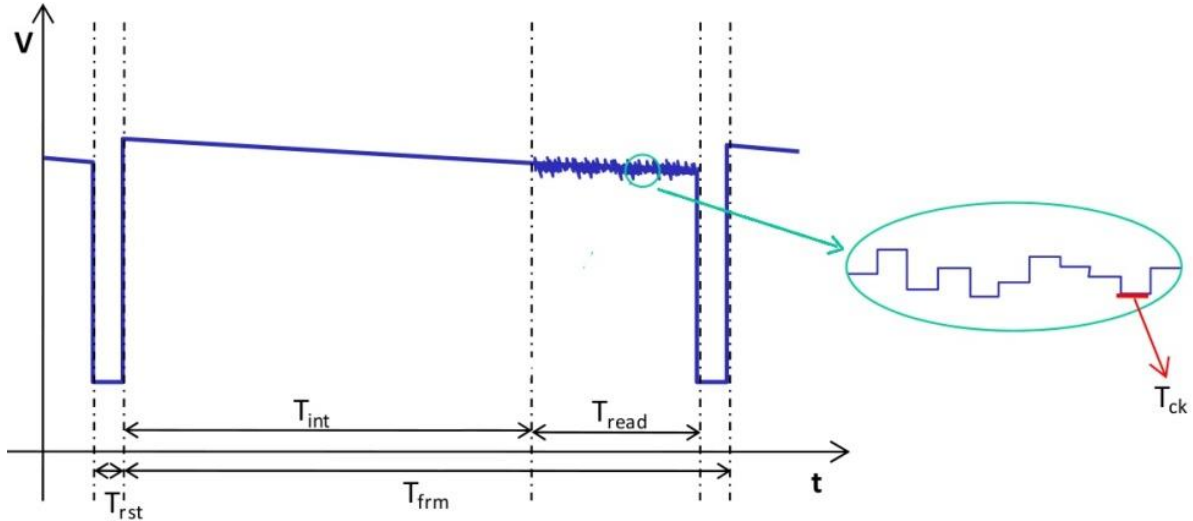


Figure 4.3 Illustration of a typical output voltage of a RAPS03 matrix

Digital signals are also present to assure the correct operations of the RAPS sensors (i.e. to control Clock and Reset, to read and write registers and to synchronize the lecture of the pixel matrix signals). To read the sensor and to cope with all these signals a dedicated fully custom analog to digital acquisition system has been developed.

4.2.1 Requirements of the Digital Acquisition System

The aim of the digital acquisition system (DAQ) was to read four matrices of four different chips simultaneously. This requirement was necessary for measuring typical particle sensor parameters such as the spatial resolution and the detection efficiency, for which we need the comparisons between the data collected simultaneously by at least three sensors aligned one in front of each other (standard telescope configuration).

Measurements have been performed before the development of the DAQ system, to collect information about the dynamic range, the output impedance and the frequency domains of the outputs (see [4.3] for details). The outputs of the chip are all single ended with positive dynamic with respect to the ground potential. In Figure 4.4(a) and (b) are shown respectively the minimum and the maximum output voltage values as a function of the V_{pot} . From these values and from the analysis of expected noise (about 1mV) it was retrieved the necessary resolution of the analog to digital converter: a 12bit ADC was chosen.

After the analog to digital conversion, the data must be transferred to a personal computer where it is possible to display, elaborate and record them. The required bandwidth between the DAQ and the

computer was 300 FPS x 16384 pixel x 4 matrix = 236 Mb/s, supposing to transfer for each pixel only the average of the good samples. The bandwidth of an USB2.0 (480Mb/s) was enough.

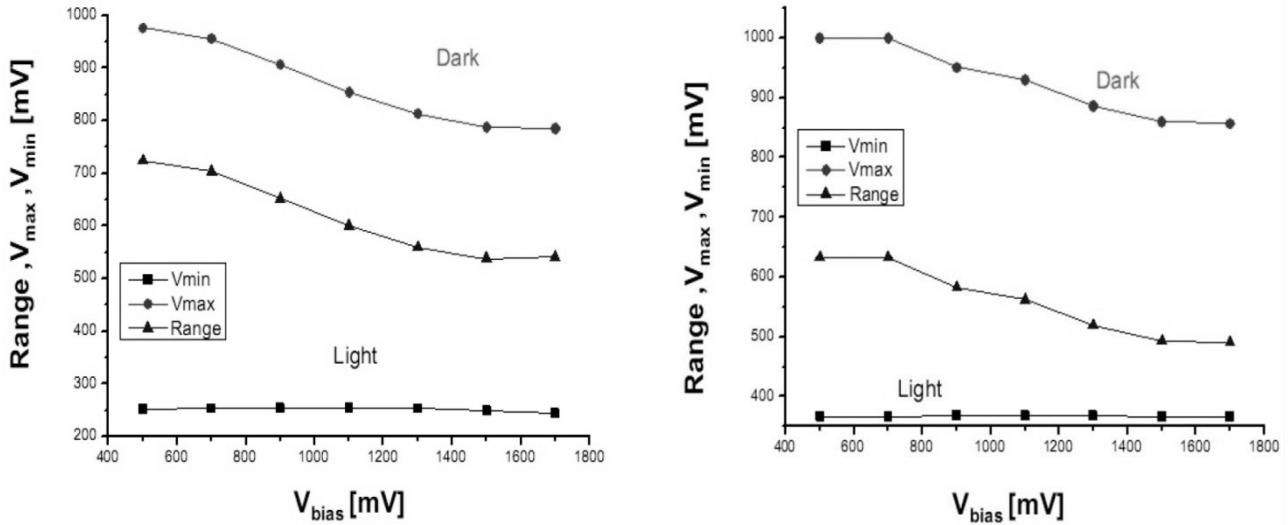


Figure 4.4 Minimum (square line) and maximum (circle line) output voltage of a RAPS03 matrix and its difference (triangle line) in function of the Vpol for the ESAS (a) and the ESAL (b).

4.2.2 DAQ architecture overview

The Figure 4.5 shows the DAQ system overview. Two analog to digital converters AD9238 allow to read up to four different sensors; each of these converter has two differential inputs which are converted in parallel with a 12bit resolution and a frequency up to 65MSPS [4.4].

The overall system is based on an Opal Kelly XEM3050-4000p which is equipped with a Xilinx Spartan3 XC3S4000, a built-in USB2.0 interface, 32MB SDRAM, a PLL and some other features [4.5].

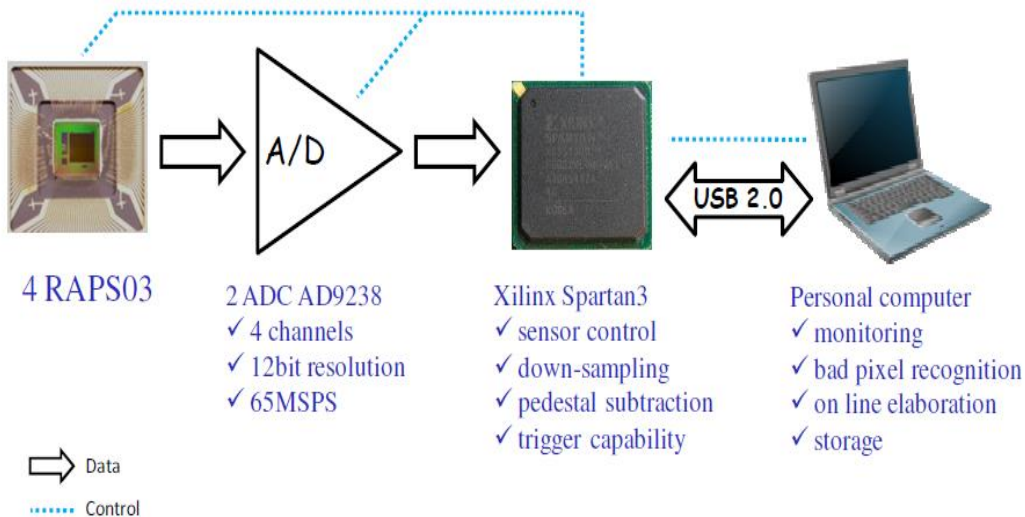


Figure 4.5 DAQ system overview. The black arrows indicate the data paths while the blue dotted line the control paths

The Xilinx Spartan3 FPGA controls all the sensors and the ADCs; moreover, it is capable to perform:

- the down-sampling of the acquired data: cutting off all the unwonted samples, at the beginning of each pixel interval, and making the average of the good samples where the signal is stable;
- the pedestal subtraction to compensate the fixed pattern noise of the matrix;

- the generation of a programmable triggering among the four acquired sensors and two additional external digital inputs.

The FPGA communicates through a USB2.0 interface with a personal computer from which it is possible to control the whole system. To allow for the telescope configuration, a flexible geometry to host separately the chips has been implemented: each of the four sensors has been placed in an independent printed circuit board. Each of these four boards is connected through a 96 pin connector to a motherboard which has the functions to generate all the voltage supplies needed by the sensors and to amplify their analog outputs.

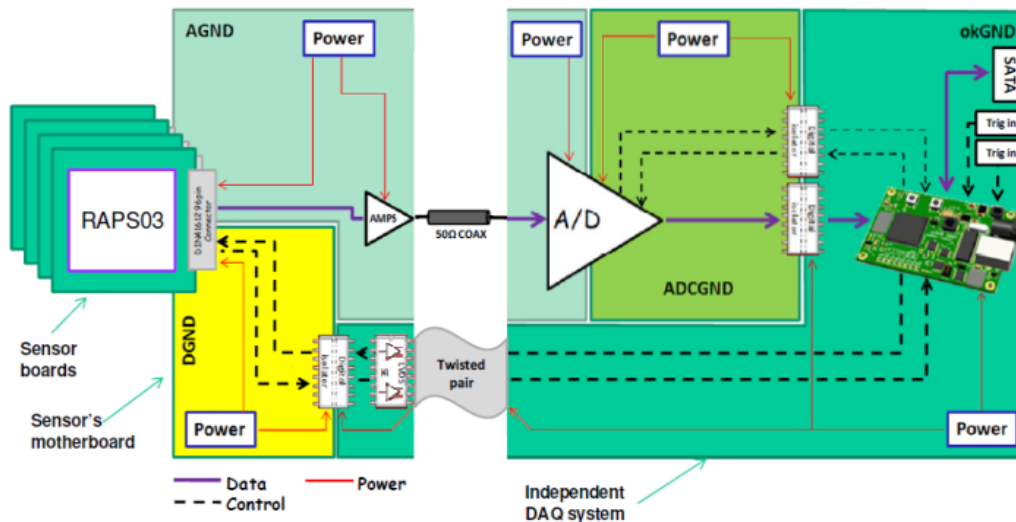


Figure 4.6 Schematic illustration of the RAPS03 DAQ hardware with different ground potential domains

The digital lines, from and to the sensors, travel through a twisted pair cable between the motherboard and the DAQ section after the conversion in LVDS format, with all the benefits of this standard.

There are many advantages from this subdivisions:

- The small independent sensor boards allow the positioning of the sensors one in front of each other or in more complex mechanical configurations, allowing for flexible geometry;
- The block on the right side in Figure 4.6 is an independent and reusable DAQ system with 4 analog input, 10 LVDS digital inputs, 10 LVDS digital outputs, two digital trigger inputs and the powerful XEM3050;
- The motherboard can also be reused to hold other sensors: the entire system, in fact, has been reused for the next sensor prototype.

To reduce as much as possible the noise, particular attention has been paid to the ground potentials. The digital lines with their fast transitions, for example, can induce noise on the analog section if the two domains are not properly isolated. For this reason and to avoid possible ground loop, in the circuit have been individuated and isolated four different ground domains. Each ground domain has its independent power section and each section has its independent power supply input.

4.2.3 Mechanics

The arrangements of all the boards and cables of the measurement setup, its electromagnetic shielding and the mechanic interface to hold it on the experimental area have been studied, before their realization, with the assistance of a mechanical CAD named SolidWorks [4.6].

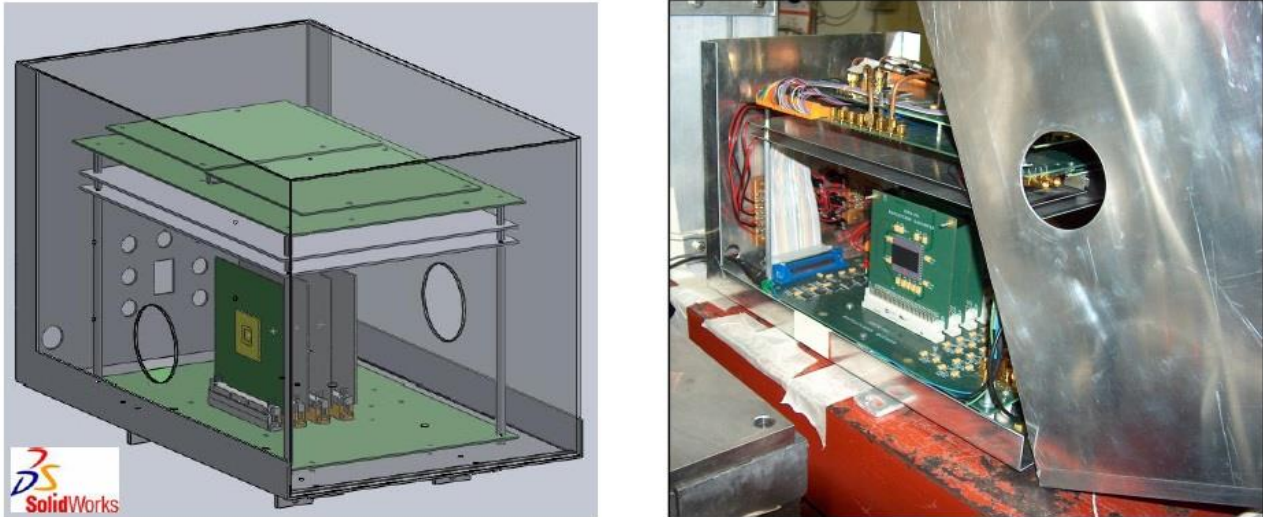


Figure 4.7 (a) CAD drawing of the boards arrangement and their shielding; (b) A photo of the setup.

The Figure 4.7(a) shows the mechanical drawing of the boards arrangement and the metallic box used to shield the electronics from external interference. On the box has been held a single connector for the power and all the fuse holder; there are also two holes for the incoming (front) and outgoing (rear) particles beam. The Figure 4.7(b) is a picture of the realized DAQ system at work in an irradiation facilities.

4.2.4 Software

A complete software has been developed to communicate with the FPGA and set the working conditions of the sensors. The environment used for the acquisition software is LabVIEW [4.8]; it is a powerful instrument for the data acquisition because of the ease to draw graphic interface and its graphical programming technique, which does not require to know the syntax and the semantic of a programming language. The Figure 4.8 shows a screenshot of the virtual instrument panel built for the RAPS03 DAQ system.

The functions implemented into this software can be summarized as in the following:

- *Configure the FPGA with a .bit file*; the bit file which contains the FPGA code is downloaded into the Spartan3 at startup.
- *DAQ configuration*; from the graphical interface the user can set all the acquisition parameter such as the trigger configuration, the pedestal subtraction and the delay of an external trigger.
- *Sensors configuration*; the user can vary the parameters that set the sensors functionality (essentially the clock frequency and the integration time) and send the asynchronous reset.

- *Data storage*;
- *Pedestal calculation*; a defined number of frame can be collected and used to define the pedestal.
- *Mask calculation*; to avoid fake particles recognition, a pixel mask is automatically retrieved from the acquired data.
- *Real time display*;
- *Real time analysis and plot*; some analysis, like the computation of the cluster signal distribution, can be performed and displayed in real time.

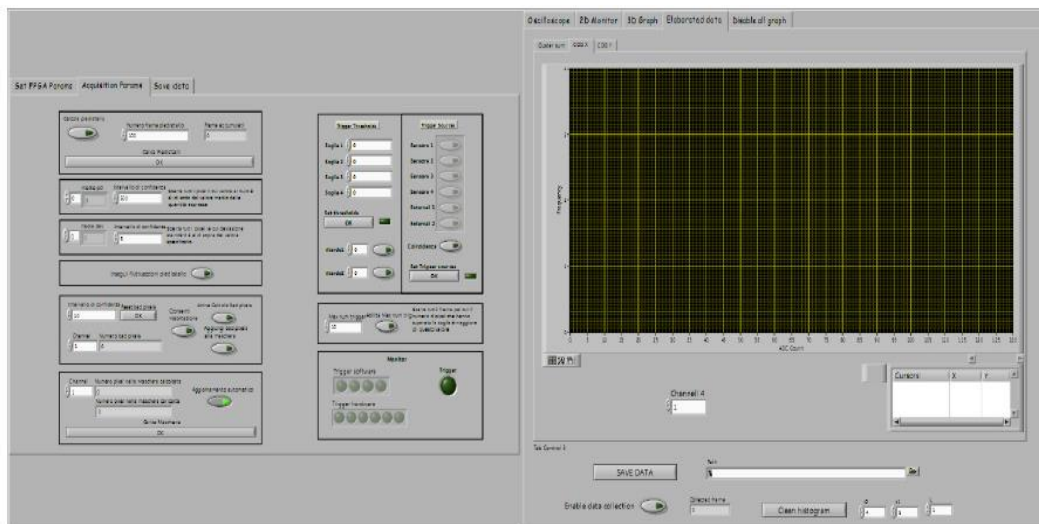


Figure 4.8 Panel of the virtual instrument used with the RAPS03 DAQ system.

4.2.5 Firmware

The FPGA has been programmed in VHDL language using the Xilinx ISE Foundation software pack. In Figure 4.9 it is shown a scheme of the logic implemented into the FPGA. A Data elaboration unit receives the data from the ADCs and, by means of the synchronization signals given by the sensors, it is able to assign each sample to the corresponding pixel. Setting properly the registers of this unit, it is possible to collect only the samples corresponding to the interval where the signal is stable. This unit, if desired, can also perform the pedestal subtraction with the data stored in the Pedestal RAM. A Trigger unit compares all the pixels values with the data stored in a specific register (named *Threshold*) detecting if one or more pixels in a frame cross that threshold; some pixels can be excluded by this operation if belonging to the pixel masked matrix. A Trigger logic checks all the internal and external trigger inputs and if the condition matches with the user requirements transmits this information to the main State machine.

The pedestal and mask RAM, the trigger unit with its threshold register and the data elaboration unit (all the blocks surrounded by a dashed box in Figure 4.9) are replicated for each of the four input channels corresponding to the four ADCs and sensors.

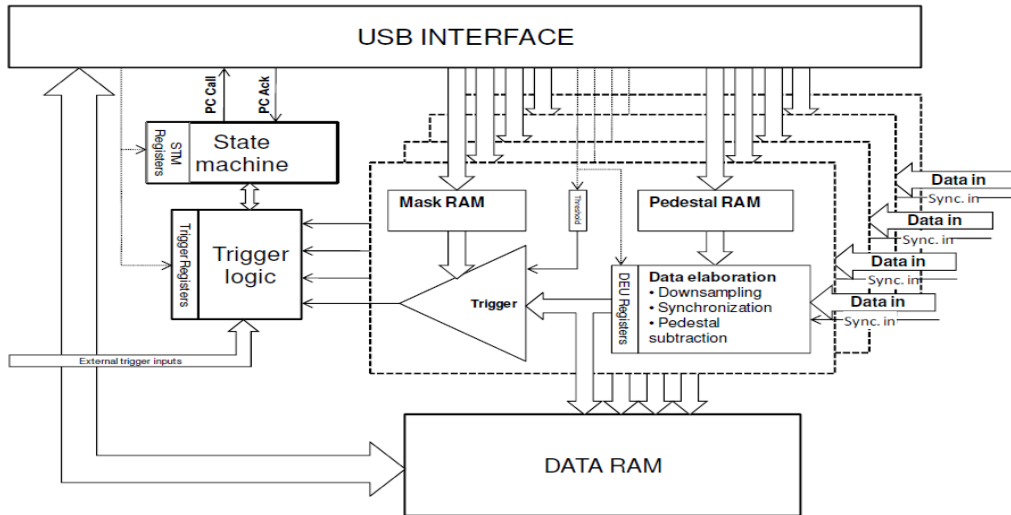


Figure 4.9 Block diagram of the code implemented into the FPGA

4.3 Noise analysis

In this section will be analyzed the noise of the two ESAS and the two ESAL matrices. For simplicity the structures will be named as in Figure 4.10 where it is shown their locations.

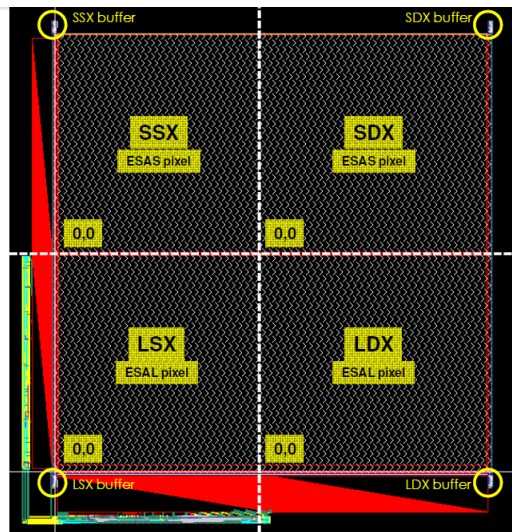


Figure 4.10 Layout of the four 128x128 pixels matrices; the upper two have an ESAS pixel, while the lower ones an ESAL. It is also underlined the locations of the four analog buffers and the first pixel of each matrix

4.3.1 Fixed pattern noise FPN

When a matrix of pixels is in dark condition or exposed to an uniform illumination, the pixels are not at the same level. Due to the inevitable differences among the pixels, caused by unavoidable non-uniformity in the realization processes, each pixel has a different level. This phenomena is define as *Fixed Pattern Noise* (FPN). The FPN represents the offset to subtract to all the frames in order to get the right signal produced by the radiation. In the following, when we talk about the signal read by a sensor, we always

refer to the difference between the real signal read by that sensor and the FPN. In Figure 4.11(a) the FPN of LDX matrix was evaluated, by averaging the pixel response on 500 consecutive frames.

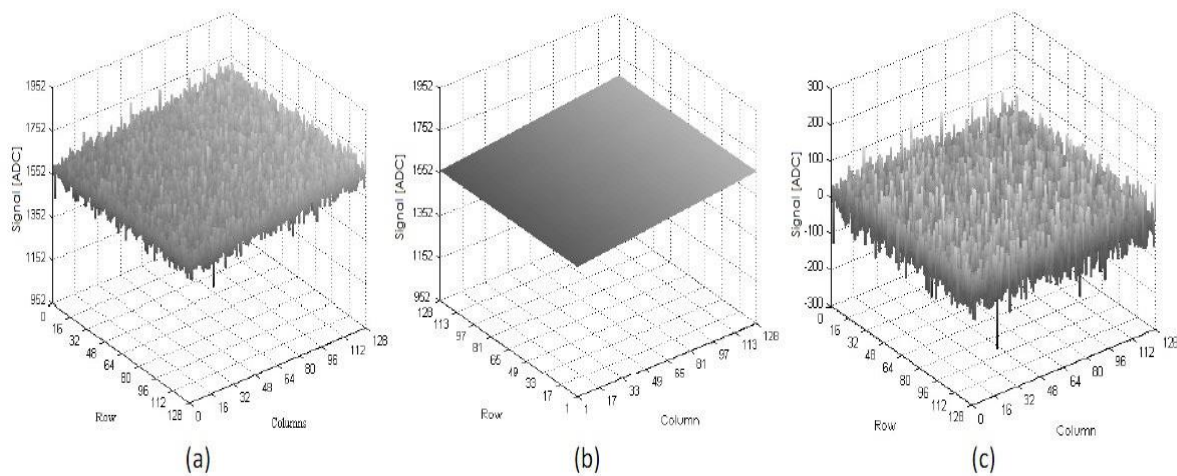


Figure 4.11 (a) Response of LDX matrix in dark condition; (b) with its linear regression to a plane; (c) the relative residues

As can be seen there is a component of the signal that rises linearly with the column number; using a multiple regression algorithm the plane shown in Figure 4.11(b) can be extracted. Subtracting this interpolating plane to the measured FPN the values are brought back all around zero (Figure 4.11(c)).

In Figure 4.12 it is shown the distribution of these residuals for the LDX matrix. The distribution has a Gaussian shape with a standard deviation of few tens of ADC (see Figure 4.12(a)). Increasing the integration time the shape starts to be slightly different from the Gaussian; in Figure 4.12(b) this behavior is emphasized using a logarithmic scale, showing the differences at the left of the Gaussian lobe.

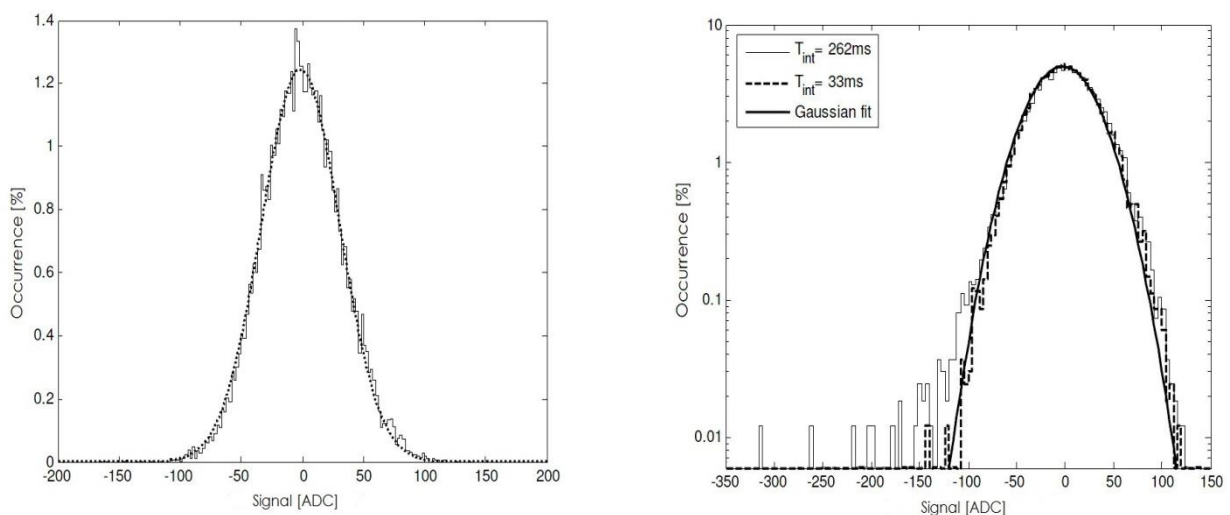


Figure 4.12 (a) FPN distribution after subtraction of the interpolating plane of the LDX matrix. (b) The comparison between the FPN distribution calculated at 33 ms and 262ms of integration time

Because of the different pixel dark currents, the pixels signal decreases in a incoherent manner as the integration time increases. In fact some pixels go towards the discharge faster than others.

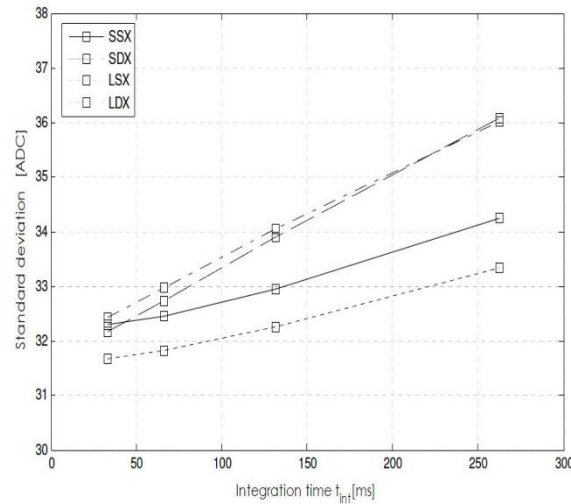


Figure 4.13 Standard deviation at different integration time plotted for all the four 128 by 128 pixels matrix.

This aspect leads to the increasing of the standard deviation of the Gaussian distribution as a function of the integration time, as clearly is shown in Figure 4.13. An additional correction pixel by pixel will be then needed for improving the sensor functionality.

4.3.2 Signal pixel noise

Noise is generally defined as a unwanted random addition to a signal; in our case the noise can be defined as the fluctuations which occur in the pixel signal around its pedestal from an acquisition to another. The main cause of this fluctuation at the pixel level is the so called kT/C noise [4.9]; but there are some other contributions which increase the level of measured noise as the noise of read-out buffer, the quantization noise, external electromagnetic interference, bonding, cables, PCB board, etc.

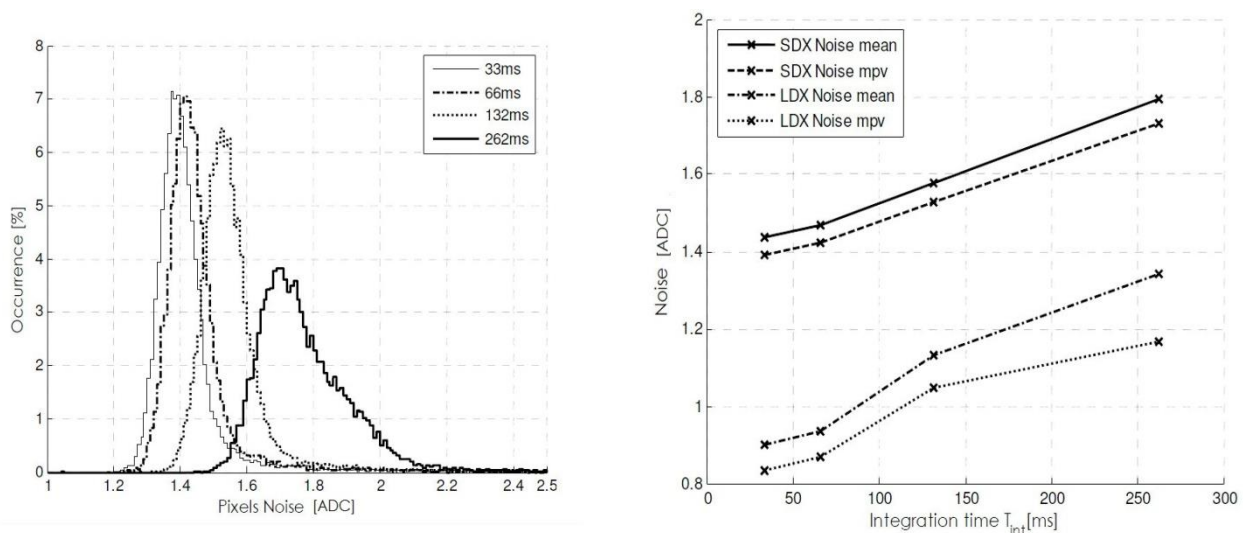


Figure 4.14 (a) Distribution of the single pixel noise for all the pixels of an ESAS matrix measured for different integration times. (b) Most probable value and mean value of the single pixel noise of the ESAS and ESAL matrix, at different integration times.

The Figure 4.14(a) shows the distribution of the single pixel noise for the SDX matrix at different integration times. The mean noise rises almost linearly with the integration time, spreading their values

within a larger interval. Due to the asymmetric shape of the distribution the mean value of the measured noise, for a given matrix, differs from the most probable value.

In Figure 4.14(b) are drawn both quantities. As expected the noise is smaller for the matrices with the large photodiode because of its larger capacitance (indeed the term C occurs at denominator in the expression of kT/C noise power). Another aspect that can be noted is the dependence of the noise on the integration time: the kT/C noise is, by definition, independent by the time, but this is not true for other contributions such as the leakage current (i_l).

During acquisition operations, usually, the signal of each pixel is compared with a certain threshold; if the threshold is crossed it is assumed that a particle has hit the detector and the corresponding frame is stored. Usually the threshold must be as low as possible for detecting weak signals but the noise puts a lower limit to this parameter. Fake crossings, caused by noise, can occur. Avoiding that is of relevant importance because they may get worse the quality of the acquisition setup.

Each frame is composed by $N_p = 128 \times 128 = 16384$ pixels, assuming the same Gaussian noise for each pixel with a standard deviation σ the probability P_{FH} to have a fake hit is given by:

$$P_{FH} = 1 - p^{N_p}$$

$$p = \int_{-\infty}^T g(x) dx \quad (4.1)$$

$$g(x) = \frac{1}{\sigma\sqrt{2\pi}} \exp\left(-\frac{x^2}{2\sigma^2}\right)$$

where p is the probability of not crossing the threshold T on a pixel and $g(x)$ is the Gaussian function; using the normalized threshold $\tau = T/\sigma$ the Eq. (4.1) becomes:

$$P_{FH} = 1 - (1 - Q(\tau))^{N_p} \quad (4.2)$$

$$Q(x) = \frac{1}{\sqrt{2\pi}} \int_x^{\infty} \exp\left(-\frac{t^2}{2}\right) dt$$

where $Q(x)$ is the so called *Q-function*. The P_{FH} can be estimated with the ratio between the number of frames which have crossed a certain threshold on the total frames acquired during an acquisition in dark condition. The measured P_{FH} is reported in Figure 4.15 with a dotted line. As can be seen the measured quantity differs drastically from the theoretical one. The number of frames which cross the trigger is still over 15% at ten times the most probable noise value of the observed matrix. From the trigger check can be used to exclude all the noisy pixels, that are all the pixels with a measured noise greater than the average one. However, this method is not enough effective to reduce the fake hits. The dashed-dotted line in Figure 4.15 represents the probability measured excluding all the pixel with a noise greater than the most

probable noise value for the given matrix (an unrealistic value because about the 65% of all the pixels will be excluded from the check), but the result is still insufficient.

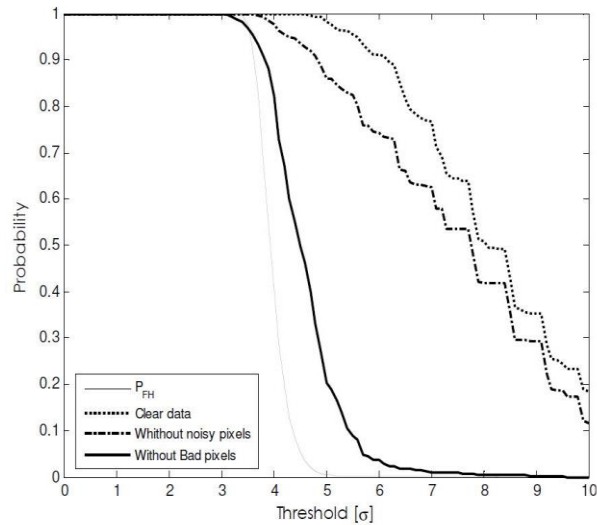


Figure 4.15 Comparative between the theoretical probability of fake hit (P_{FH}) in function of the threshold and the measured ones (SSX matrix). The bold curves represent the measured probability including into the trigger control: all the pixel (dotted line); only the pixels with noise less than the most probable one (dashed-dotted); excluding the Bad Pixels (solid).

An explanation of this behavior is that there are some pixels which have not a Gaussian noise, as shown in Figure 4.16 where it is reported the evolution of the signal (the graph on the left) and its cumulative distribution (on the right) measured on a particular pixel of the SSX along about 500 consecutive frames.

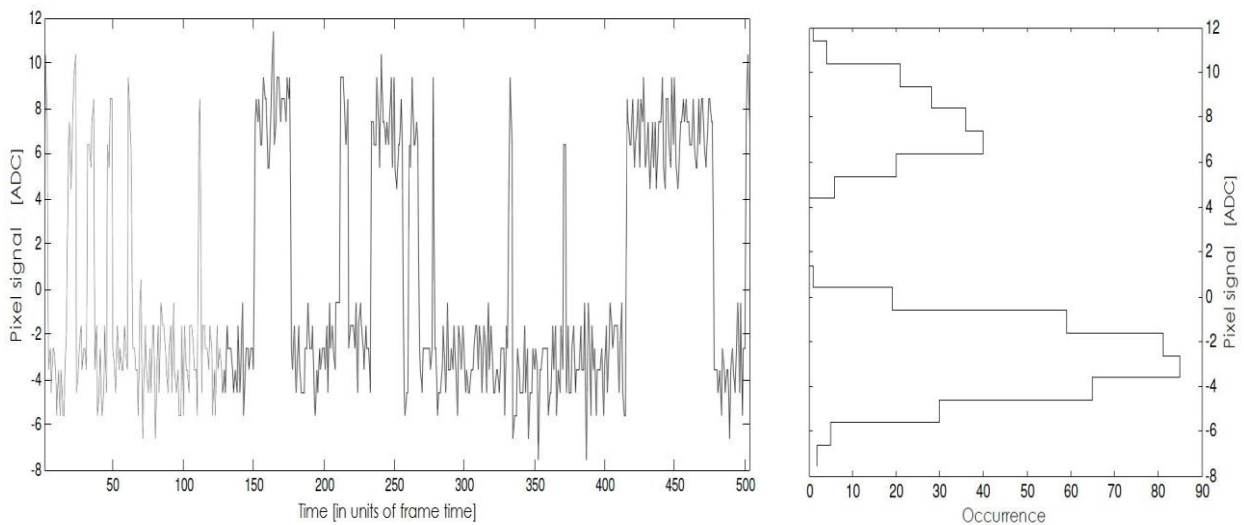


Figure 4.16 (a) Signal measured on a pixel of the SSX matrix during about 500 consecutive frames and (b) its cumulative distribution.

If we measure the standard deviation of this pixel, for example between the 300th and the 400th frame, we will find a value compatible with the most probable noise value of the matrix and we wrongly do not exclude that pixel from the trigger check, though the leaps clearly visible in the figure could generate fake hits. To find these undesired pixels we can look at the occurrence with which the pixels cross the threshold. If, on a pixel, the number of fake hits is much greater than the average, that pixel can be marked as *Bad* and removed from the trigger control. The solid-dotted line in Figure 4.15 represents the probability measured excluding all the bad pixel. The line now looks very close to the measured P_{FH} .

4.4 X-ray response of the ESAS and ESAL matrix

The sensor has been tested using a variety of photon sources with several energy in the soft x-ray range either to verify its response than to derive the absolute calibration. The frames are continuously acquired by the DAQ and recorded for offline analysis if at least one pixel signal, called seed, is over a threshold bigger than 10 times the pixel noise.

The response to a single photon not always is well confined within few pixels; the signal sharing may be caused by either the diffusion of the electron-hole pairs than the electronic cross-talk among adjacent pixels. To reconstruct correctly the signal generated by an incoming photon the concept of cluster of pixels has been introduced. A cluster is defined by starting from the seed pixel; then all the pixels included in the 3x3 submatrix centered on the seed are tested to see if their signal is bigger than the adjacent threshold value (V_{ad}), in which case the pixel is added to the cluster; the procedure is repeated for the outer ring of 5x5 submatrix to select pixels with signal over V_{ad} and topologically connected to the cluster, and so on. When the cluster is composed only by the seed it is called monopixel cluster. Only the monopixel clusters have been selected for calibration purposes.

4.4.1 Sensor absolute calibration of the ESAS matrix

The following tests have demonstrated the capability of the ESAS to detect single x-ray photons produced by the x-ray tube, exploiting the direct conversion of the photons into the silicon without scintillator or particular expedient. The analysis have been performed considering a 3x3 pixels clusters with a threshold $T=18$ ADC at least (about 15 times the single pixel noise σ) and a V_{ad} imposed at 4 ADC (about 3 times the single pixel noise σ).

In Figure 4.17(a) it is drawn the signal distribution of the monopixel clusters, and its fit with the theoretical model, when the sensor is hit by the photons reemitted by an iron target at its typical fluorescence lines. It is clearly visible the peaks generated by the charge deposited by the photons; the main one is generated by the 6.5keV photons but it is also appreciable the effect of the 7.1keV photons as well. The distribution at the left of the main peaks represents all the cases where the photons interact deeply in the silicon or in a *death zone* of the pixel and the photodiode is not able to collect all the generated charge. To better understand how the generated charge diffuses in the silicon the cluster signal has been studied as a function of the number of pixels belonging to its.

In Figure 4.17(b) three regions are clearly identified in the plot:

- the noise region (blue circle in the lower left part) where the pixels that reach the threshold level used during the acquisition can be found;
- the partially collected region (green square in the upper part) where are localized the events where an important part of the charge is not collected due to the interaction depth of the photon and to the limited capability of the small n_{well} to capture all the generated charge;

- a monopixel region (red circle in the lower right part) where there are the data corresponding to a fully efficient charge collection.

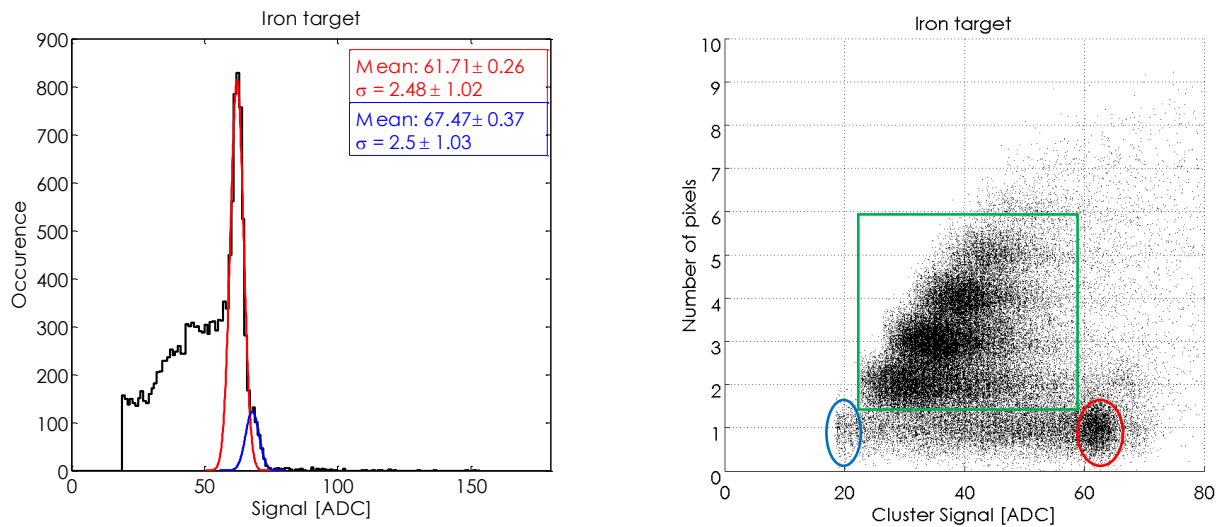


Figure 4.17 (a) Signal distribution of the ESAS monocluster pixels due to the iron target emissions. (b) Correlation among cluster signal and number of pixels in the cluster

In the following are shown the correlation plots for different kind of target material and therefore for different photon energies. It is evident how increasing the energy of the photons, the number of monopixel clusters dramatically goes down with respect to the multipixel cluster.

According Eq. (2.30), increasing the energy of the photons the generated photoelectron can move in a larger areas of silicon releasing charge within more than only one pixel. In fact when the Iron target is used, the cluster is composed mainly by 2.7 pixels; this number becomes 3.2 with the Lead target, 5.0 with the Molybdenum target and 6.4 with the Cadmium target. For the Silver target it is difficult to find the average size of the cluster because of the non negligible contamination of Copper in the target, which causes emission of photons at lower energies. Another relevant aspect appears from Figure 4.18. The multipixel clusters show an important charge collection lost of the order of 30-50%.

This can be due basically to two aspects:

- when a photon interacts among two or more photodiodes, there is a considerable loss of charge due to the small n_{well} and to the associated depletion region which does not extend in all the pixel area and therefore the charge generated far from the photodiode recombines, escaping to the collection.
- in case of deep interaction the charge generated move toward the surface spreading among two or more pixels recombining itself during the path. For this reason these photons will be detected with a lower signal than the original one.

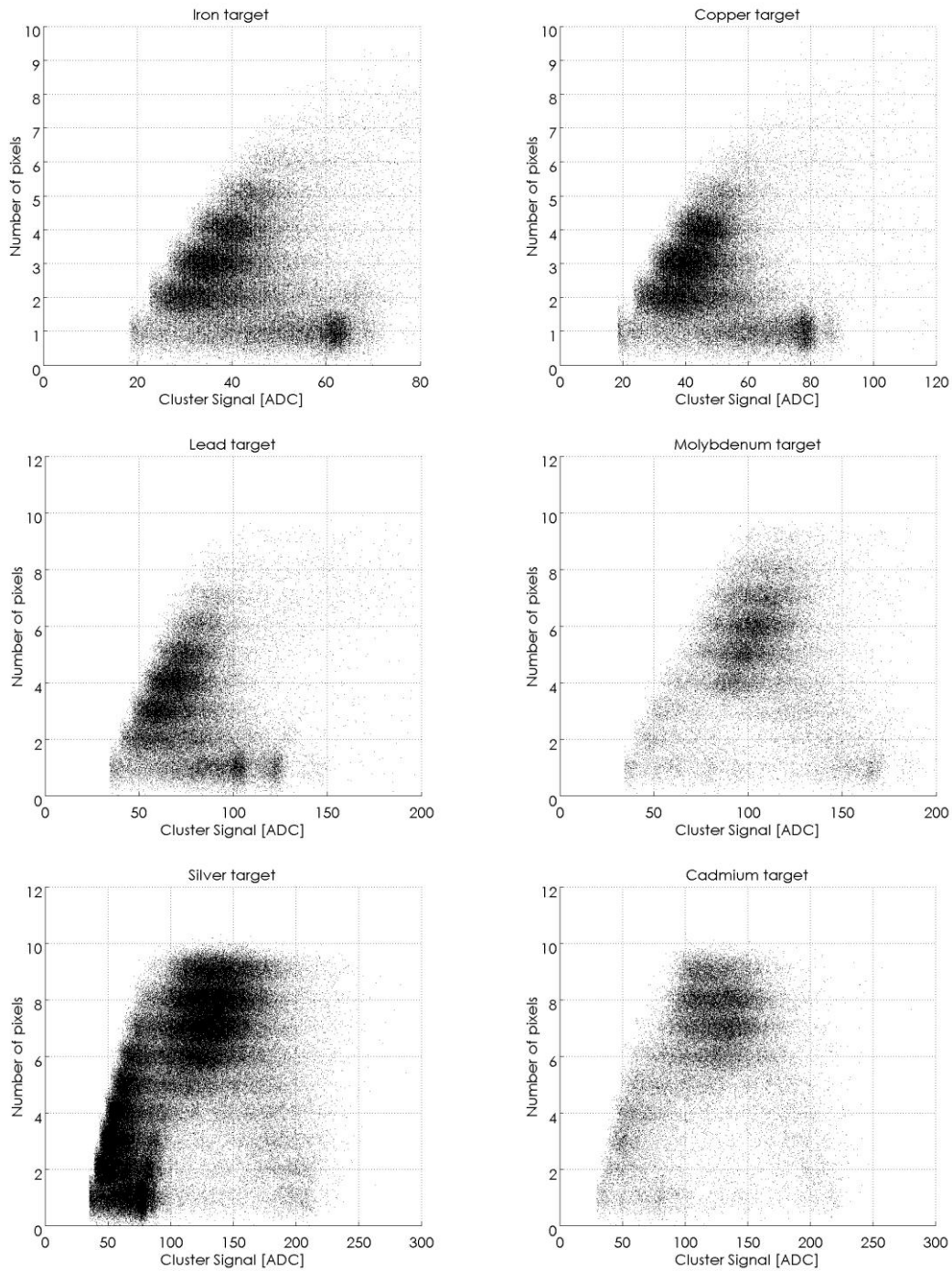


Figure 4.18 Correlation among cluster signal and number of pixels in the cluster due to the emission respectively of: (a) iron target; (b) copper target; (c) lead target; (d) molybdenum target; (e) silver target; (f) cadmium target

All the previous considerations return again in the Figure 4.19. The signal distribution of monopixel cluster achieved with different target materials are here shown. The emission line which lie at high energy (i.e. cadmium and silver) are hardly detected making them useless for the ESAS calibration purposes.

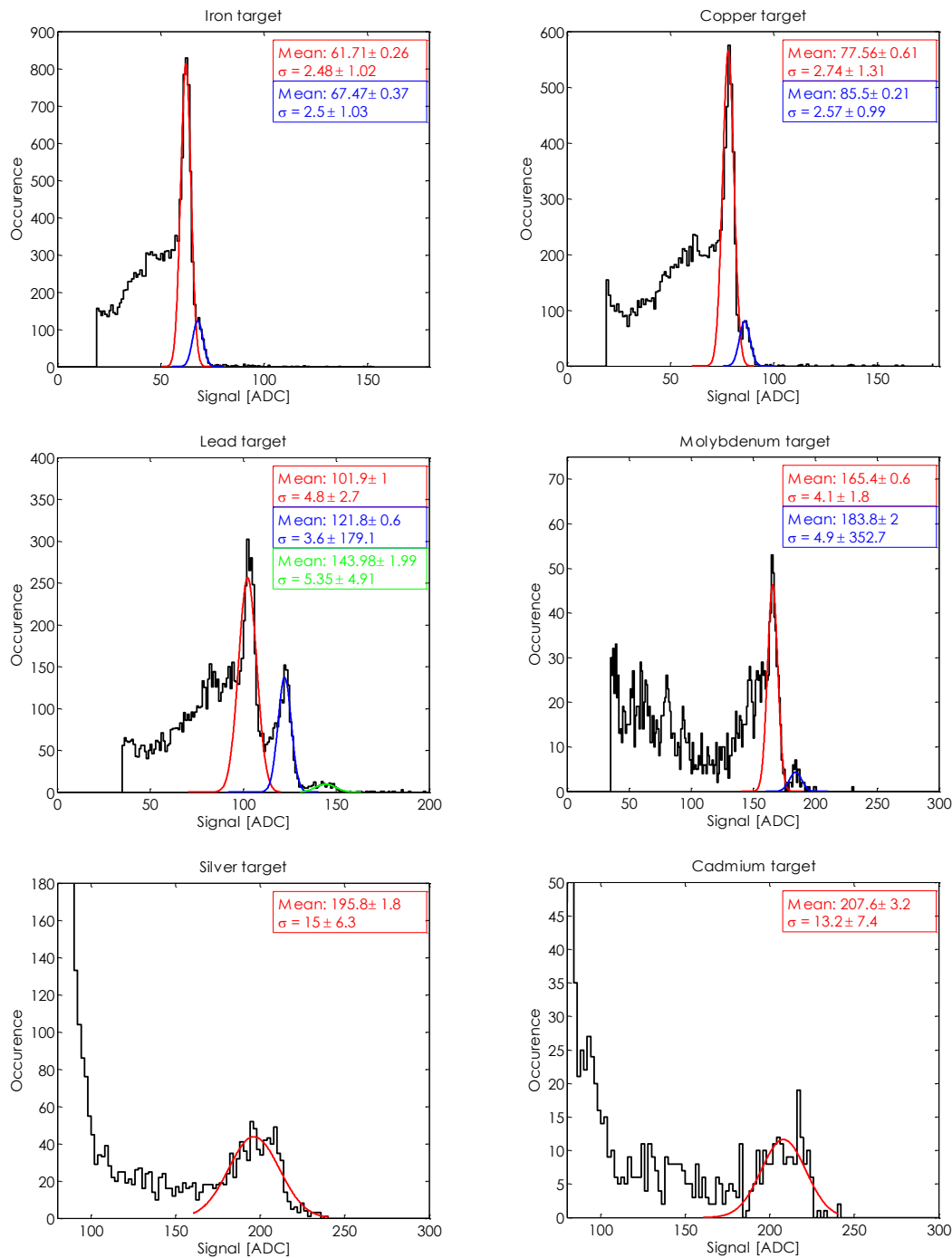


Figure 4.19 Signal distribution of the ESAS monopixel clusters due to the emission respectively of: (a) iron target; (b) copper target; (c) lead target; (d) molybdenum target; (e) silver target; (f) cadmium target

Finally it is possible to build the absolute calibration of the ESAS sensor. Only monopixel clusters have been selected to calculate the calibration line. Correlation plot between the photon energy and the mean value of the related monopixel cluster peak is drawn in Figure 4.20. The bar error corresponds to the standard deviation of the Gaussian fit on the monopixel cluster distribution. To achieve a more accurate fit, the error of every single measurement has been taken in account. At each point populating the Figure 4.20 has been assigned a weight inversely proportional to its measurement error.

A calibration value of 9.28 ± 0.31 ADC/keV can be found. Equivalently the calibration factor can be expressed as 29.93 ± 1 e/ADC.

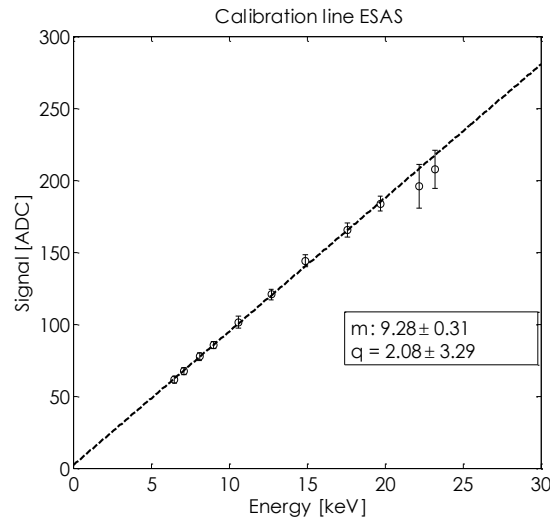


Figure 4.20 Correlation between photon energy and peak cluster signal with a linear fit

Using the calibration we can convert the pixel noise of the ESAS from ADC to electrons giving a values independent by the read-out electronic; in the most common working condition (32ms integration time) the noise becomes: 41.9 ± 7.7 e.

In this case it is difficult to give a precise value of the signal over noise ratio due to the presence of the incomplete charge collection region. If we consider only the peak related to the complete charge collection we are taking in account only a small amount of all the incoming photons and we are drastically reducing the detection efficiency.

However, the position of the peak sets the end point of the signal distribution and represents the maximum signal achievable by the detector. Under these assumptions the measured SNR for the ESAS matrix, when 5.9keV photons are completely absorbed, is 38.2 ± 1.77 while it rises up to 148.3 ± 13 for 23.3keV photons. In case of complete charge collection it is obvious that the monopixel cluster has a best SNR with respect to the case of cluster having more than one pixel.

Another important figure of merit carried out from these measurement is the energy resolution of the sensor, defined as the ration between full width at half maximum and the peak position. This parameter approaches an average value of 9.2 ± 2.8 % which in terms of eV it becomes 595eV for 6.5keV photons and 2.12keV for 23.2keV photons.

4.4.2 Sensor absolute calibration of the ESAL matrix

The same tests performed on the ESAS matrix have been repeated on the ESAL matrix.

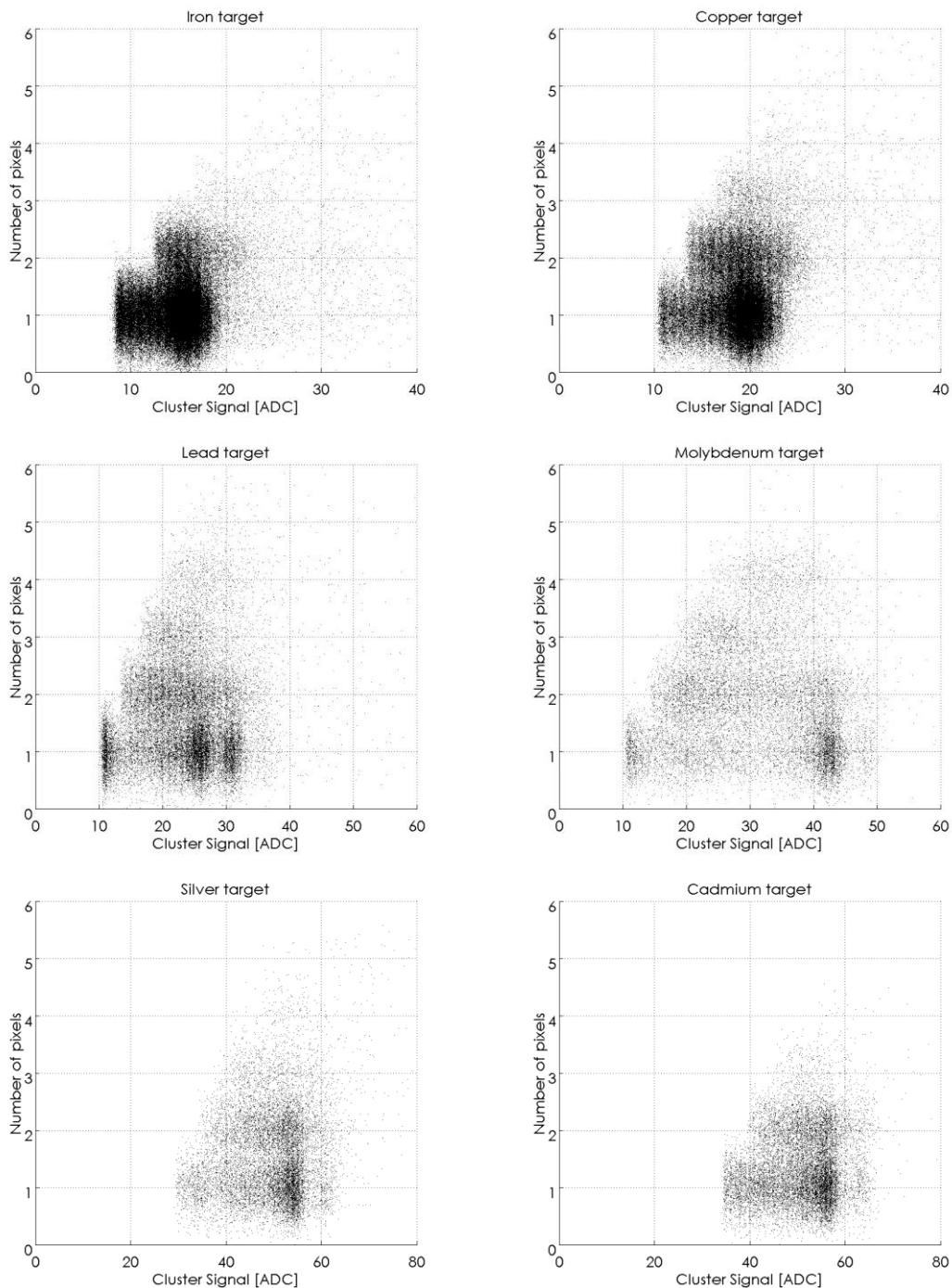


Figure 4.21 Correlation among cluster signal and number of pixels in the cluster due to the emission respectively of: (a) iron target; (b) copper target; (c) lead target; (d) molybdenum target; (e) silver target; (f) cadmium target

In Figure 4.21 is shown the correlation plots for the six targets employed in the fluorescence studies. The analysis have been performed considering a 3×3 pixels cluster with a threshold $T = 8$ ADC at least (about 10 times the single pixel noise σ) and a V_{ad} imposed at 3 ADC (about 3 times the single pixel noise σ). As expected, the signal detected by the ESAL pixels, featuring a large photodiode, is lower than the ESAS due to the unfavorable conversion factor charge-voltage which reduces the output voltage drop of the pixels.

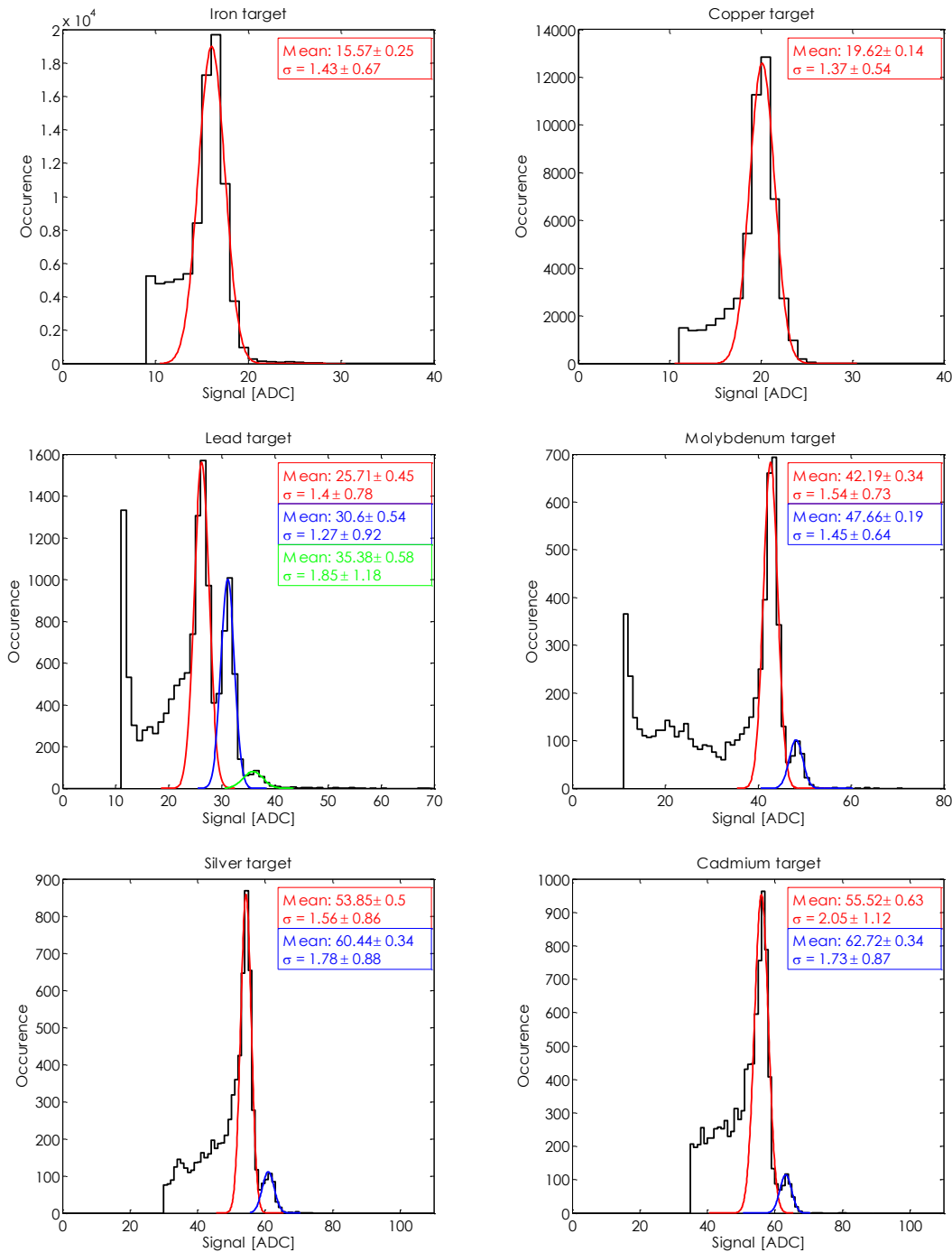


Figure 4.22 Signal distribution of the ESAL monopixel clusters due to the emission respectively of: (a) iron target; (b) copper target; (c) lead target; (d) molybdenum target; (e) silver target; (f) cadmium target

Also the charge sharing between adjacent pixels is more limited. The mean size of the cluster is 1.13 pixel for Iron target, 1.61 pixel for Lead target and 1.82 for Molybdenum target. Also the charge collected loss is reduced due to the larger n_{well} featuring by the ESAL pixel. The signal distribution for monopixel clusters are very defined. Even for energetic photons it is possible to recognize clear spectrums (see Figure 4.22), which was not possible for ESAS matrix.

Finally it is possible to build the absolute calibration also for the ESAL sensor. Always monopixel clusters have been selected to calculate the calibration line. Correlation plot between the photon energy and the mean value of the related monopixel cluster peak is drawn in Figure 4.23. The bar error corresponds to the

standard deviation of the Gaussian fit carried out by the monopixel cluster distribution. To achieve a more accurate fit, the error of each single measurement has been taken in account. In fact at every point populating the Figure 4.23 has been assigned a weight inversely proportional to its measurement error. A calibration value of 2.42 ± 0.04 ADC/keV can be found. Equivalently the calibration factor can express as 112 ± 1.85 e/ADC. The energy resolution approaches an average value of 4.4 ± 0.5 %.

Using the calibration we can convert the pixel noise of the ESAL from ADC to electrons giving a values independent by the read-out electronic; in the most common working condition (32 ms integration time) the noise turns out to be: 100 ± 35 e.

Under these assumptions the measured SNR for the ESAL matrix, when 5.9keV photons are completely absorbed, is 16 ± 5.6 while it rises up to 64 ± 22 for 23.3keV photons.

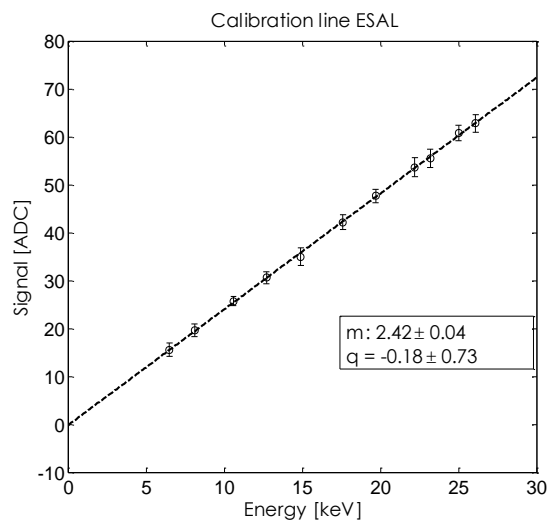


Figure 4.23 Correlation between photon energy and peak cluster signal with a linear fit

4.5 Charge particle response for ESAS and ESAL matrix

Measurements have been carried out with different setups and many different charged particle sources, but we are focusing on the behavior of the two matrices in case of irradiation with electrons with energy close to a MIP (i.e. the most difficult particle to detect). Firstly the SNR and the charge sharing among the pixels of the detectors will be analyzed. Then, using the absolute calibration, it will be given an estimation of the depth at which the different kind of photodiode are able to collect the charge generated by the radiation. The tests have been performed at Beam Test Facility (BTF) in Frascati, which is a beam line featuring electron or positron beams, with an energy in the range of 25MeV to 750MeV.

4.5.1 Behavior of the ESAS matrix exposed to high energy electron beam

The Figure 4.24 shows a typical response of the pixel of the ESAS to 465MeV electrons beam. The signal is not entirely confined into one pixel but there is a non negligible amount of charge collected by the pixels surrounding the central one.

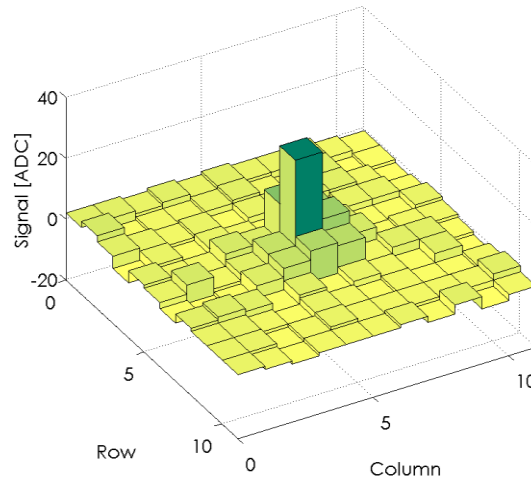


Figure 4.24 Typical response of an area of 11x11 pixels around a pixel crossed by an accelerated electron.

On average the signal is distributed as in Figure 4.25(a): the central pixel collects the 10.5% of the charge, the 3x3 pixels submatrix collect the 53.5%, the 5x5 collect the 78.2%, the 7x7 collect 91% and the 9x9 contains about the 97% of the charge.

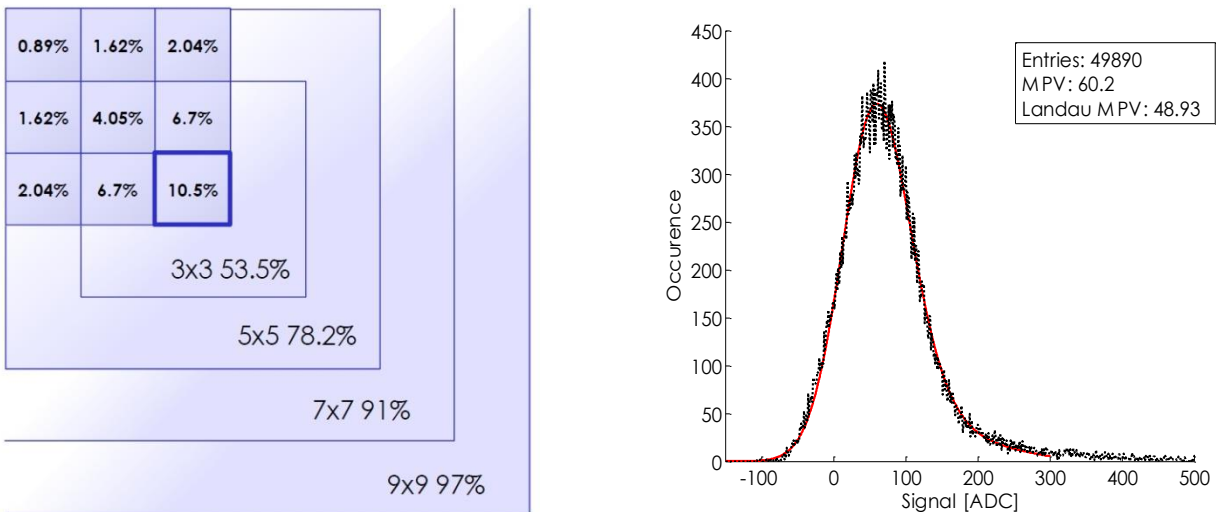


Figure 4.25 (a) Distribution of the collected charge around the impact point for the ESAS exposed to a 465MeV electrons. (b) Signal distribution of the 9x9 pixels cluster related to the matrix ESAS exposed to a 465MeV electrons.

Looking at the values of Figure 4.25(a) it is clear that if we want to measure the total amount of charge collected by the pixels we should use a large cluster in order to include all the electron-hole pairs generated. The Figure 4.25(b) shows the 9x9 pixels submatrix signal distribution with its fit according the expected signal distribution as in Eq. (2.19). The algorithm gives 48.94 ± 0.3 ADC as the MPV of the Landau distribution which is lower than the peak of the distribution (60.2 ADC). This is not surprising,

because the convolution between the Landau and the Gaussian distribution, representing the cluster noise and featuring a standard deviation 9 times greater than the pixel noise, will move the peak of the convoluted distribution at higher values. Knowing the conversion factor e/ADC , retrieved from the x-ray calibration, we can translate the MPV to the equivalent electron hole pair, which reads: $1464 \pm 58 e$. From the theory $1464e$ corresponds to a collecting length of about $22 \pm 1 \mu m$. However this thickness should not be simply considered as the collection depth of the chip beyond which the photodiode is no longer able to collect. Actually, the ability to collect charge as a function of the depth has a more complex shape with a maximum near the junction and a long tail for deeper positions; it can be only asserted that this kind of sensors, from the point of view of the ability to collect the charge, can be compared to an ideal (i.e. fully depleted) detector which is able to collect all the charge deposited within this thickness. The best SNR in the MIP detection can be achieved for 3×3 pixels cluster and the value which turns out is of 17.6 ± 3.2 .

4.5.2 Behavior of the ESAL matrix exposed to high energy electrons beam

The behavior of the ESAL is slightly different with respect to the ESAS: in the Figure 4.26(a) has been drawn how the charge is divided among the adjacent pixels. As expected, because of the larger photodiode, the electronic charge sharing is lower. The 19.7% of the charge is collected by the central pixel and the cluster 3×3 contains about the 60.8% instead of the 53.5% as for the ESAS.

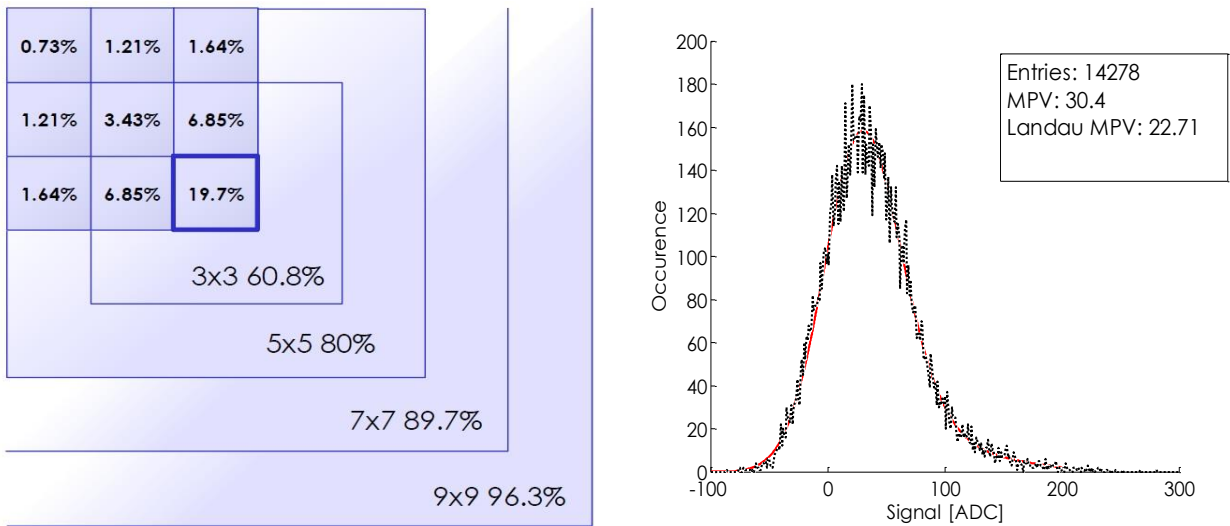


Figure 4.26 (a) Distribution of the collected charge around the impact point for the ESAL exposed to a 465MeV electrons.
 (b) Signal distribution of the 11×11 pixels cluster related to the matrix ESAL exposed to a 465MeV electrons;

Even if the bigger photodiodes collect more charge compared with smaller ones the conversion factor voltage/charge is unfavorable and as result the measured signal is lower. The Figure 4.26(b) shows the signal distribution of the 9×9 pixels submatrix and its fit according the Eq. (2.19). As can be seen the peak is located at lower value than the ESAS (30.4 ADC instead of 60.2 ADC) and the estimated MPV of the Landau is at 22.71 ± 0.4 ADC. In terms of electrons we have: $2543 \pm 44 e$.

Following the same procedure shown above about the equivalent thickness, we found a value of $38 \pm 7 \mu\text{m}$. This could potentially indicate that the ability to collect the deeper charge seems to be better for the larger photodiode. Also in this case the 3x3 pixels cluster has the best performance in term of the signal over noise ratio. The SNR for the 3x3 cluster is 14.7 ± 4.9 , which is slightly lower than the ESAS.

4.6 Spatial resolution and detection efficiency

In order to reconstruct a ionizing particle trajectory it is needed to detect exactly the positions of this particles with a probability as close as possible to 100%. The technique used to track the particle motion consists on the interposition along the trajectory of several sensors planes; from the position measurement in each plane the trajectories followed by the particles can be reconstructed. In these environments two of the most important parameters to be extracted are: the spatial resolution and the detection efficiency. The former is the resolution with which we can reconstruct the crossing point of the particle and the latter is the probability to reveal the passage of the particle when it effectively crosses the sensor.

Basically, the evaluation of the spatial resolution of a particle sensor consists on the measurement of the differences between the estimated impact position and the real one. Similarly, the detection efficiency consists in the ratio between the estimated number of particles crossing the sensor and the real one. A solution of these problems comes from the use of a tracking system (usually called *telescope*) able to predict the number and the impact position of the incoming particles. In our dedicated setup the telescope is composed exclusively from RAPS03 sensors. The Figure 4.27 illustrates schematically this system. For simplicity considering a one-dimensional system we must use at least three sensors to detect the coordinate x_1, x_2 and x_3 of the particle trajectory at three different position d_1, d_2 and d_3 . From the interpolation of two of these points we can reconstruct the particle path and use it to estimate the position on the third sensor. From simple geometry considerations, if a and b indicate the two sensors used to estimate the position on the third one, that is c , such predicted position will be:

$$\hat{x}_c = \frac{x_b - x_a}{d_b - d_a} d_c + \hat{x}_a \quad (4.3)$$

and the difference whit the measured one (in the following called residue also) mathematically is:

$$e = x_c - \hat{x}_c = x_c - \frac{x_b - x_a}{d_b - d_a} d_c - \hat{x}_a \quad (4.4)$$

If we assume that the uncertainty in the position measurement has a Gaussian probability density function whit a standard deviation σ , e has a Gaussian probability density function in turn with a deviation of:

$$\sigma_e = \sigma \sqrt{2(k^2 - |k| + 1)} \quad (4.5)$$

$$k = \frac{d_c}{(d_b - d_a)}$$

So, from the standard deviation of e and knowing the geometry of the system it is possible to retrieve σ which is the spatial resolution of the sensors.

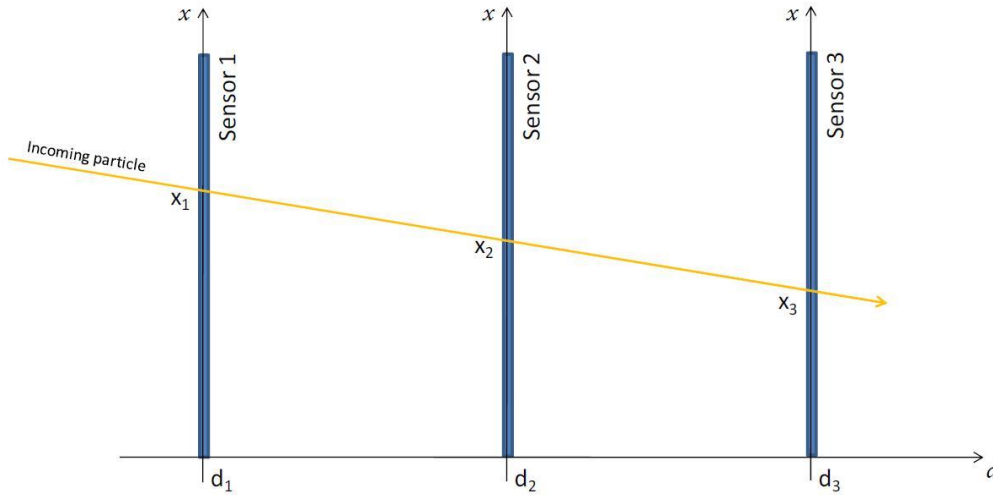


Figure 4.27 Illustration of a tracking system with three sensors aligned one in front of each other.

The previous example however represents an ideal case; in real cases there are several sources of uncertainty. First each sensor has a non negligible thickness which produces a deflection of the incoming particle due to the phenomenon of multiple scattering, which adds another aleatory contribution to the coordinates of the measured position. The effect on the residues is to enlarge its distribution.

Other sources of uncertainty come from a non perfect alignment of the different elements. Each sensor, as a solid body, has six different degree of freedom, namely three translations and three rotations. The two translations perpendicular to the particles direction adds an offset to the coordinates of the impact point. The effect on the distribution of the residue is only a shift of the Gaussian peak. The translation along the particle direction adds an uncertainty to the coordinate d ; however if the distance of a sensor to another is big compared to the position uncertainty this component can be neglected.

The rotations (Figure 4.28) are more difficult to compensate. Referring to the Figure 4.29 a rotation around the x or y axis has the effect shown in Figure 4.29(a), mathematically:

$$x_2 = x_1 \frac{1}{\cos(\Theta_y)}; y_2 = y_1 \frac{1}{\cos(\Theta_x)}; \quad (4.6)$$

if the angles are little (few degrees) the correction can be neglected. For the Θ_d tilt the situation is more complex because each coordinate x or y of a sensor is related to both the coordinates of another sensor (see Figure 4.29(b)).

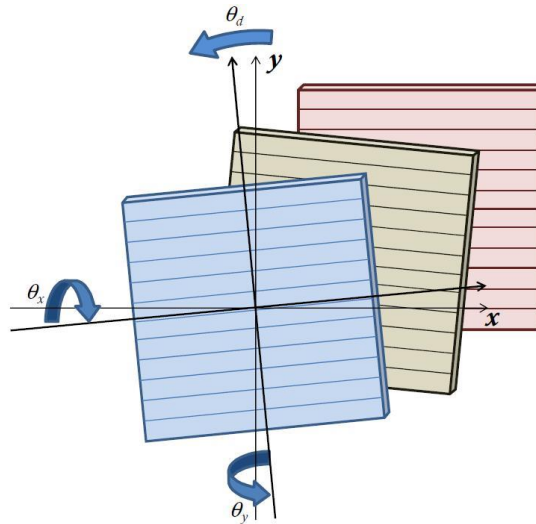


Figure 4.28 The three tilt angles among the sensors.

Mathematically the tilt around the axis parallel to the particles beam direction can be modeled as:

$$\begin{vmatrix} x_2 \\ y_2 \end{vmatrix} = \begin{vmatrix} \cos(\Theta_d) & -\sin(\Theta_d) \\ \sin(\Theta_d) & \cos(\Theta_d) \end{vmatrix} \cdot \begin{vmatrix} x_1 \\ y_1 \end{vmatrix} \tag{4.7}$$

The effect of all the rotations on the residue is to widen its distribution, but from the analysis of the coordinate x_2 and y_2 detected on a sensor as a function of the coordinate x_1 and y_1 detected to another sensor the tilt can be estimated and corrected.

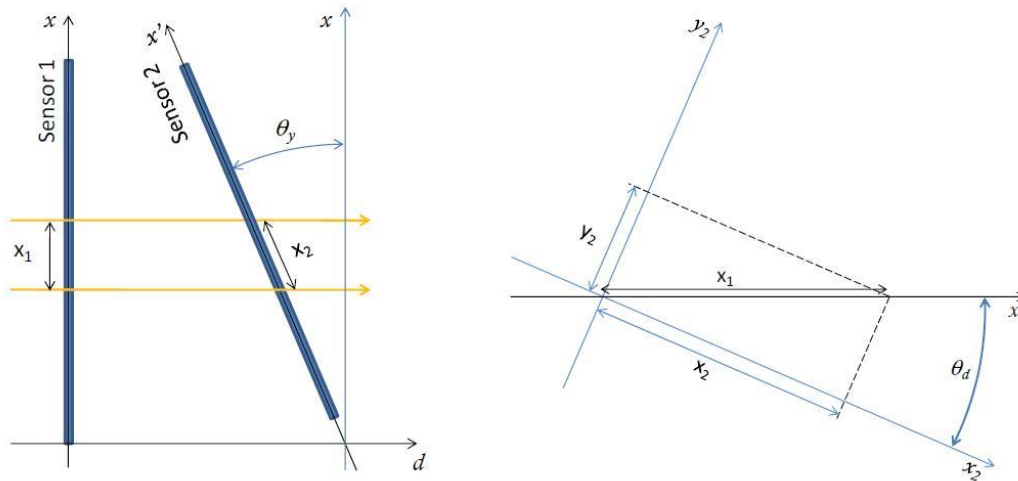


Figure 4.29 Effect of a non parallelism among two different sensors.

Summarizing the relation among two different sensors we can consider:

$$\begin{vmatrix} x_2 \\ y_2 \end{vmatrix} = \begin{vmatrix} m_{xx} & m_{xy} \\ m_{yx} & m_{yy} \end{vmatrix} \cdot \begin{vmatrix} x_1 \\ y_1 \end{vmatrix} + \begin{vmatrix} q_x \\ q_y \end{vmatrix} \tag{4.8}$$

From the measured points, using a multiple linear regression algorithm, it is possible to retrieve the coefficients m and q .

Another source of uncertainty comes from the algorithm used to define the crossing point of the particles with each single detector. To improve the resolution in the position reconstruction, it is possible to exploit the charge sharing effect among adjacent pixels. Usually the barycentre algorithm is used (in the following called Center of Gravity (COG)). Mainly, due to the finite nature of the detector and the dimensions of the cluster, the COG can add a systematic error also (for a detailed discussion of the problem see [4.10] [4.11] [4.12]).

4.6.1 Beam test setup

To reduce the contribution of the multiple scattering it is necessary to use particles with a very high momentum, being the scattering inversely proportional to the momentum [4.13]. For this reason the accessibility to an irradiation facilities with high energetic particles beam is fundamental for this kind of measurements. We have tested our sensors using a 180GeV positrons and protons beam provided at the SuperProtoSynchrotron (SPS), situated at CERN.

A simulation with GEANT4 [4.14] of the detector system has been carried out to evaluate the multiple scattering contribution. In Figure 4.30 there is a drawing of the simulation: three identical detectors composed by 300 μm of silicon and 1mm of Al_2O_3 are equally spaced by 2cm of air; the yellow line represent the protons beam while the other azure lines are secondary emissions. The multiple scattering retrieved by the simulation is 0.1 μm using the *acb* configuration, and 0.2 μm in the *abc* configuration. This result shows how, at this energy, the multiple scattering contribution cannot affects the estimation of the spatial resolution of our sensors.

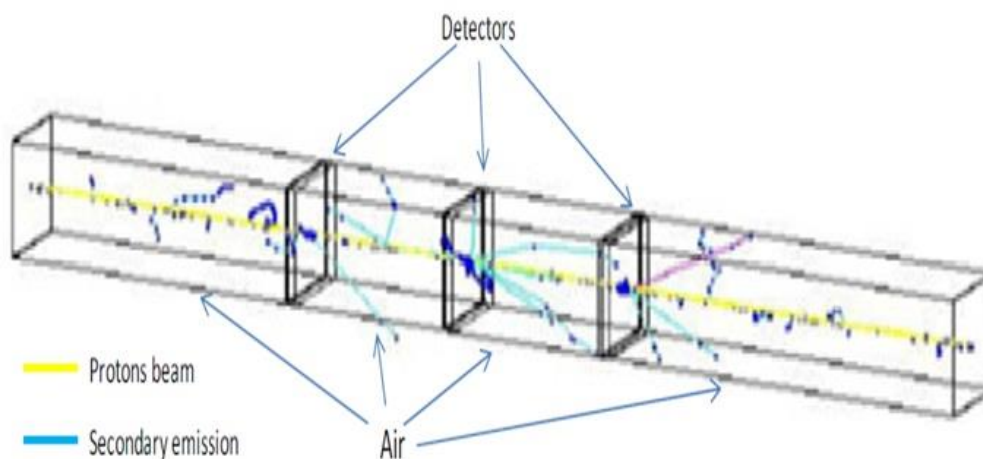


Figure 4.30 A drawing of the system simulated with GEANT4 in order to evaluate the multiple scattering introduced by the detectors.

The Figure 4.31 shows the mechanical setup built up for the tests at CERN. Four RAPS03 sensors have been aligned one in front of each other. The RAPS03 are equally spaced by 20mm and aligned along the particles beam. The data are collected and synchronously stored for all the four sensors if simultaneously a single pixel signal of the first and of the last sensor of the telescope is bigger than a predefined threshold and if an external trigger signal indicates the presence of the particle beam.

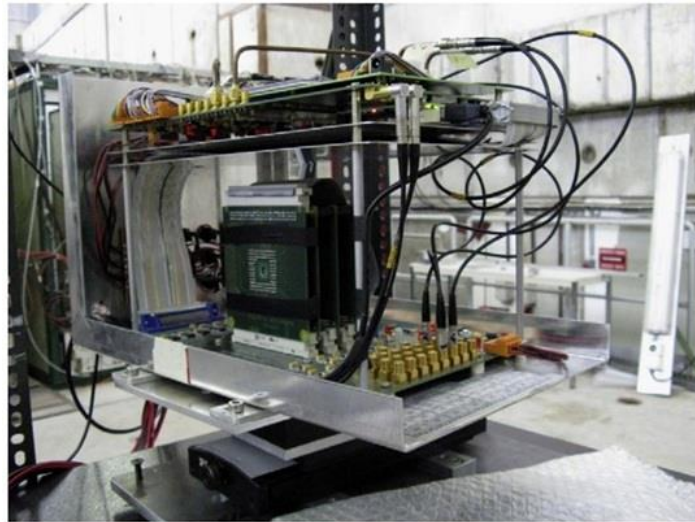


Figure 4.31 Sensors under tests at CERN Super-Proto-Synchrotron SPS irradiation facilities.

4.6.2 Spatial resolution measurement

After correction for misalignment of the various sensors (offsets and rotations) the distributions of the residuals between the telescope predictions and the measured hits on the detector under test could be derived.

In Figure 4.32 the residue distributions, scaled of the geometrical factor according Eq. (4.5), in both spatial directions perpendicular to the incident beam are illustrated respectively for the ESAS and ESAL sensors. The standard deviations of these distributions represent the spatial resolution of the sensors along the x-direction and y-direction. As can be seen there is a clear peak in each distributions standing out from a large background which is given by all the uncorrelated events; in red it is plotted the Gaussian fit.

The width of the residual distribution represents the intrinsic spatial resolution of our detector after misalignment corrections, which is $1.38\mu\text{m}$ for x-direction and $1.51\mu\text{m}$ for y-direction (ESAS) and $2.01\mu\text{m}$ for x-direction and $2.18\mu\text{m}$ for y-direction (ESAL). These are good values comparable with the performances of other solid state detector (see for example [4.15]).

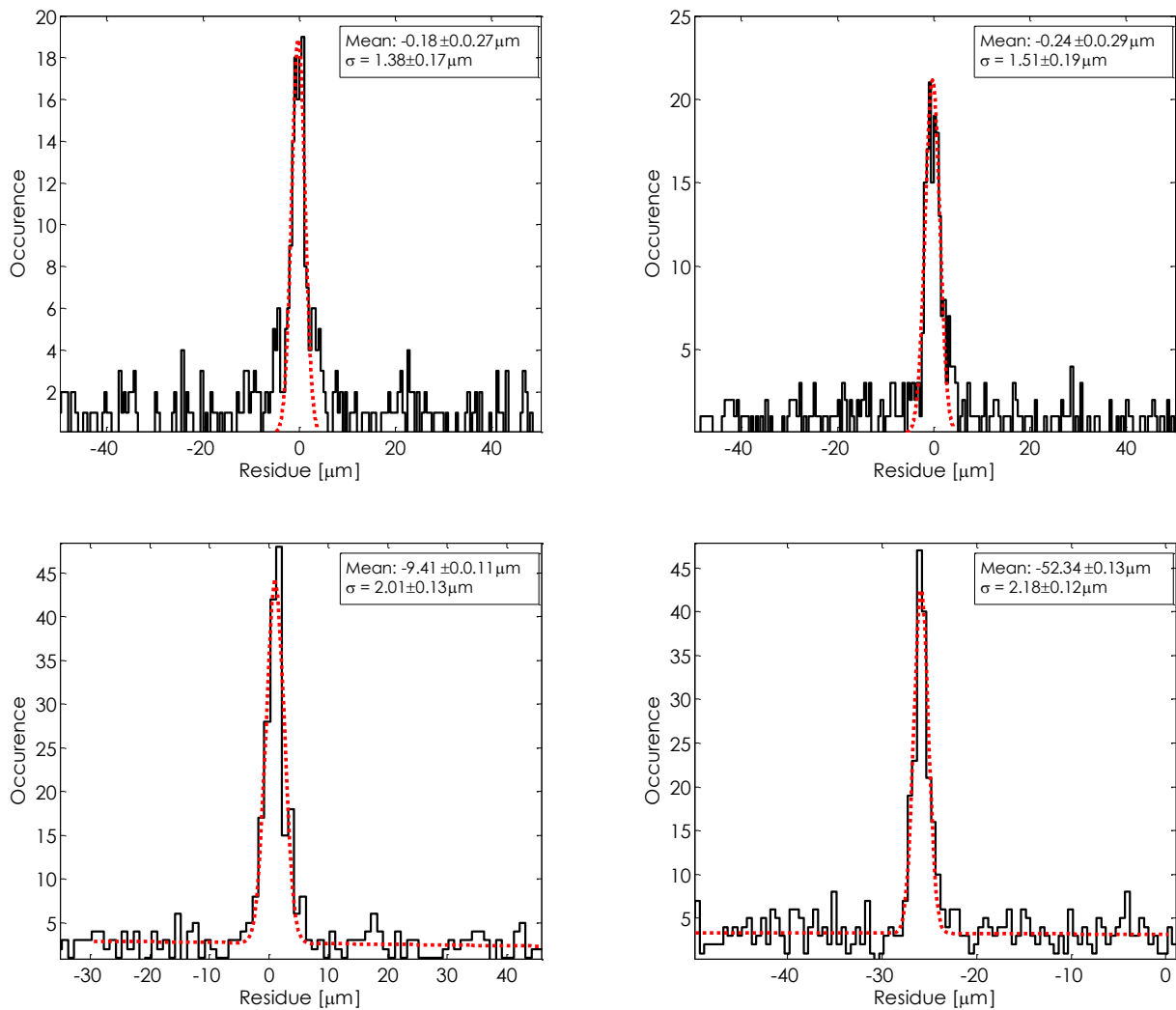


Figure 4.32 Distribution of the residues, scaled of the geometrical factor, on the third sensor using the second and the fourth one as predictors; on the top ESAS distributions along x and y direction, on the bottom ESAL distributions along x and y direction.

4.6.3 Detection efficiency measurement

Both pixel layouts have been characterized in terms of detection efficiency and fake rate. In Figure 4.33 the detection efficiency versus fake probability curves are reported. Due to the sensor misalignments was not possible the direct measurement of the detection efficiency. In fact the curves in Figure 4.33 have been derived from the analysis of the SNR and from the information concerning the charge sharing in a 3x3 pixels submatrix.

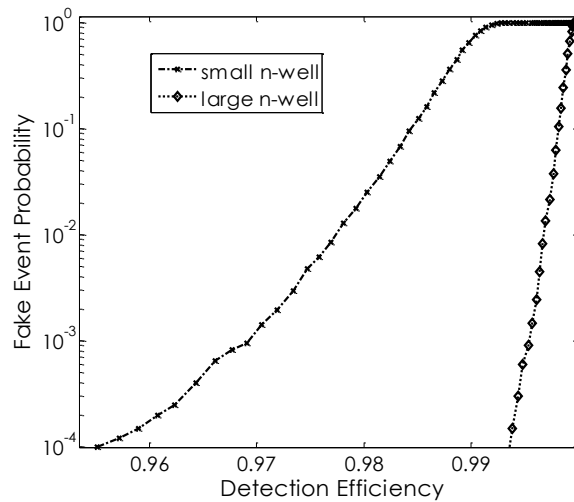


Figure 4.33 Detection efficiency vs fake rate probability for both the small photodiode (cross-dotted line) and the large photodiode (open diamond).

The open diamonds and the crosses in Figure 4.33 correspond to threshold values of the cluster seed normalized to single pixel noise. For a fake probability of 0.01% the efficiency is 99.3% for the large photodiode and 95.5% for the small photodiode. Due to the reduced charge sharing between the seed and its adjacent pixels, the large photodiode solution is preferred, allowing a greater signal/noise rejection.

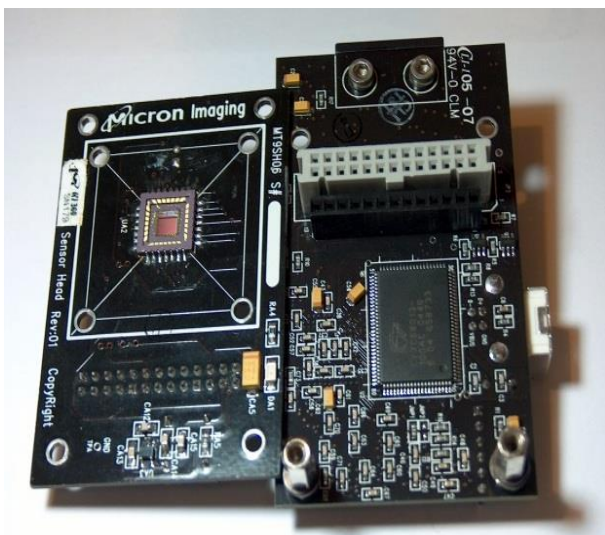
References

- 4.1 D. Passeri et al., *Detectors with reconfigurable read-out electronics in a 0.18 μ m CMOS bulk technology*, Nuclear Science Symposium Conference Record, vol. 4, pp. 2509-2512, 2007.
- 4.2 D. Passeri, et al., *Active Pixel Sensor Architectures in Standard CMOS Technology for Charged-Particles Detection*, PIXEL 2002, Carmel, California, USA, September 9–12, 2002
- 4.3 Paolo Delfanti, Ph.D. Thesis, *Progetto e collaudo di un sensore di radiazione a stato solido*, Università degli Studi di Parma, 2008.
- 4.4 Analog Devices, AD9238 Data Sheets
- 4.5 Opal Kelly, XEM3050 User manual
- 4.6 Solid Work corp. [Online]. <http://www.solidworks.it/>
- 4.7 Opal Kelly, Front Panel 3 User Manual.
- 4.8 National Instrument. LabVIEW. [Online]. <http://www.ni.com/labview/>
- 4.9 H. Tian, B. Fowler, and A. El Gamal, *Analysis of Temporal Noise in CMOS Photodiode Active Pixel Sensor*, IEEE Journal of Solid-State Circuits, vol. 36, no. 1, pp. 92-101, 2001
- 4.10 G. Landi, *Properties of the center of gravity as an algorithm for position measurements*, Nuclear Instruments and Methods in Physics Research, vol. A 485, pp. 698-719, 2002.
- 4.11 Landi G., *Properties of the center of gravity as an algorithm for position measurements: two-dimensional geometry*, Nuclear Instruments and Methods in Physics Research, vol. A 497, pp. 511-534, 2003.
- 4.12 C. Amsler et al., *A high resolution silicon beam telescope*, Nuclear Instruments and Methods in Physics Research, vol. A 480, pp. 501-507, 2002.
- 4.13 Particle Data Group PDG, *Passage of particle through matter*, Nuclear and Particle Physics, vol. 33, no. 27, pp. 258-270, July 2006.
- 4.14 Geant4. [Online]. <http://geant4.web.cern.ch/geant4/>
- 4.15 Yasuhiro Sugimoto. ACFA joint Linear Collider Physics and Detector Working Group. [Online]. <http://www-jlc.kek.jp/subg/vtx/index-e.html>

Chapter 5.

Commercial CMOS Active Pixel Sensor

In recent years, CMOS pixel imagers applications have grown at a phenomenal rate. Consumers are demanding more functionality, including advanced and robust imaging capabilities on DSCs and camera phones, as well as a growing emphasis on the number of pixels present on the same surface (several Megapixels devices are now normally available). The integration at sensors level of these features has been possible thanks to the progress of the microelectronics fabrication technology: today, a pixel size of less than $2\mu\text{m}$ is available. Beside imaging applications, new perspectives in several research areas could be opened by such a class of devices. As an example, position measuring devices for ionizing radiation with sub-micrometer intrinsic accuracy could be possible.



Parameter		Typical Value
Optical Format		1/4-inch (4:3)
Active Imager Size		3.58mm(H) x 2.69mm(V), 4.48mm Diagonal
Active Pixels		640H x 480V
Pixel Size		5.6 μm x 5.6 μm
Color Filter Array		RGB Bayer Pattern
Shutter Type		Electronic Rolling Shutter (ERS)
Maximum Data Rate/ Master Clock		13.5 MPS/27 MHz
Frame Rate	VGA (640 x 480)	30 fps at 27 MHz
	CIF (352 x 288)	Programmable up to 60 fps
	QVGA (320 x 240)	Programmable up to 90 fps
ADC Resolution		10-bit, on-chip
Responsivity		1.9 V/lux-sec (550nm)
Dynamic Range		60dB
SNR _{MAX}		45dB
Supply Voltage		2.8V \pm 0.25V
Power Consumption		70mW at 2.8V, 27 MHz, 30 fps
Operating Temperature		-20°C to +60°C
Packaging		28-Pin PLCC

Figure 5.1 (a) MTV9V011 sensor with evaluation board and Demo2 DAQ board (b) Summary of the Micron MT9V011 characteristics.

In this chapter, we have investigated the possibility of using MICRON (now Aptina Imaging) CMOS imagers as ionizing radiation detectors, either for soft x-ray than for charged particles. A standard sensors featuring $5.6 \times 5.6 \mu\text{m}^2$ pixel size and 640×480 pixels with epitaxial layer [5.1] has been extensively tested. These devices have a built-in 10bit ADC conversion capability and also the possibility to adjust the gain of the circuit from 1.00 up to 15.88 [5.2]. The integration time of the device may also be varied from $56\mu\text{s}$ to 267ms, with a default value of 33.3ms. The read-out of the sensor is assured (Figure 5.1(a)) by the Demo2

board and the MT9SH06 evaluation board, with an USB line to power the system, to control the sensor and to receive the data. The sensor under test have no microlenses over the pixels and is run in monochromatic mode to equalize the pixel response. In Figure 5.1(b) there is a summary of its characteristic from Micron datasheet [5.3]. The acquisition setup is supplied with its driver and a software, named DevWare, which allows to read and display the data acquired by the sensor and to explore all the possible sensor settings. However this software was not suitable for our purposes and a dedicated software has been developed using the DLL library provided with the DevWare software package [5.4].

5.1 Noise analysis of Micron MT9V011

The sensor has been characterized in absence of external stimuli.; for each pixel the signal distribution has a Gaussian shape from which the average (pedestal) and its RMS (noise) have been extracted to be used later. The sensor is featuring 307200 pixels (VGA 640x480 format), and its homogeneity has been checked: in Figure 5.2(a) it is reported the distribution of all the pedestals of a sensor and the shape is again Gaussian to a good approximation with a small standard deviation, while in Figure 5.2(b) the distribution of the pixel noise is shown for all the pixels in the sensor. The shape is fairly Gaussian with some tails toward higher noise, again showing a good behavior.

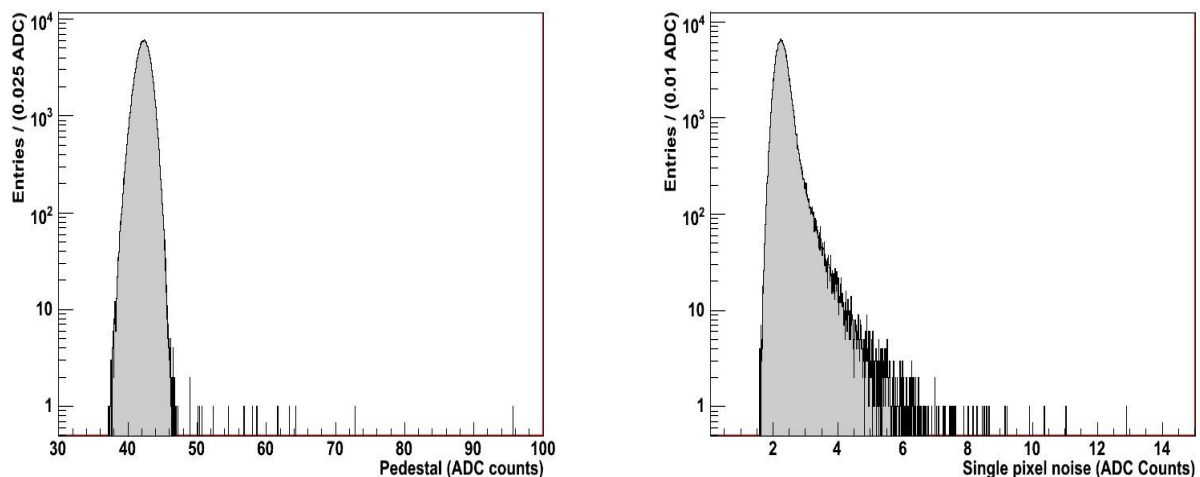


Figure 5.2 Sensor uniformity: (a) single pixel pedestal distribution for all pixels. (b) Single pixel noise distribution for all pixels.

After pedestal subtraction it may remain a collective variation in time of the pixel signal that should be evaluated. The distribution of the average value of all the pedestal subtracted pixel signals for each frame (Figure 5.3(a)) shows that indeed any such residual effect is well below the pixel noise value, hence can be neglected in our setup.

Another important value to be extracted is the single pixel threshold level, in order to avoid fake events when stimuli are applied. In Figure 5.3(b) the pixel occupancy, defined as the probability of a single pixel to be over a certain threshold, has been plotted. The threshold level has been normalized to the single pixel noise and the curves for two different values of the sensor integration time (56 μ s and 100ms) are shown.

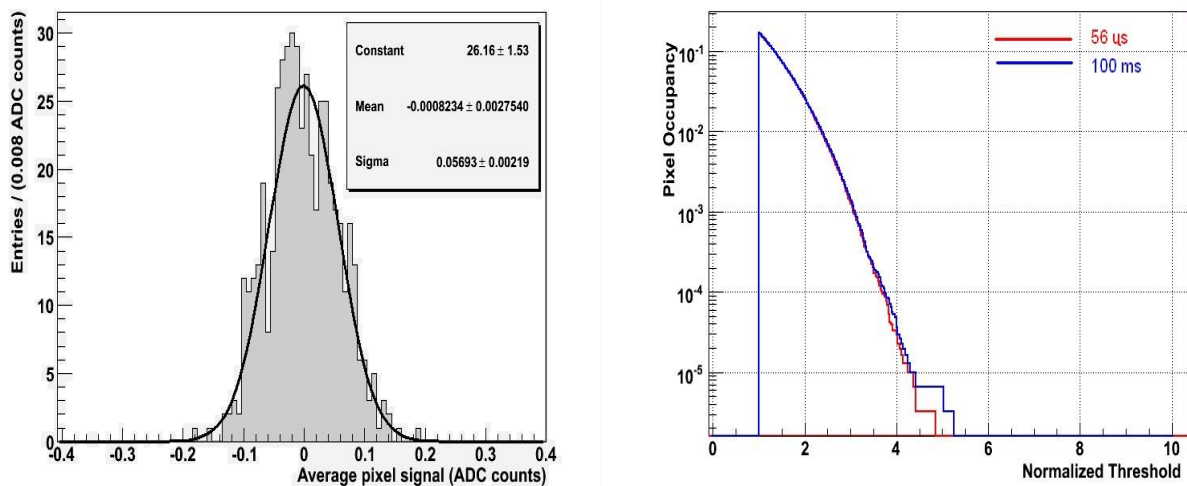


Figure 5.3 (a) Distribution of average pixel signal showing that for all events the common fluctuation is below few ADC counts. (b) Pixel occupancy for two different integration times, 56ms (red) and 100ms (blue), as a function of the pixel threshold normalized to the single pixel noise.

No relevant variation is visible and the endpoint of the distribution is situated near 5.0, irrespective of the value of the integration time. To reach a 3×10^{-5} occupancy (i.e. less than one pixel per frame) a normalized threshold value bigger than 6 is needed. This would translate, at the default integration time (33.3ms) into an absolute cut of about 20 ADC counts for maximum gain.

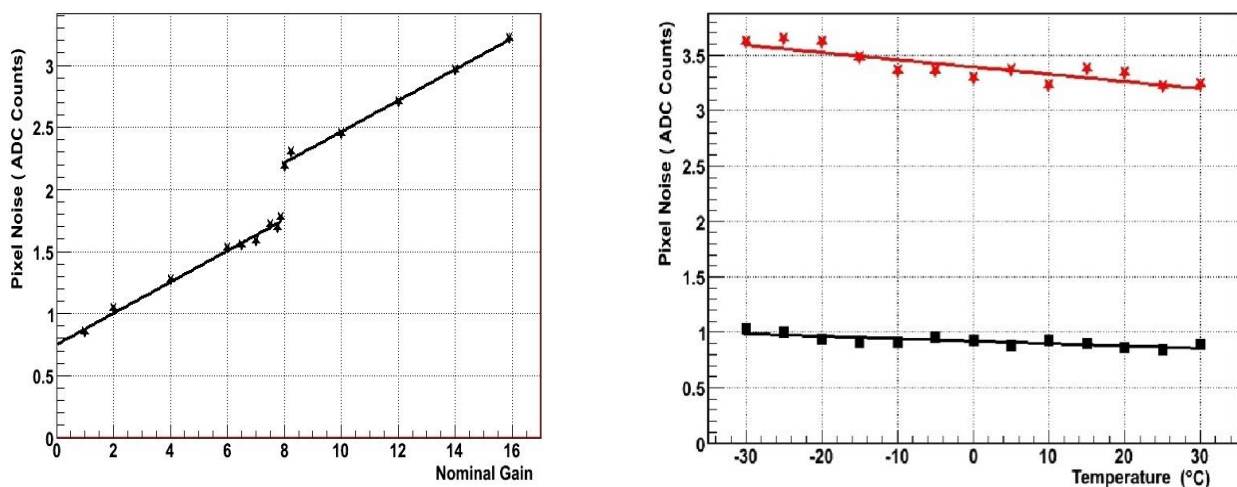


Figure 5.4 Variation of pixel noise: (a) as a function of nominal gain; (b) as a function of temperature for maximum (red stars) and minimum gain (black squares) configuration.

The linearity of the sensor adjustable gain has been verified against the pixel noise value. In Figure 5.4(a) it is shown the distribution of the pixel noise for a single pixel as a function of the nominal gain. It can be seen that the gain interval is divided in two domains at the nominal value of 8; in each one a good linearity is achieved, with the same slope, being different just by a constant term of 0.4 ADC counts due to a different circuit settings.

The behavior of the detector has been checked against temperature variation because in several applications, especially when radiation damage is involved, the required operating temperature is below 0°C . The sensor is certified to be working in an interval from -20°C up to $+60^{\circ}\text{C}$. A scan from -30°C to

+30°C has been performed looking at the variation of the single pixel noise. The results are shown in Figure 5.4(b): at minimum gain ($G=1.0$) there is almost no dependence (fractions of ADC counts over the whole range). Subtracting the quantization error at minimum gain (triangles), the resulting dependence is more evident but still negligible. At maximum gain ($G=15.88$) a weak dependence could be measured, $-0.0063 \text{ ADC}/^\circ\text{C}$ corresponding to a 10% variation in the pixel noise [5.5].

5.2 Sensor characterization with calibrated x-ray sources

The sensor has been stimulated with several photon sources from few keV (^{55}Fe for 5.9 and 6.4 keV) to several tens of keV (x-ray tube with monochromator for 8, 16, 24 and 32 keV), to study its response and to build the absolute calibration relation. The frames are continuously acquired by the DAQ and recorded for offline analysis if at least one pixel signal (seed) is over a threshold bigger than 6 times the pixel noise (autotrigger mode). The response to a single ^{55}Fe photon is well confined within few pixels (Figure 5.5(a)); the signal sharing is caused by the diffusion of the electron-hole pairs and the induced signal among adjacent pixels. To estimate the amount of signal-sharing among adjacent pixels, for each frame the sum of the signals of the 7×7 submatrix centered on the seed pixel is computed and it is used to normalize the signal of each pixel of the submatrix.

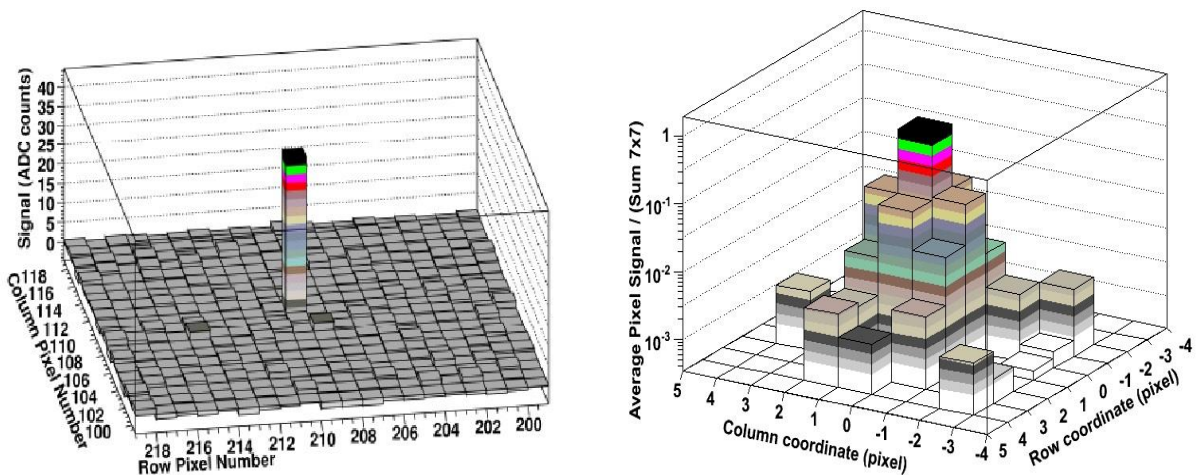


Figure 5.5 (a) Event display for a ^{55}Fe photon at minimum gain. (b) Distribution of average pixel signal in the 7×7 submatrix centered in the pixel with maximum signal; the signal of each pixel is normalized to the sum of the signals of the 7×7 submatrix.

In Figure 5.5(b) is shown the distribution of the average fraction for the 7×7 submatrix; most of the signal is concentrated into the seed pixel (67%) while the rest is mainly divided among the 8 adjacent pixels: 25% in the 4 with a border in common and 5% in the 4 with a corner in common.

To collect the signal caused by the photon it is customary to use the sum of all the pixels of a submatrix centered around the seed pixel, and the previous result suggests that for ^{55}Fe photons, it is enough to consider only the 3×3 submatrix to obtain most of the released charge. In Figure 5.6(a) is shown the distribution of the collected signal when the size of the submatrix is varied from 1×1 (just the seed pixel)

to 7x7. It can be seen that considering only the seed pixel will not reproduce a Gaussian distribution for the signal because there are many events where the charge is shared with the adjacent ones or only partially collected. The 3x3 submatrix assures the best efficiency in reconstructing the signal with the smallest width. Increasing the submatrix size will just widen the distribution, according to the square root of the number of pixel used without increasing the collected signal, as would be expected. It should also be noticed that the seed pixel has a Gaussian peak at a value higher than all the other options; this aspect, important for absolute calibration, will be investigated further.

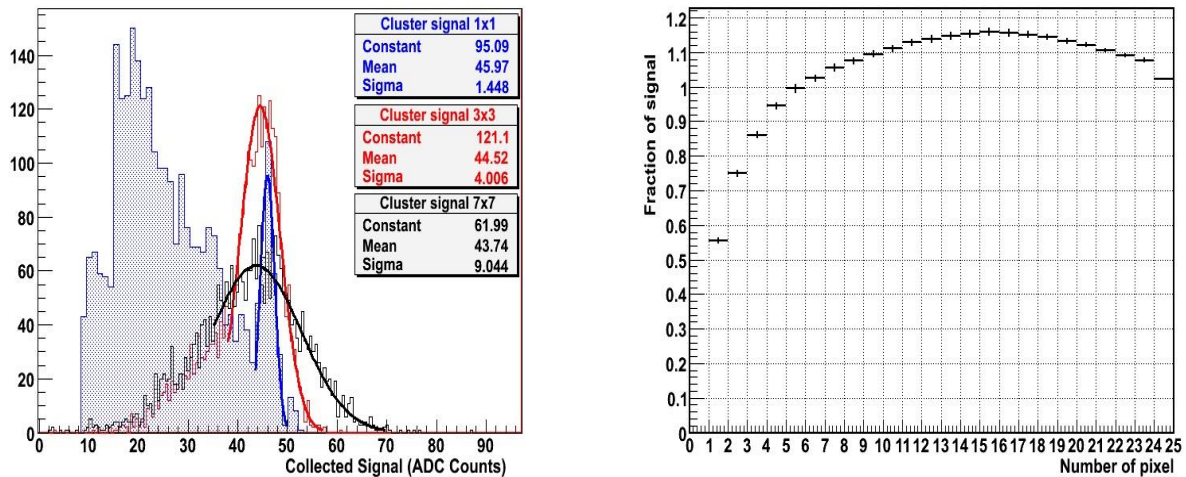


Figure 5.6 (a) Distribution of signal collected in a submatrix of size varying from 1 to 7 pixels at minimum gain.
 (b) Distribution of average fraction of pixel signal as a function of the number of pixel, ordered according to decreasing pixel signal value, summed up in the 5x5 submatrix.

Ordering the signals of the pixels in the 5x5 submatrix by decreasing values, the average fraction, with respect to the signal collected by the 5x5 submatrix, has been plotted (Figure 5.6(b)) as a function of the number of pixels summed up. To reach the 100% level it is enough to sum the 5 most important pixels being almost zero the average sum of the other 20 pixels; hence the idea of using a clustering algorithm for signal extraction. Figure 5.7(a) shows the distribution of the number of pixels belonging to a cluster when a ^{55}Fe source is used with the $V_{ad} = 3.0$. The average number is 5.7 and no cluster has more than 10 pixels; this confirms a good geometrical confinement of the signal in an area of few pixels, an area of the order of $100\text{-}200\mu\text{m}^2$. Comparing the distribution of the cluster signal (Figure 5.7(b)) with the one from the signal in the seed pixel and the one obtained summing up all the contributions in the 3x3 submatrix, we see that there is not a real difference between the two methods; although the difference with respect to the peak in the seed signal distribution remains.

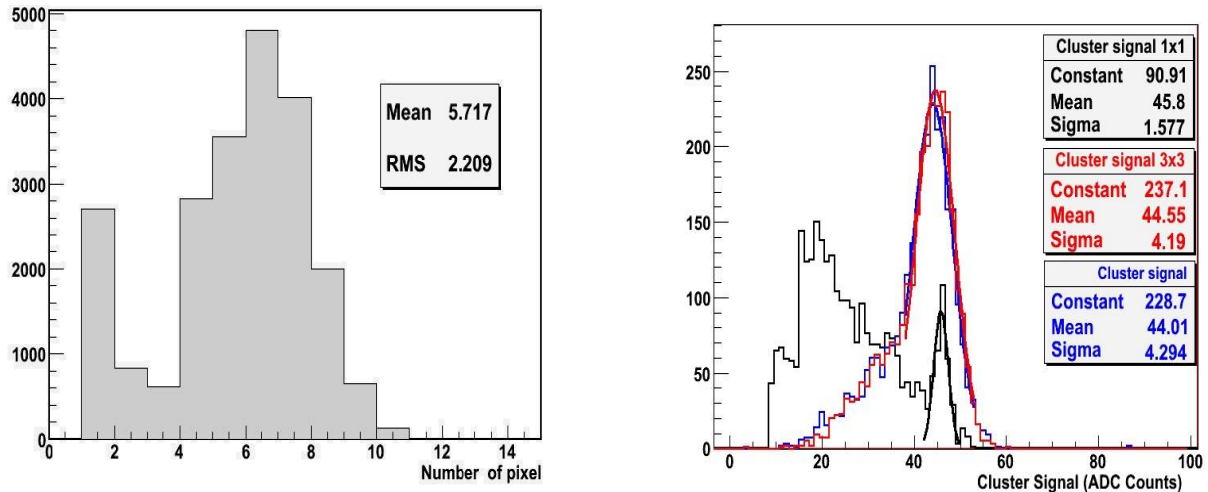


Figure 5.7 (a) Distribution of the number of pixels belonging to a cluster in the case of a ^{55}Fe photon. (b) Comparison between signal distribution for cluster algorithm (red), seed pixel (black) and sum over 3x3 submatrix (blue).

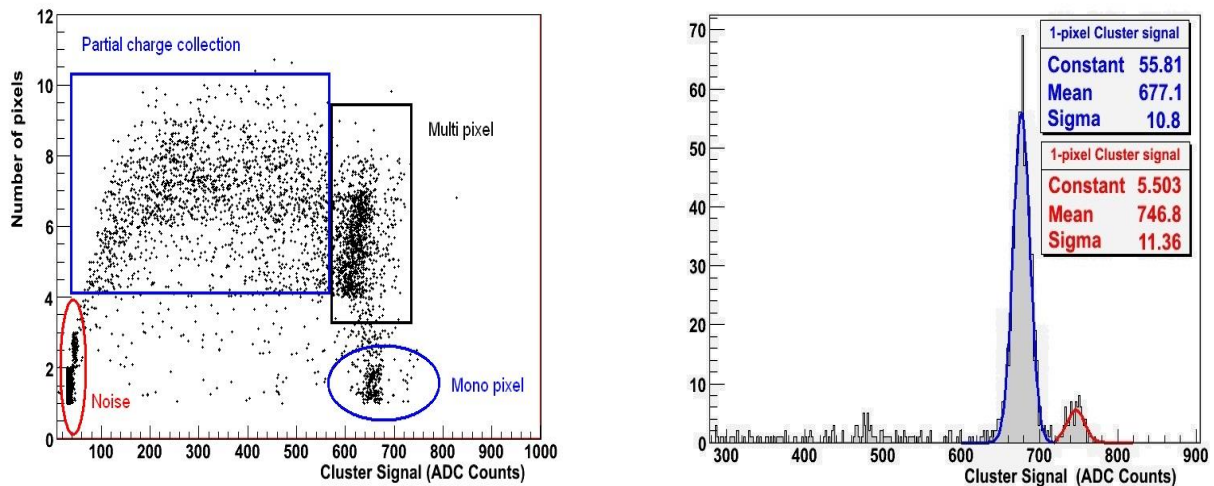


Figure 5.8 (a) Correlation among cluster signal and number of pixels in the cluster at maximum gain settings. (b) Distribution of the cluster signal for ^{55}Fe photons at unitary gain; the two energy peaks (5.9 and 6.4 keV) are well separated.

To disentangle this effect the cluster signal has been studied as a function of the number of pixels belonging to the cluster (Figure 5.8(a)). Four regions are clearly identified in the plot:

- The noise region (circle in the lower left part) where the pixels that reach the threshold level can be found: with a 6 sigma value of, in this case, about 26 ADC.
- The partially collected region (square in the upper left part) where are located the events with an important part of the charge not collected (due to the interaction depth of the photon).
- A mono-pixel region in the lower right part.
- A multi-pixel region in the upper right-hand part, where the data corresponds to a fully efficient charge collection.

A clear charge collection loss for multi-pixel clusters has been observed, of the order of 7-15%. Hence, in order to derive the absolute calibration for the detector only the monopixel clusters have been considered; in Figure 5.8(b) the spectra of the two ^{55}Fe energy peaks are presented.

5.3 Sensor absolute calibration

To measure the detector absolute calibration only monopixel clusters have been selected. Correlation plots could then be built (Figure 5.9(a)) for each gain settings and calibration relations could be found: 6.9 ± 0.1 ADC/keV for unitary gain, and 117 ± 1 ADC/keV for maximum gain. These results could then be converted into an equivalent pixel noise of respectively 36 ± 3.6 e and 6.5 ± 0.7 e for unitary and maximum gain.

In Figure 5.9(b) the response to the variation of the nominal gain of the device is reported (dots) together with the signal/noise behavior (stars) for ^{55}Fe photons. The difference between the linear response in signal (growing proportionally to the nominal gain value) and the behavior of the average SNR is due to the different electronic circuits involved before and after the value of 8; at low gains the noise is greatly influenced by the quantization error, whose importance decreases with the increase in nominal gain. Hence the increase in SNR up to a saturation value in the first part and a moderate linear increase in the second part.

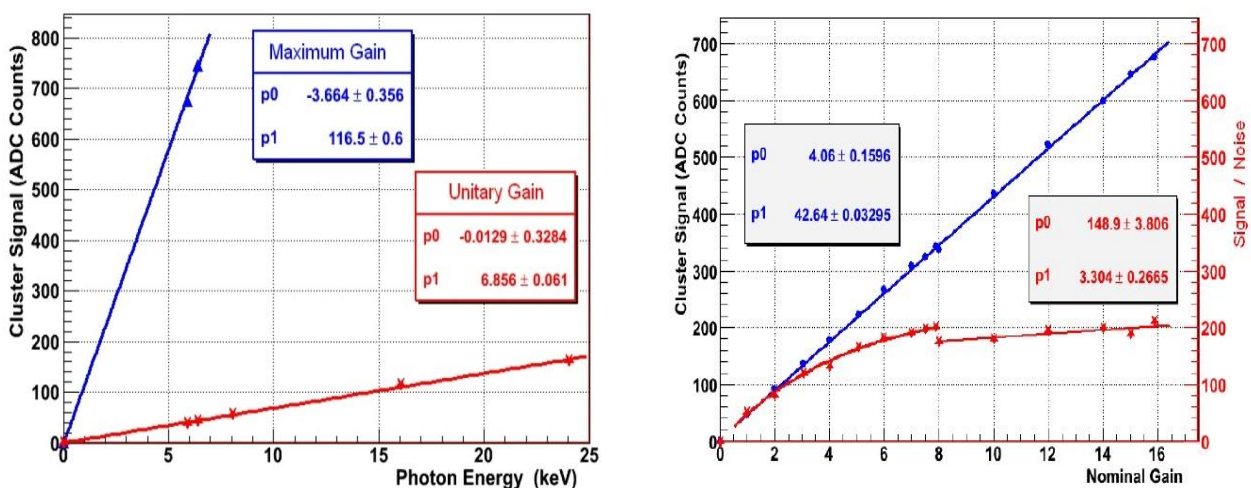


Figure 5.9 (a) Correlation between photon energy and peak cluster signal with a linear fit for minimum (stars) and maximum (triangles) gain. (b) Variation of cluster signal (blue) and cluster signal/noise (red) as a function of the device nominal gain.

The clustering algorithm is useful to better isolate the signal from the noise when only part of the charge is collected by the sensor. In Figure 5.10(a) the distribution of the cluster signal is plotted for either the 3x3 submatrix (empty) or the clustering algorithm (gray) when the noise region has been removed. It can be estimated that the cluster algorithm allows a better separation and a sensitivity even below 1keV while the 3x3 submatrix method stops at just about 1keV.

The dynamical range covered by the sensor can then be estimated between 2keV to 150keV for minimum gain and 1-8 keV for maximum gain. The variation of the cluster signal against temperature is shown in Figure 5.10(b) for ^{55}Fe photons yielding an approximate linear dependence with a signal variation of -0.15 ADC/°C.

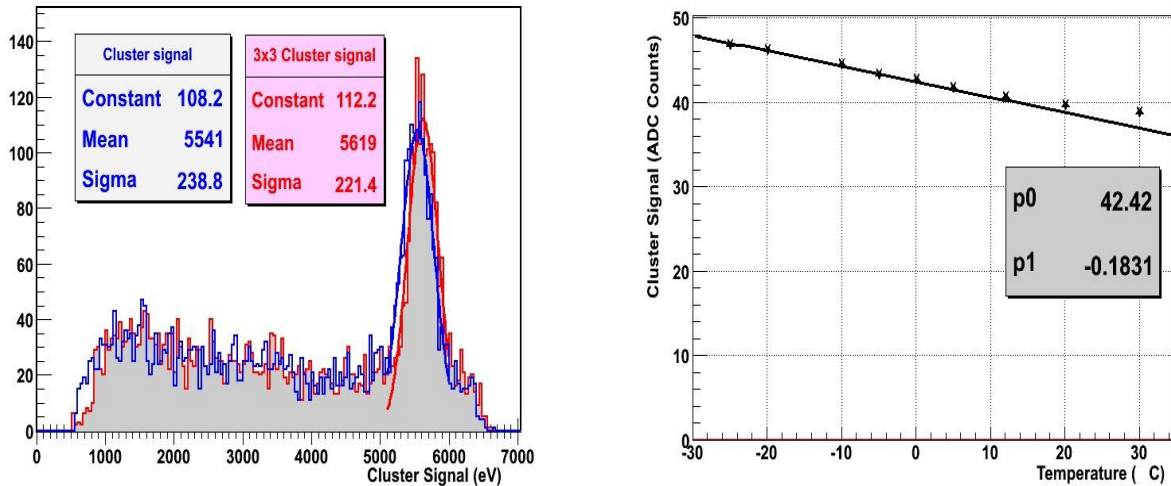


Figure 5.10 (a) Integral distribution of cluster frequency vs cluster signal for ^{55}Fe photons (at maximum gain) for the 3x3 submatrix and the cluster algorithms. (b) Temperature dependence of cluster signal for unitary gain.

5.4 Charge particle response for MTV9V011 sensor

The detector was put in October 2009 on the PS 12GeV proton beam at Cern to measure the response to a MIP. Tests have been performed at different nominal gains but in the following only the results related to the maximum gain (15.88) will be presented, configuration offering the best performances. Figure 5.11 shows an event display with one electron hitting the sensor orthogonally; the signal is shared among few pixels.

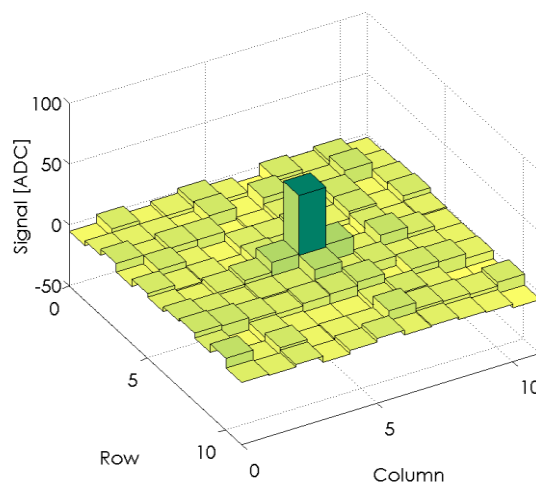


Figure 5.11 Typical response of the MT9V011 pixels around the crossing point of a 12GeV proton.

To estimate the amount of signal-sharing among adjacent pixels, for each frame the sum of the signals of the 9x9 submatrix centered on the seed pixel is computed and it is used to normalize the signal of each pixel of the submatrix. In Figure 5.12(a) is shown the distribution of the average fraction for the 9x9 submatrix; most of the signal is concentrated into the seed pixel (57%). To reach the level of 97% of the

collectable charge it is enough to use the a 5x5 submatrix while with a 7x7 submatrix all the generated charge is collected.

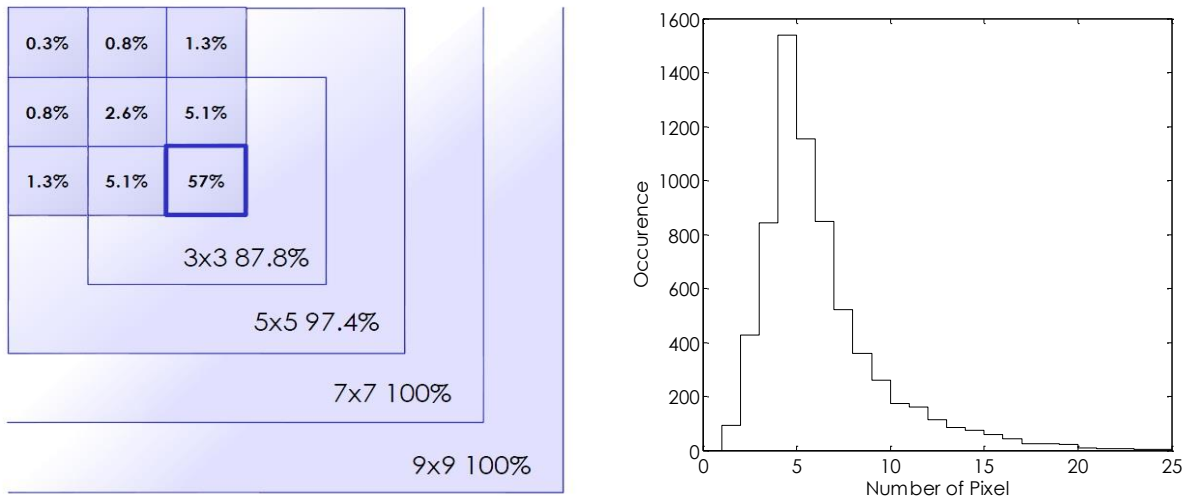


Figure 5.12 (a) Distribution of the collected charge around the impact point for the MTV9V011 exposed to a 12GeV protons. (b) Distribution of the number of pixels belonging to the cluster for 12GeV incoming protons.

The average cluster size of 5.6 pixels (Figure 5.12(b)) are quite similar to the photon's one, but the distribution is different having a single peak and a long positive tail due to the δ -ray and energy deposition fluctuations. The main reason for the widening of the area where the charge released by the electrons should be collected is partially due to the longer creation path ($\sim 4.0\mu\text{m}$ of epitaxial layer) for electron-hole pairs, with respect to the almost point-like case (order of $1\mu\text{m}$) for photons; this allows for a greater diffusion before the charge collection by the pixel's photodiodes.

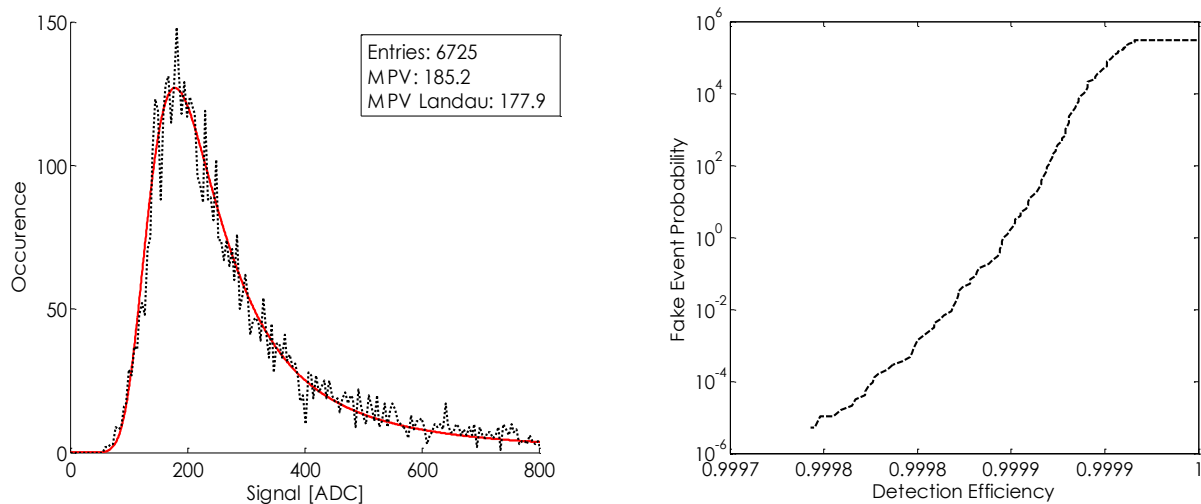


Figure 5.13 (a) Signal distribution of the 5x5pixels cluster related to the MTV9V011 exposed to a 12GeV protons and (b) its detection efficiency vs fake event probability.

In Figure 5.13(a) the signal distribution of a 5x5 submatrix, when the sensor is exposed to a 12GeV protons beam, is shown. The distribution is fitted with a Landau convoluted with a Gaussian in accordance with the theory reported in Chapter 2. The acquisition threshold is about the 30% of the expected charge in the seed pixel and does not significantly modify the cluster signal distribution.

The peak is located at 185.2 ± 3 ADC but considering the noise contribution, the real peak is located at a lower value of 177.9 ± 1 ADC. Using the absolute calibration given from the x-ray (2.3 ± 0.2 e/ADC at maximum gain) we can convert this value in terms of electron-hole pairs resulting in 409.1 ± 16 e, corresponding to an equivalent sensitive thickness of 7.4 ± 0.4 μm . This value is well comparable with the nominal $4.0\mu\text{m}$ of epitaxial layer declared by the manufacturer. It is known, indeed, that the ability to collect charge of sensors with this kind of technologies is limited by the epitaxial layer thickness [5.6].

The corresponding SNR for the 3×3 pixels cluster is estimated to be 23.9 ± 0.6 , while getting just the seed pixel, the SNR raises to 30.5 ± 1.1 . These results, together with the noise characterization, allows to estimate the detector efficiency with respect to the fake hit probability (Figure 5.13(b)); with a seed threshold of 6 times the single pixel noise, an efficiency of 99.98% with 1×10^{-5} fake hit probability is possible [5.7].

References

- 5.1 L. Servoli et al., *Use of a standard CMOS imager as position detector for charged particles*, Nuclear Physics B Proceedings Supplements, Volume 215, Issue 1, p. 228-231.
- 5.2 Aptina Imaging [Online] <http://www.apina.com/>.
- 5.3 Micron Technology, Demo2 User manual.
- 5.4 Micron Technology, DevWare Midlib documentation.
- 5.5 L. Servoli et al., *Characterization of Standard CMOS Pixel Imagers as Ionizing Radiation Detector*, JINST 5 P07003 (2010) 001-013.
- 5.6 W. Dulinski et al., "CMOS Monolithic Active Pixel Sensor for Minimum Ionising Particle Tracking Using Non-Epitaxial Silicon Substrate" IEEE Transactions on Nuclear Science, vol. 51, no. 4, pp. 1613-1617, 2004.
- 5.7 L. Servoli et al., *Use of a standard CMOS imager as position detector for charged particles*, Nuclear Physics B Proceedings Supplements, Volume 215, Issue 1, p. 228-231.

Chapter 6.

Vertical integration technologies for Pixel Detectors

Typical tracking systems for particle trajectory reconstruction in HEP experiments are usually based on different separated sensing layers, featuring pixels and/or strips sensitive elements. In this chapter the results obtained by an innovative approach to particle tracking will be presented. Such an approach is based on CMOS Active Pixel Sensors layers, monolithically integrated in a all-in-one chip featuring multiple, stacked, fully functional detector layers capable to provide momentum measurement (particle impact point and direction) within a single detector. This will results in a very low material detector, thus dramatically reducing multiple scattering issues. To this purpose, we rely on the capabilities of the CMOS vertical scale integration (*3D IC*) technology.

The usual approach of 3D integration in a vertex detector framework could be described as heterogeneous integration in the sense that it devotes different tiers to the sensing layer, and to the analog and digital circuitry. Such an approach has certainly some advantages as it guarantee a 100% fill-factor of the detecting area while at the same time allowing for some on-chip signal processing. On the other hand such an architecture cannot be strictly considered "monolithic".

In our approach, instead of using different tiers of the stacked 3D structure for heterogeneous integration, identical fully-functional CMOS APS matrix detectors, including both sensing area and control/signal elaboration circuitry, could be stacked in a monolithic device by means of Through Silicon Vias (TSV) connections. The information coming from thinned multiple stacked layers could be usefully exploited to extend the detection capability of the monolithic sensor. In principle, such a detector would be capable of giving accurate estimation not only of the impact point of a ionizing particle (with spatial resolution in the μm range), as well as of its incidence angle (with angular precision around 1°) [6.1].

A first chip prototype has been fabricated within a multi-project run using a 130nm CMOS Chartered/Tezzaron technology, featuring two layers bonded face-to-face. Tests have been carried out on full 3D structures, providing the functionalities of both tiers. To this purpose, laser scans have been carried out using highly focused spot size obtaining coincidence responses of the two layers. Tests have been

made as well with x-ray sources in order to calibrate the response of the sensor and with 3MeV protons. Encouraging results have been found, fostering the suitability of both the adopted 3D-IC vertical scale fabrication technology and the proposed approach for particle tracking applications.

6.1 The two-layer 3D CMOS APS detector

A first chip prototype has been fabricated within a multi-project run using a 130nm CMOS 3D Chartered/Tezzaron technology [6.2, 6.3], featuring two layers bonded face-to-face. The top (outer) tier has been thinned down to less than $10\mu\text{m}$, while the bottom (inner) tier has not been modified with respect to the standard planar (2D) realization. The two tiers host two almost identical (i.e. mirrored) layouts, featuring several corresponding test structures, namely single pixels, as well as different matrices, e.g. featuring 5×5 and 16×16 pixels (Figure 6.1(a)). Each pixel is based on the standard three transistors (3T) active pixel architecture, featuring $10\times 10\mu\text{m}^2$ size with different sensitive element (photodiode) layout. In particular, a *small* sensitive area with small capacitance (aiming at maximizing the charge to voltage conversion gain) and a *large* sensitive area (aiming at maximizing the fill-factor of the detector) (Figure 6.1(b)). The structures of both tiers can be read out in parallel by means of dedicated output bond pads, located at the backside of the top tier.

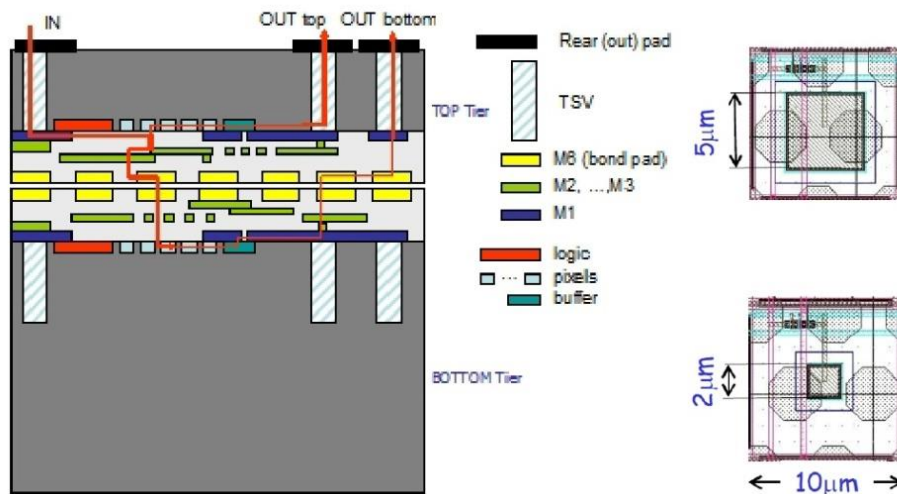


Figure 6.1 (a) Schematic cross-section of the two tiers (sketch not to scale). (b) Large (top) and small (bottom) pixel layouts.

6.2 Simulation activity

Before to realize the RAPS04 chip an extensive simulation activity has been carried out aiming at the optimization of the detector geometry for the specific task at hand. The simulations were made by means of the software ISE-TCAD [6.4], starting from a simple 2D section of a 7×7 pixels submatrix. Mixed-mode simulations have been carried out: each photodiode, featuring a sensitive area of $2\times 2\mu\text{m}^2$ (small

photodiode), has been coupled to the three transistor circuit APS scheme (Figure 6.2). A MIP stimuli response has been therefore simulated, considering the distribution of the charge for an impinging particle. All the results were obtained by considering both charge drift and diffusion components for a typical CMOS substrate doping concentration and under biasing conditions.

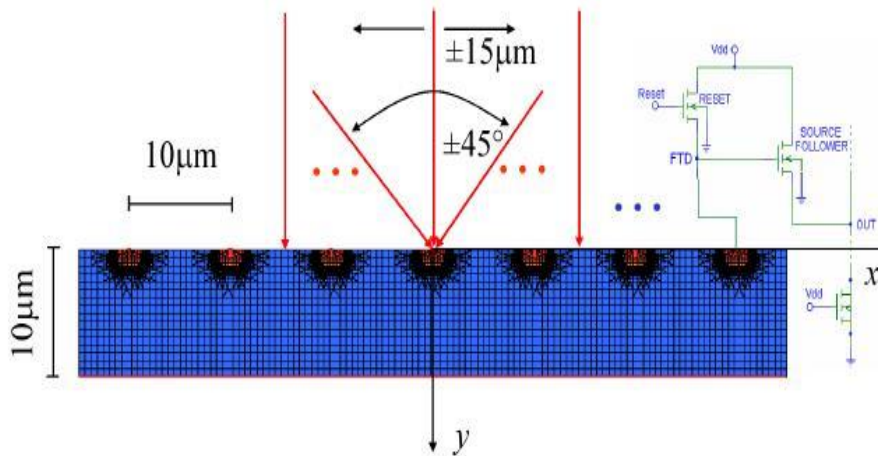


Figure 6.2 2D cross-section of a CMOS Active Pixel Sensor sub-array (7 pixels).

In order to evaluate the suitability of having multiple spatially close measuring layers the impact point and the incidence angle reconstruction have been performed, starting from the voltage responses at the pixel outputs. In particular, we considered a cluster signal, featuring three pixel responses, namely the seed pixel and the two neighboring ones.

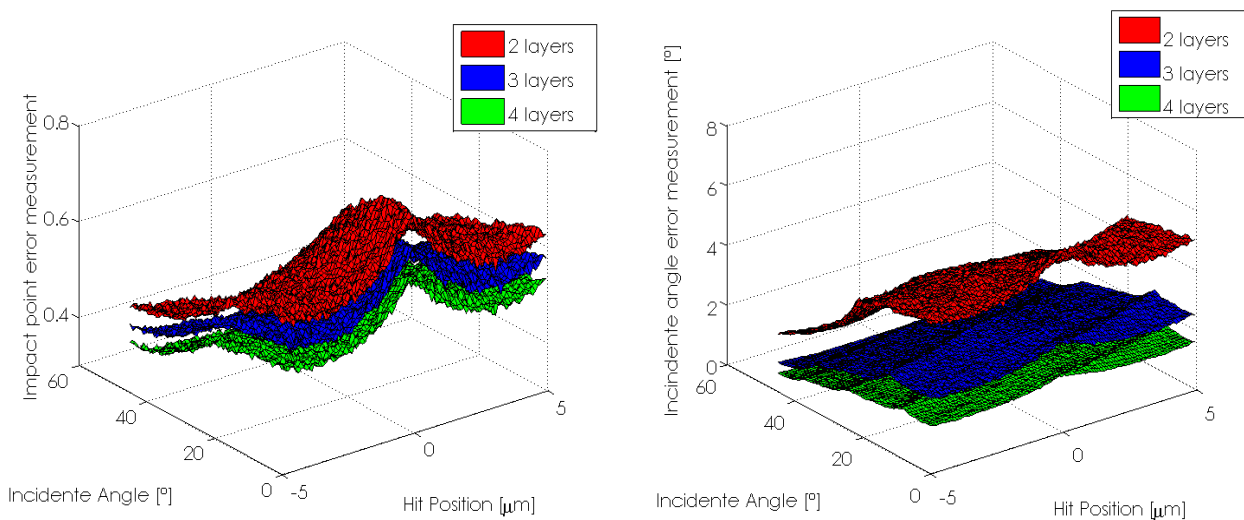


Figure 6.3 Error in the (a) impact point and (b) incident angle calculation as a function of the incident angle and hit position.

The equivalent noise voltage was added to the voltage response of each pixel using a Gaussian distribution. The hit position and angle were therefore reconstructed from the voltage response of each pixel involved in the cluster, by a weighted average of the voltage signals between pixels pertaining to the same layer and by a linear fitting of the information obtained from different layers (namely, we considered as straight line the trajectory of the particle inside the detector substrate).

A comprehensive analysis of the four layers sensor structure is reported in Figure 6.3. In particular, we considered an impact point spanning from a left half-pitch with respect to the central pixel to a right half-pixel and incidence angle ranging from 0° to 45° with respect to the normal incidence.

This four layers sensor structure will result in a spatial resolution of about $1\mu\text{m}$ and a resolution in the detection of the incident angle of about 1° .

6.3 Functional characterization

For electrical and functional characterization a suitable read-out setup has been devised and fabricated. In particular, an advanced optical workbench with IR, UV, and VISible laser heads with micro-focusing (spot size below $2\mu\text{m}$) and micro-positioning (scan step $0.21\mu\text{m}$) capabilities has been used. It allows up to four sensors parallel read-out for track reconstruction and spatial resolution analysis, as well as 2D scans for surface mapping [6.5]. Coincidence responses to a focused IR spot of corresponding outer and inner matrices have been obtained. The coincidence responses can be clearly observed by translating the spot along the matrix (i.e. along the chip surface) and looking at the different responding clusters of pixels (see Figure 6.4(a)).

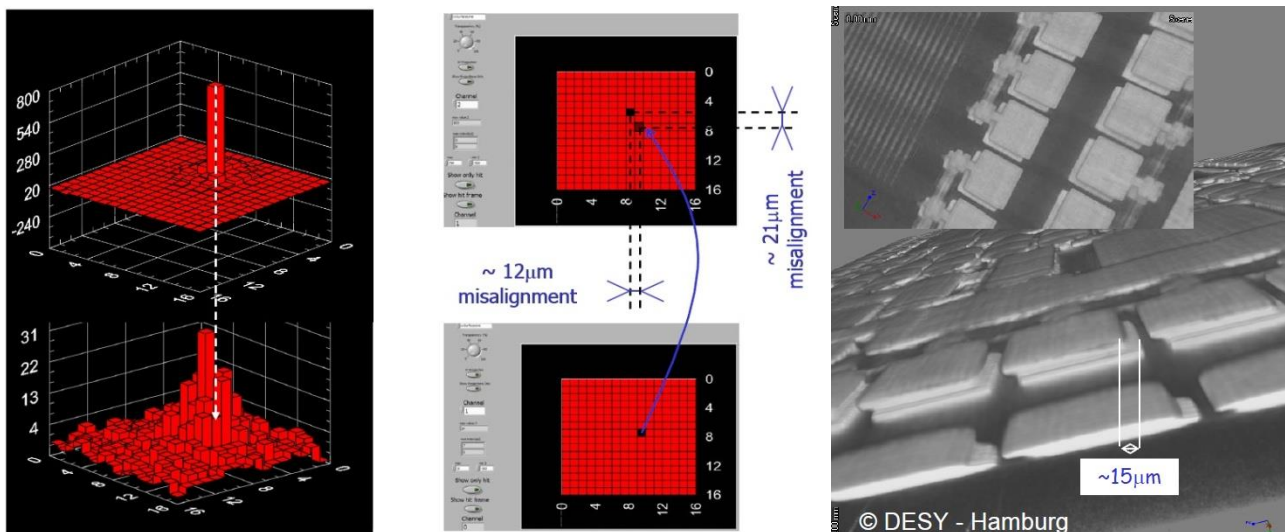


Figure 6.4 (a) Coincidence responses to a IR laser of the 16x16 outer (top) and inner (bottom) matrices. (b) Differences between peak response coordinates of the top and bottom matrices. (c) Computed tomography (CT) of the stacked die.

The focusing capabilities allow the stimulation of a single pixel on the top, back-side illuminated matrix, while a wider and spread-out response has been obtained from the bottom matrix, due to the scattering effect of the metal layers between the two chips and to the shielding effects of the bond-point metal-6 octagons, whose dimensions ($3.4\mu\text{m} \times 3.4\mu\text{m}$) are of the same order of the pixel size. Misalignments of about $12\mu\text{m}$ in one direction and of about $20\mu\text{m}$ on the orthogonal one have been demonstrated (Figure 6.4(b)). These findings have been confirmed by deeper investigations carried out by means of computed tomography (CT) scans at DESY, Hamburg. In particular, Figure 6.4(c) shows a detail of the pad regions. From the dimensions of the pads ($120\mu\text{m}$) the estimated misalignment, which is of the order of 10% of the

pad size, is about $15\mu\text{m}$, in good agreement with the previous findings. It should be emphasized, however, that the significant misalignment between the two tiers does not prevent the communication from the bottom tier to the top tier. The implemented circuits actually features TSV interconnections only at the chip periphery (e.g. at the pad level). The huge number of TSVs in these regions, even if the two tiers are tilted/shifted, still guarantees the electrical connections between the pads.

Surface scans can be carried out as well, in order to evaluate the response of the pixel as a function of the spot positions. The micro-focusing and micro-positioning capabilities allow very deep investigation of the point spread response of the matrix. The response to a back-side illumination with visible light (531nm) is reported in Figure 6.5(a). Clear peak responses, corresponding to the sensitive regions of the pixels, can be observed. On the other hand, a broader response has been obtained with front-side illumination with visible light (780nm): the effects of the metal layer tend to spread out the laser stimuli. Moreover, the shielding effect of octagonal bond-points can be observed as well: in Figure 6.5(b), the superimposition of the actual layout with the response of a 3×3 pixel submatrix is reported.

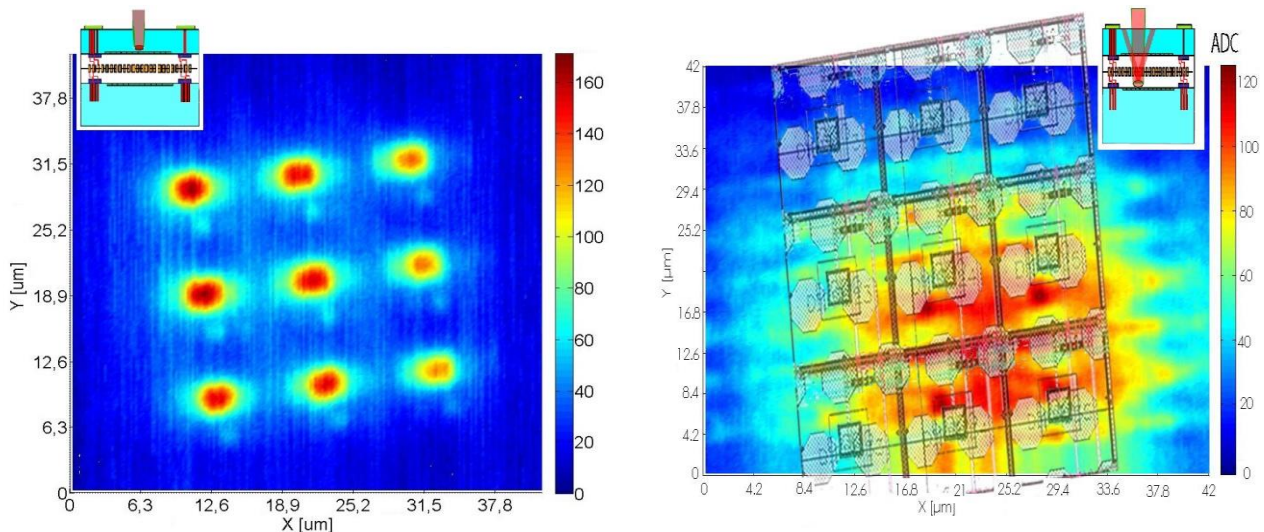


Figure 6.5 (a) Back-side illumination of a 3×3 small submatrix: no metal shielding effects, regular pattern response to a x-y laser scan. (b) Front-side illumination of a 3×3 small submatrix: effects of metal-layers and bond-points on the response to a x-y laser scan.

6.4 Signal to noise evaluation: x-rays analyses

A comprehensive noise analysis has been carried out, by considering the overall contribution of temporal and spatial noise. Very similar noise figures have been obtained for corresponding pixels of outer (top) and inner (bottom) tiers. Small pixel architecture resulted in a higher noise ($\sim 1.8 \pm 0.5$ ADC), as expected, due to the kT/C noise contribution which is significantly greater for the small pixel (due to the lower sensitive region capacitance) with respect to the large pixel (1.0 ± 0.3 ADC).

An Amptex Mini-X x-ray source has been used for sensor calibration purposes with photons of different energies. In particular, Fe and Cu targets have been used in fluorescence mode. A good linearity of the sensor response has been found at different photon energies: from the expected energy peak deposition of

Fe and Cu targets (6.4keV and 8.1keV, respectively), the number of electron-hole pairs generated within the silicon substrate can be estimated.

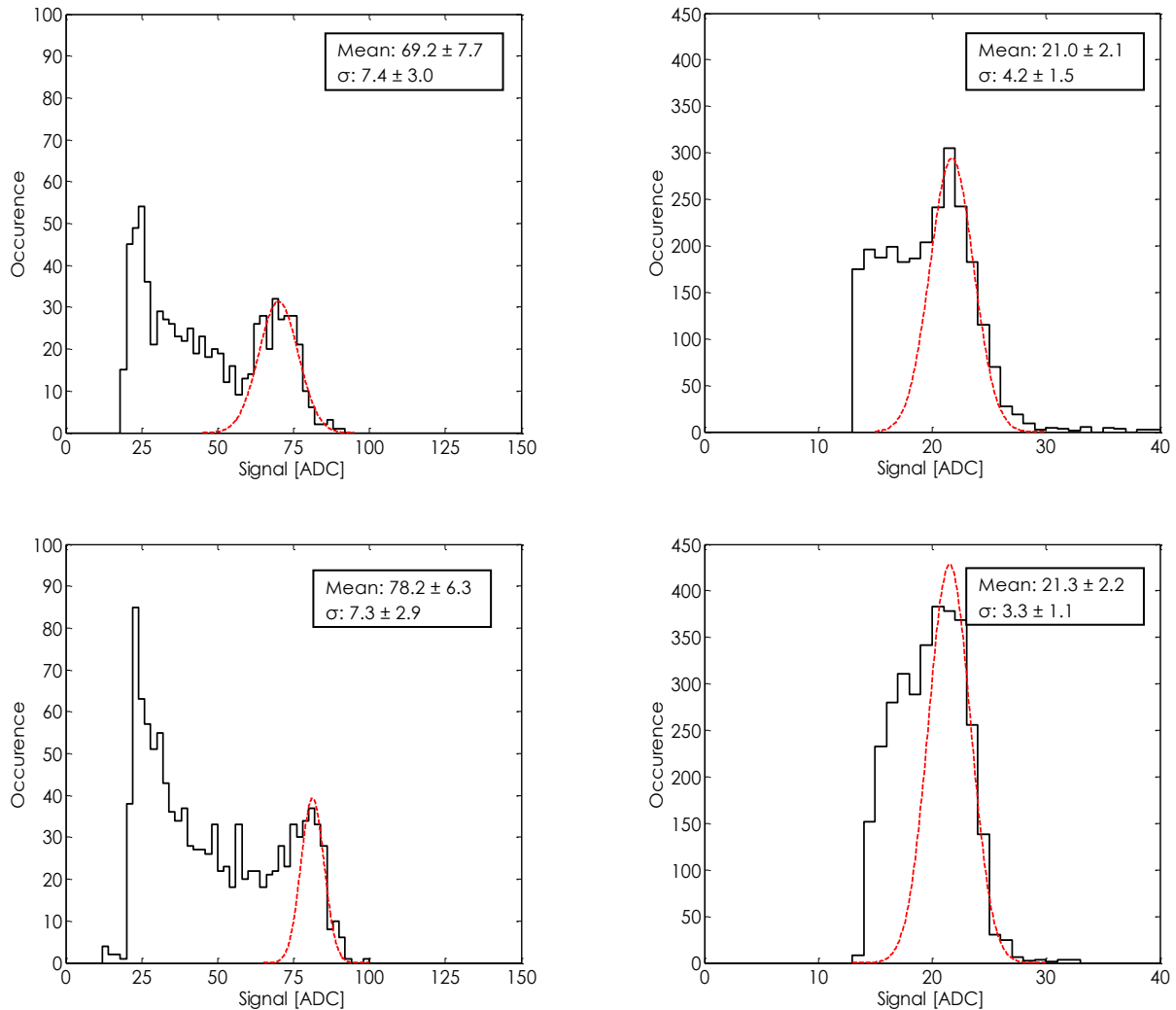


Figure 6.6 Pixel matrices x-rays responses (Fe target): cluster signal distributions for small inner matrix (top left), small outer matrix (bottom left), large inner matrix (top right) and large outer matrix (bottom right).

The peak positions on the cluster signal distributions of Figure 6.6 correspond to almost complete charge collection; therefore, sensor calibration can be carried out, allowing an estimation of the conversion gain for the small matrix of around 22 e/ADC for the outer tier and 25 e/ADC for the inner tier and for the large matrix of around 88 e/ADC for the outer tier and 86 e/ADC for the inner tier (Figure 6.7). From this point of view, at least for x-ray photons, no particular worries about signal coming from top (thinned) tier with respect to signal coming from bottom tier have been experienced.

Eventually, after calibration, the overall (spatial and temporal) measured noise was around 41 ± 11 e for the small photodiode and 88 ± 26 e for the large photodiode.

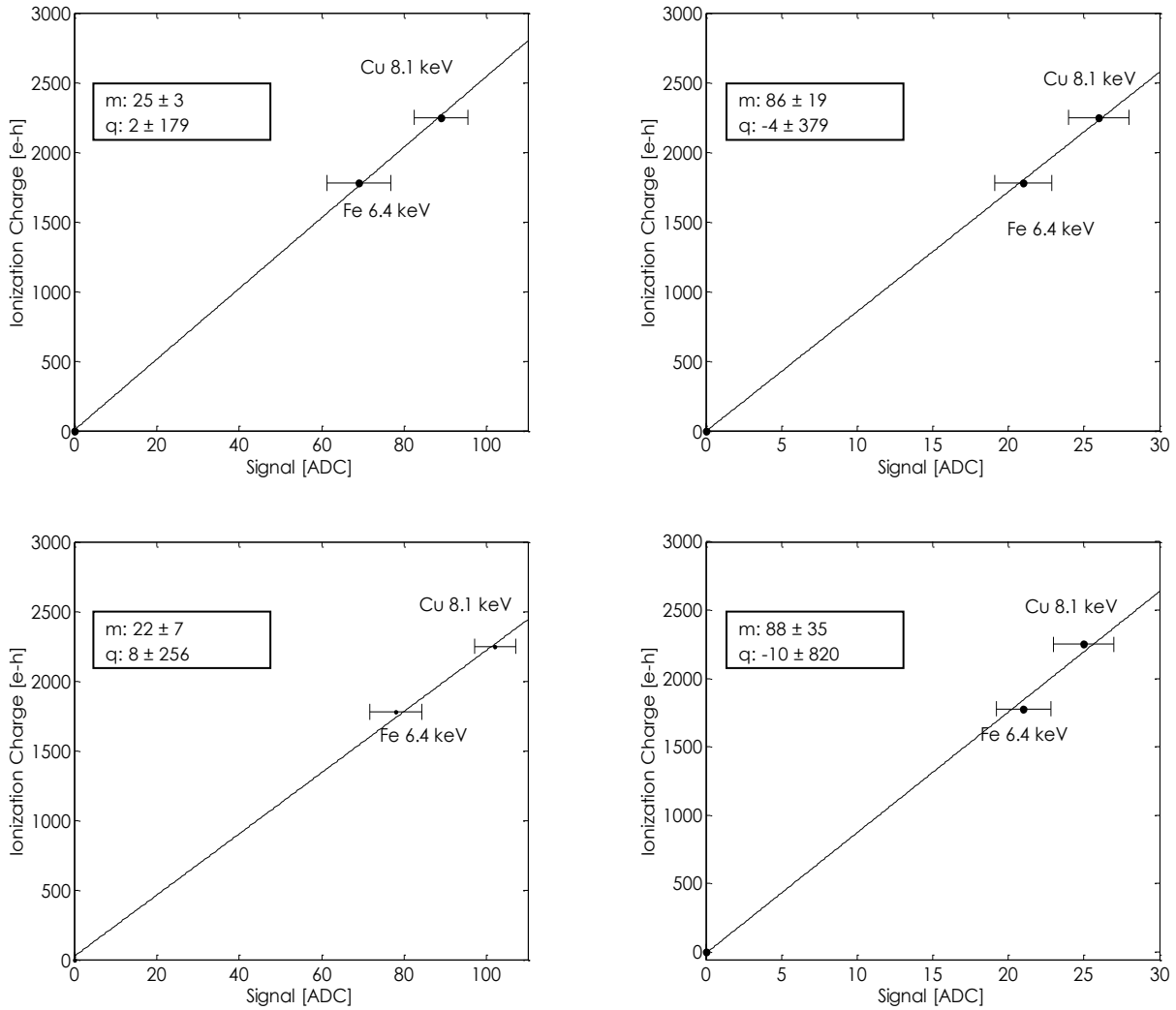


Figure 6.7 Matrices calibration: responses (ADC) to different x-ray photons for small inner matrix (top left), small outer matrix (bottom left), large inner matrix (top right) and large outer matrix (bottom right).

6.5 Charge particle response for the RAPS04 sensor

The detector was tested in July 2012 on the LABEC 3MeV proton beam at INFN Firenze to measure the response to a ionizing particles. According to the theory [6.6] a 3MeV proton releases in the silicon 20 keV/ μm instead of the 0.3 keV/ μm typical of MIP, allowing to achieve high SNR.

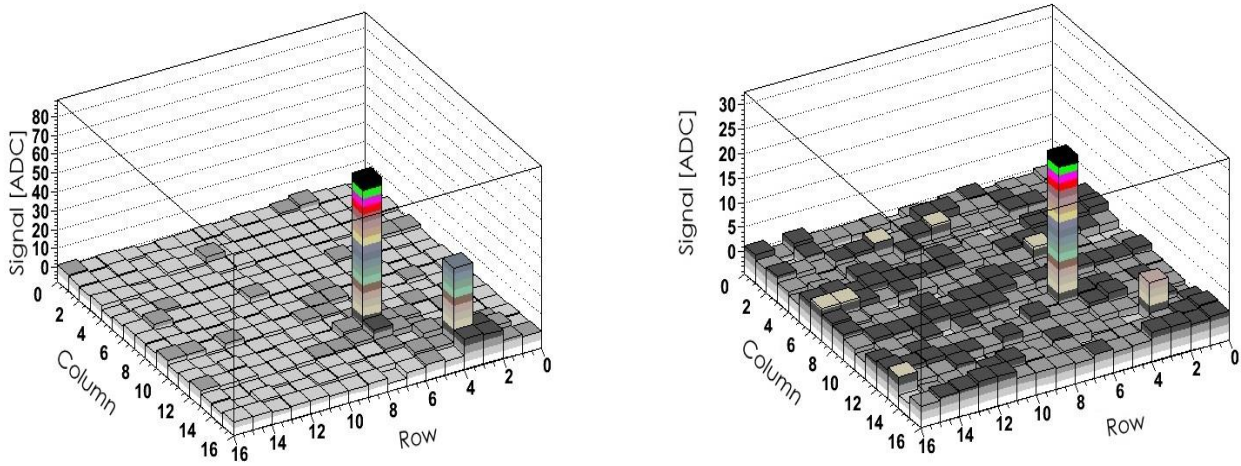


Figure 6.8 Response of the (a) inner layer and (b) outer layer to two 3MeV protons of the matrix with large photodiode.

Figure 6.8 shows one event display with two protons hitting both the layers simultaneously. It can be noticed also in this figure the misalignment between the two tiers. The signal appears entirely confined into one pixel and the charge collected by the pixels surrounding the central one is extremely low.

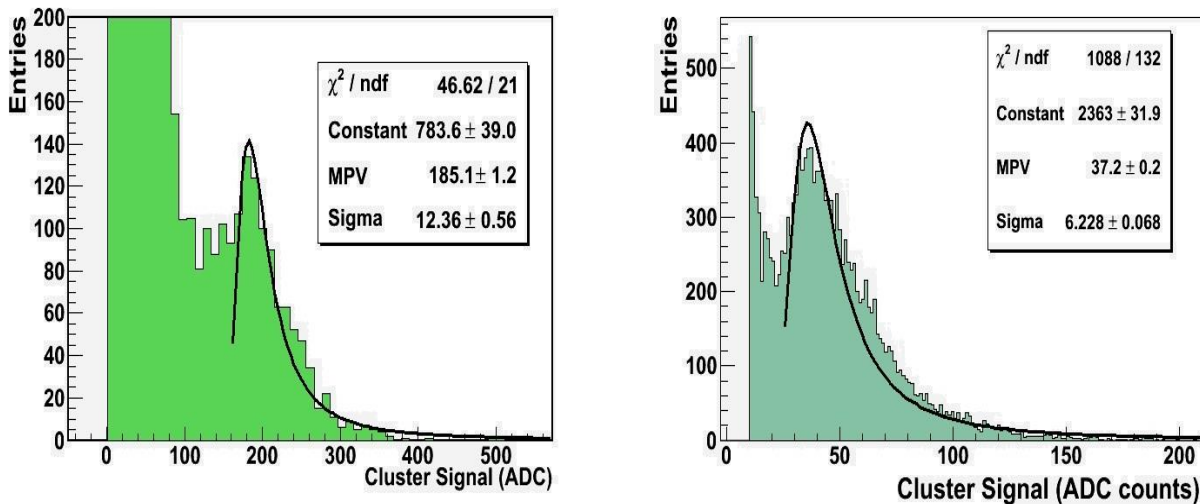


Figure 6.9 Signal distribution of the 3x3 pixels cluster related to the matrix (a) small and (b) large photodiode exposed to a 3MeV proton.

The Figure 6.9 shows the 3x3 pixels submatrix signal distributions with the Landau fit. The fit returns 185.94 ± 1.2 ADC and 37.2 ± 0.2 ADC as the MPV of the Landau distribution respectively for the small and large photodiode. Knowing the conversion factor e/ADC , retrieved from the x-ray calibration, we can translate the MPV to the equivalent electron-hole pair which reads: 4631 ± 30 e and 3199 ± 17 e respectively for the small and large photodiode. From the theory $4631e$ and $3199e$ corresponds to a equivalent thickness of the sensitive region of about 0.8 ± 0.1 μm and 0.57 ± 0.03 μm .

The SNR achieved with the 3MeV protons is 103 for the small photodiode and 37 for the large photodiode. If, starting from these results, we try to calculate the expected SNR for a MIP we find about 1.4 for the small photodiode and 0.5 for the large photodiode. This SNR expectation is not encouraging and for the next chip submission we need to find some solutions for improving this value. On the other

hand this test showed the capabilities of the RAPS04 concept to provide a coincident response of the outer and inner layers to single ionizing particle.

References

- 6.1 D. Passeri, L. Servoli and S. Meroli, *Analysis of 3D stacked fully functional CMOS Active Pixel Sensor detectors*, 2009 JINST 4 P04009.
- 6.2 3DIC Consortium, <http://3dic.fnal.gov/>.
- 6.3 P. Garrou, C. Bower and P. Ramm, *Handbook of 3D Integration*, Wiley-VCH, (2008).
- 6.4 Ise-Tcad Synopsys [Online] http://www.ece-help.gatech.edu/software/ISE_TCAD.html
- 6.5 D. Passeri, et al., *A laser test system for characterizing CMOS active pixel sensors*, Nucl. Instr. and Meth. A 565 (2006) 144.
- 6.6 D. Passeri et al., *3D monolithically stacked CMOS active pixel sensor detectors for particle tracking applications*, 2012 JINST 7.
- 6.7 Particle Data Group PDG, *Passage of particle through matter*, Nuclear and Particle Physics, vol. 33, no. 27, pp. 258-270, July 2006.

Chapter 7.

Precision physics measurements with silicon Pixel Detectors

In this chapter the pixel sensors, which have been previously introduced and characterized, have been employed to perform high precision physics measurements. In particular the Micron CMOS sensor MT9V011 featuring high SNR and elevated pixel granularity has been used to study in more details the interaction between radiation and matter and the charge diffusion mechanisms of the minority carrier in the silicon, managing to get results with precision never achieved before.

New methods and innovative approaches were implemented to extract basic transport parameters (minority carrier diffusion length, minority carrier lifetime, width of the region at maximum CCE) using mathematical procedures.

7.1 The grazing angle method

In the grazing angle configuration the sensor is put parallel, rather than perpendicular, to the particles beam. The idea of using such a configuration is to have a solid state ionization chamber with high granularity for following in great details the passage of the particles into the silicon, monitoring especially its position and energy loss. Due to the huge number of reconstruction points along the “planar” detector (up to 640 for the MT9V011) and to the negligible effect of the multiple scattering we would potentially allow for a precise determination of the particle trajectory and of the energy loss in layers few micrometers thick (i.e. $5.6\mu\text{m}$ for the MT9V011). An illustration of the idea is given in Figure 7.1.

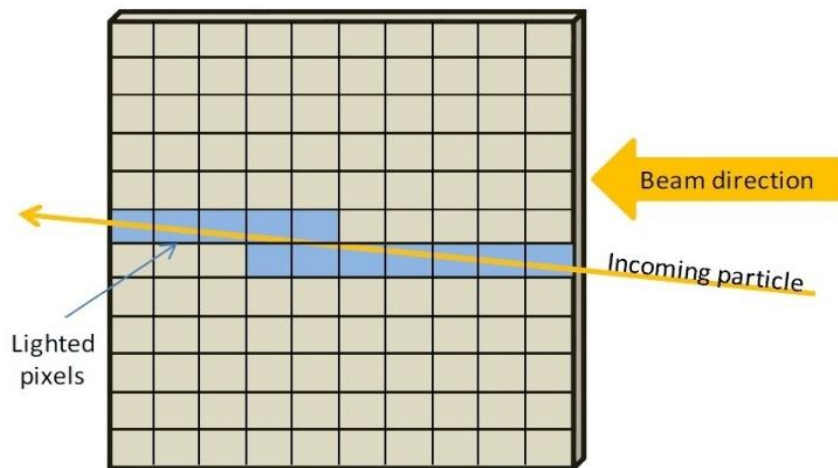


Figure 7.1 Track reconstruction using a pixel sensor parallel to the particles beam; an illustration of the idea.

In our grazing angle approach [7.1], the charged particle crosses several pixels pertaining to the single planar detector, each one at a different depth (see Figure 7.2(a)), depositing a known amount of energy and producing a voltage drop (ΔV) at each photodiode. The incident angle α is strictly related to the measurable track length R by the expression $R=d/\tan(\alpha)$ where d is the sensitive layer depth of the sensor.

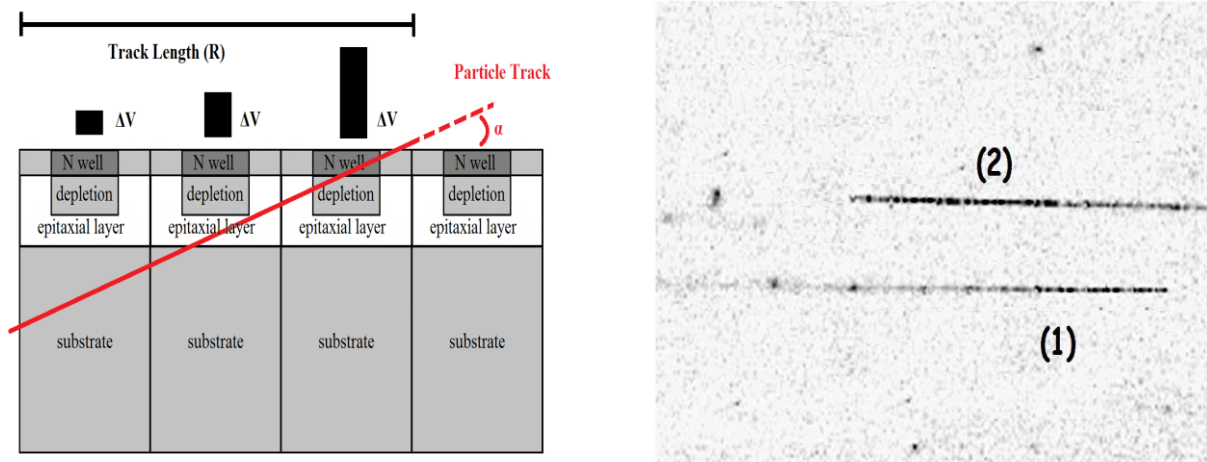


Figure 7.2 (a) Scheme of grazing angle method: several pixels are hit by the same track.
 (b) Online display of two simultaneous tracks entering the sensor from opposite sides (particles coming from the right). Track entering from sensor surface (1) and from sensor back (2).

For a given incidence angle α , the n^{th} pixel (i.e. at a certain distance with respect to the incidence entrance point) in the track is always crossed by an incident particle at the same depth. In order to keep under control (e.g., within a small error) the charge generation depth, only particles having in the same length (in pixel unit) within the array are selected.

For each pixel position a signal distribution could be built. The MPV of this distribution, for each pixel position, will depend on the generation depth. The track will be detected with a sharper definition, namely higher signal, near the sensor surface, whereas unfocused response is obtained when charge is deposited deeper in the bulk (worse S/N and greater spatial diffusion of charge), as can be seen in Figure 7.2(b) where the online display of two simultaneous tracks entering the detector from opposite sides is visible.

The pixel signal evolution along the track is consistent with track 1 entering from the surface side and track 2 from the back side, considering a beam direction from the right to left of the picture. In other words, brightest pixels at the right hand side of track 1 could be ascribed to charge generation closer to the surface leading to a greater charge collection efficiency.

To check the suitability of the approach, a dedicated mechanical support has been devised and implemented. In particular, a rotational stage allowing for the fine tilt of the sensors with respect to the beam direction has been used (Figure 7.3). Of course the grazing angle choice was dictated by the sensor geometrical constraints.

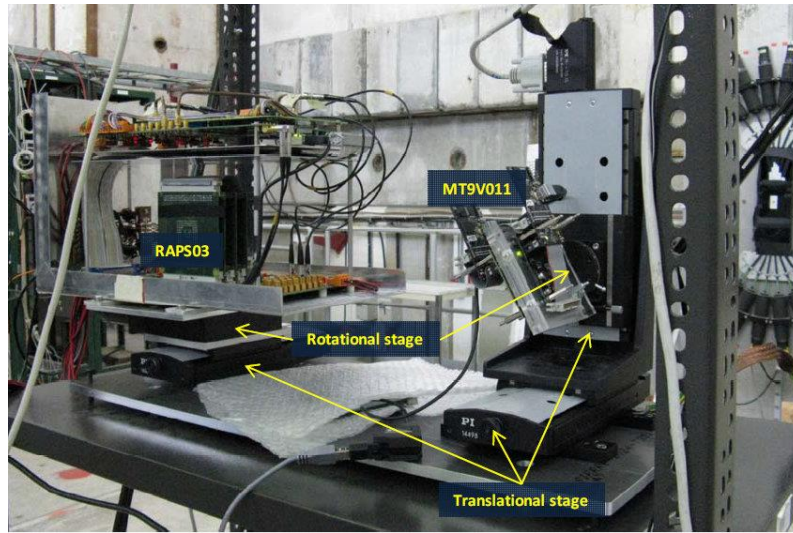


Figure 7.3 Test Setup at CERN Proton Synchrotron.

A track finding algorithm has been implemented to select good tracks and to reject background signals (e.g. noisy pixels, short tracks) [7.2].

The algorithm detects all the pixels with a signal greater than two times the pixel noise (hit pixels) and it defines a list. The row and column coordinates of these pixels are then analyzed to regroup them in tracks. The algorithm starts from a hit pixel not yet belonging to any track (track seed), and it looks in the list for some other unclassified pixels in the proximity of all the pixels of that track. If some pixel is found, it is included in the track and the procedure is iterated until no other pixel can be included (Figure 7.4(a)). If there are some ambiguous cases, i.e. two overlapping track, they are rejected, being the goal of this study to have good quality tracks. The implemented algorithm allows the separation of different tracks with a distance of only few pixels, as shown in Figure 7.4(b), where a secondary emission electron could be detected. In order to improve the algorithm functionality the tracks have to be parallel to the x-direction or y-direction of the sensor.

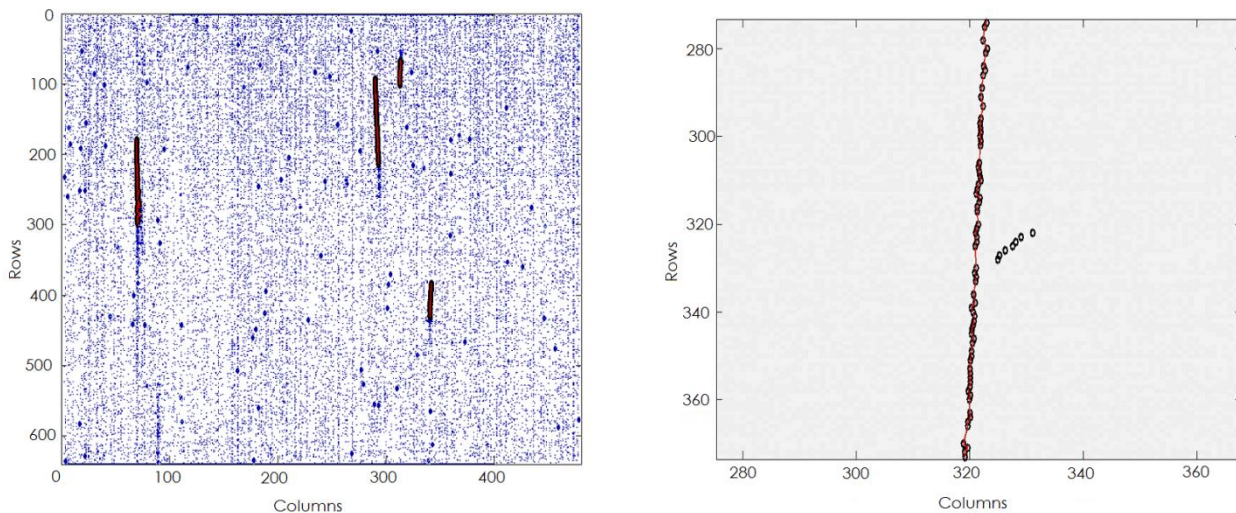


Figure 7.4 (a) Frame with four identified tracks. (b) Ionizing particle track with secondary emission.

Once the tracks have been found and defined, the automatic separation of tracks entering from the sensor surface with respect to the ones entering from the sensor backside has been implemented. Defining the track start as the pixel with the lowest absolute row coordinate, we could plot for each track the pixel response as a function of the pixel position with respect to the track start. The slope of the linear fit is defined as the pixel response slope (Figure 7.5(a)).

Tracks entering from the surface will have negative pixel response slope because the pixel response is at its maximum at low pixel coordinate and then tends to decrease towards zero with increasing pixel coordinate. For tracks entering from the back the reverse holds.

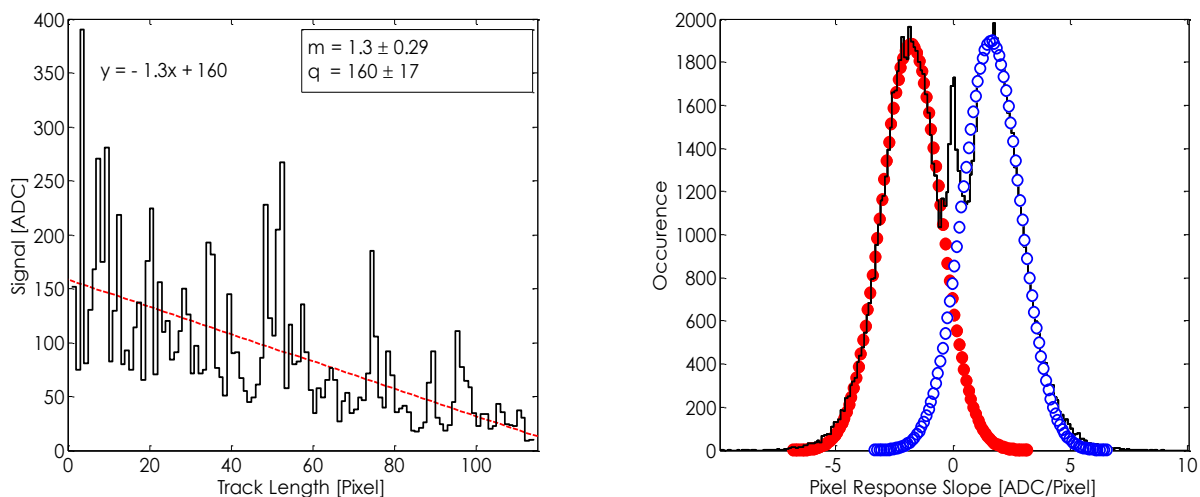


Figure 7.5 (a) Pixel response of one track entering from the surface with linear fit. (b) Distribution of the Pixel Response Slope measured with tracks entering from the sensor surface (filled circle) and from the sensor back (open circle).

The distribution of pixel response slopes is shown in Figure 7.5(b). It is possible to notice the two fitted Gaussian distributions, which represent the two different directions of incoming tracks (around the nominal direction of the beam, assumed as zero angle reference). The peak around zero represents all the incoming tracks parallel to the sensor surface, not selectable for the following analysis.

7.1.1 Grazing angle method for charge collection efficiency measurements

The knowledge of charge collection efficiency (CCE) profile plays a key role in optimization of detectors. It provides a detailed information on the fraction of charge generated in the sensitive volume which is subject to recombination. To accomplish the measurement of the charge collection efficiency (CCE) profile the most straightforward way is to generate a known amount of electron/hole pairs at a given depth and then to measure the pixel response. However, this is far from being an easy task because it requires an accurate and complex control of the setup. Various methods have been proposed in the past, mainly for microstrip devices, among which an IR laser, entering from a polished side of the silicon bulk, focused at different depths under the sensitive region [7.3] and a method using charged particles incident at a small angle on the sensor surface [7.4-7.6]. In all the previous cases the most relevant problem is the achievable spatial confinement for the charge generation, which is several micrometers at best.

In our custom grazing angle approach, as described in the former paragraph, charged particle crosses several pixels, each one at a different depth, depositing a known amount of energy and producing a voltage drop (ΔV) at each photodiode. Therefore, for each pixel position a signal distribution could be modeled by a Landau-Vavilov function [7.7]. The MPV for each pixel position will depend on the generation depth and could be used to build the CCE profile function.

Collecting all the tracks entering from one direction (for instance from the surface) with the same length (for instance 100 pixels) it is possible to build a signal distribution for each pixel position, beginning from the first pixels of the tracks to the last ones. In Figure 7.6 is shown the signal distribution for the 10th and for the 90th pixel of a track featuring a length of 100 pixel. Both distributions are well modeled by the Landau-Vavilov distribution, from which we can extract the MPV and its associated error.

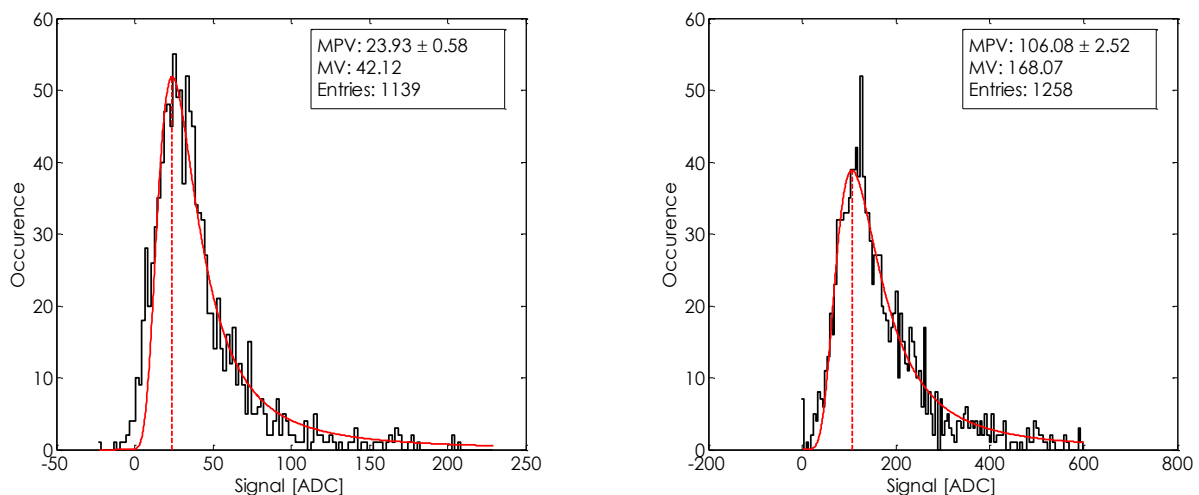


Figure 7.6 Signal distribution for the (a) 10th and for the (b) 90th pixel of a track featuring a length of 100 pixel

In Figure 7.7 is plotted the value of MPV as a function of the pixel position along the track. Position 0 is the track start (point closest to the sensor surface) and position 100 is the track end. It is evident the modulation of the response as a function of the pixel position along the depth of the track.

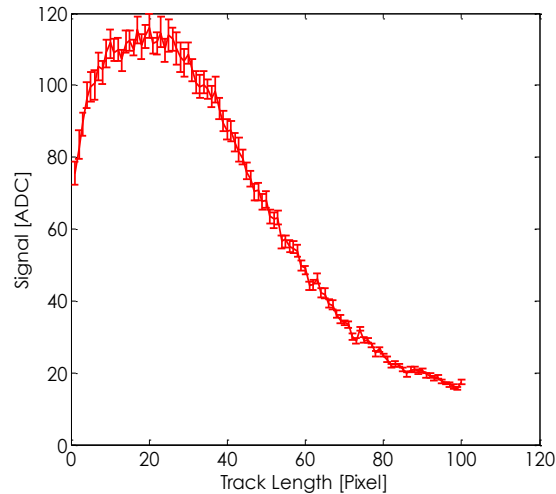


Figure 7.7 MPV as a function of the pixel position along the track

In Figure 7.8(a) are reported two profiles obtained using the tracks coming from the sensor surface (red) and from the sensor backside (blue). The high symmetry shows that the track finding algorithm is working very well.

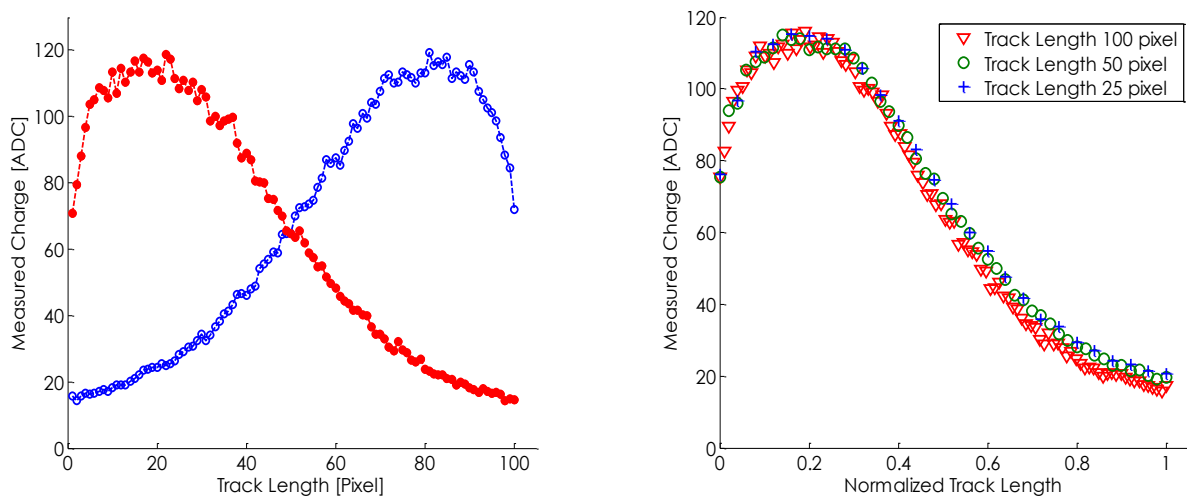


Figure 7.8 (a) Charge collection efficiency profiles measured with tracks entering from the sensor surface (filled circle) and from the sensor back (open circle). (b) Charge collection efficiency profiles measured with different track lengths.

We checked also that the method does not depend on track length. In Figure 7.8(b) are shown three profiles normalized to the track length, obtained with three different track length values (25, 50 and 100 pixels). The curves overlap very well, being the only difference a better “sampling” of the profile when longer tracks are chosen.

The final step to obtain a quantitative measure of the collection depth is to translate the horizontal scale unit from pixel units to length units (micrometers). To this purpose the following procedure has been used.

The total generated charge for an inclined track could be written as:

$$Q_{gen} = \sum_{i=1}^{N_{pixel}} Q_i \frac{\Delta R_i}{\sin \alpha} = \frac{1}{\sin \alpha} \sum_{i=1}^{N_{pixel}} Q_i \Delta R_i \quad (7.1)$$

where Q_i is the released charge per length units in the i^{th} pixel, ΔR_i is the pitch of the i^{th} pixel and α is the track incident angle on the sensor surface. The total measured charge (Q_{meas}) for an inclined track could be written as:

$$Q_{meas} = \frac{1}{\sin \alpha} \sum_{i=1}^{N_{pixel}} p_i Q_i \Delta R_i \quad (7.2)$$

where p_i is the charge collection efficiency for the i^{th} pixel of the track. The term

$$\sum_{i=1}^{N_{pixel}} p_i Q_i \Delta R_i \quad (7.3)$$

could be evaluated using orthogonal tracks, where $\alpha=90^\circ$ ($\sin\alpha=1$) and Q_{meas} is equal to the MPV of the Landau-Vavilov fit.

$$Q_{meas} = Q_{ort} = \sum_{i=1}^{N_{pixel}} p_i Q_i \Delta R_i \quad (7.4)$$

For particles at different incidence angles is then straightforward to obtain the value of α for each track, being $\alpha = \arcsin(Q_{ort}/Q_{meas})$ and hence the extraction of the depth scale of the CCE profile. Figure 7.9 illustrates how using longer tracks yields a finer sampling of the CCE, allowing a more detailed measurement.

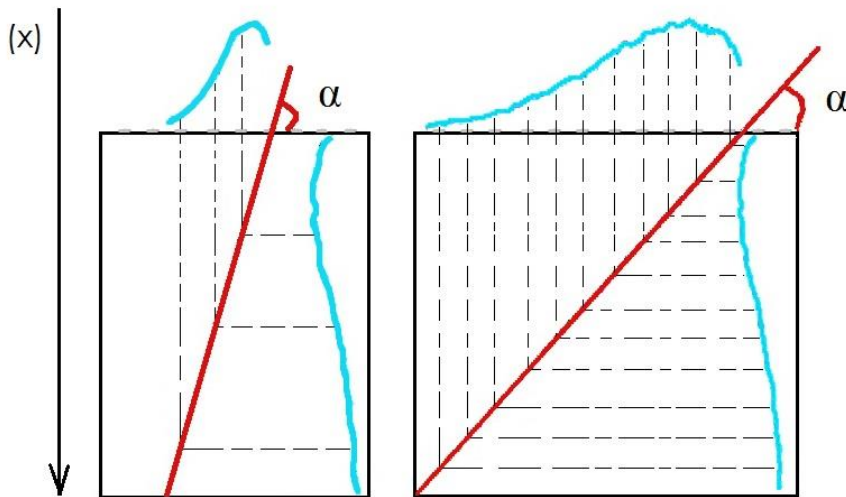


Figure 7.9 Scheme of charge collection efficiency profile measurement using grazing particles

Once defined the technique to measure the CCE profile, we are going to study the CCE profiles and some basic transport parameters extracted from these profiles for: RAPS03 ESAS and ESAL sensors, Micron MT9V011 and Micron MT9V032 sensor. The first three sensors have been already presented in the former

chapters; the MT9V032 sensor is similar to the MT9V011 but it features an epitaxial layer of $12\mu\text{m}$ instead of $4\mu\text{m}$.

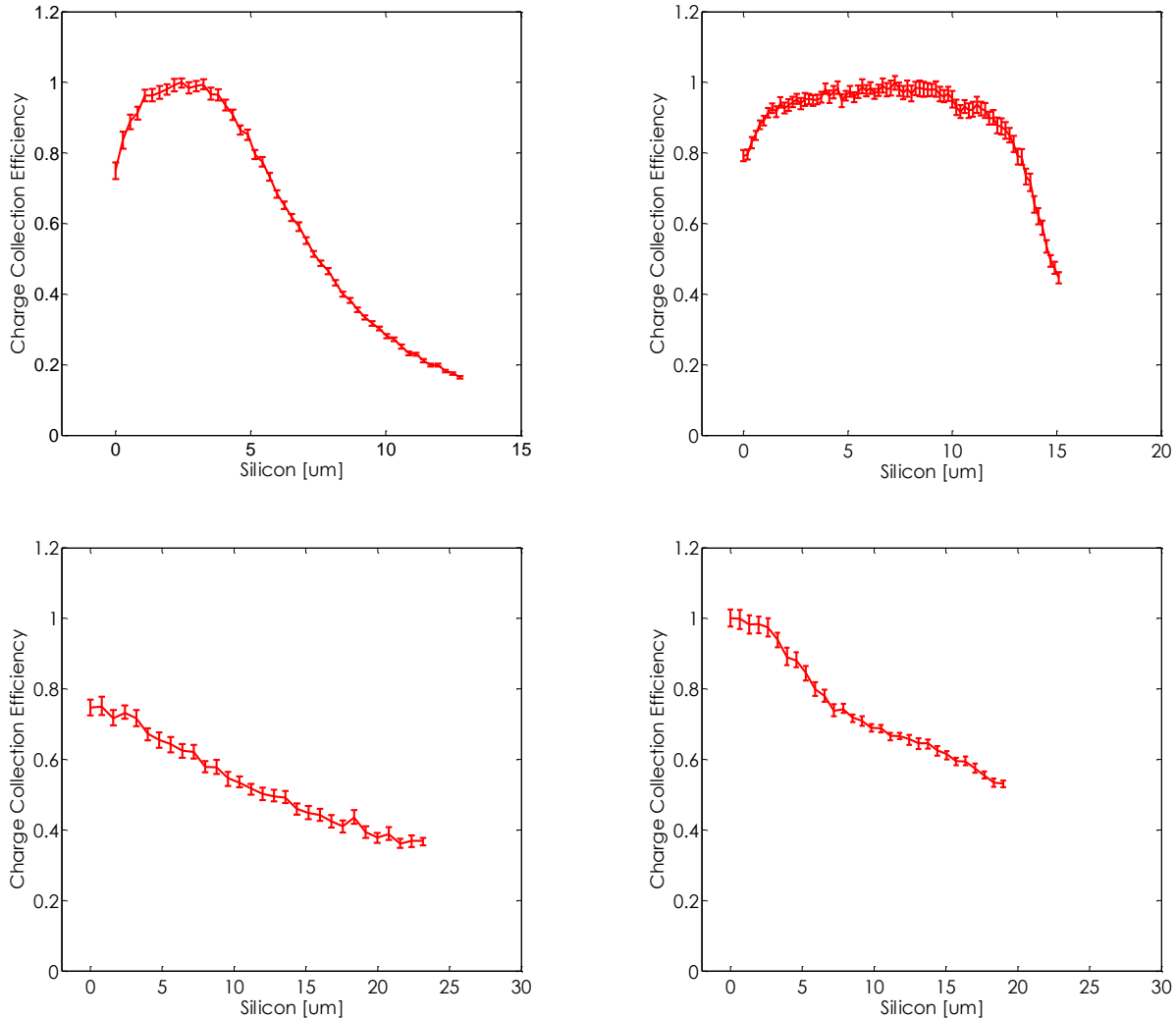


Figure 7.10 Experimental Charge Collection Efficiency profile related to: (top left) MT9V011, (top right) MT9V032, (bottom left) ESAS RAPS03, (bottom right) ESAL RAPS03.

The experimental CCE profiles for the four CMOS sensors are shown in Figure 7.10. The CCE profiles are normalized to the most probable signal expected for an ionizing particle traversing the calculated length of silicon [7.8]. Going from the surface toward the bulk (from the left side to the right side of Figure 7.10), we can roughly consider three different regions in the sensors, especially for those featuring the epitaxial layer:

- A. A heavily doped n^+ region where the low electric field and the low lifetime of the carriers due to the high doping and to the presence of the p -wells hosting the pixel transistors prevent carriers from being completely collected.
- B. A region where the collection efficiency is about 100% due to the presence of the depletion region of the pixel sensitive area. In this region the electric field is high and the carrier velocity can be close to saturation. This means that all the carriers within this region cross the region itself since the drift time is much shorter than minority carrier lifetime.

C. A region, localized in the bulk p-doped zone, where the collection efficiency is exponentially decaying. In this region the carrier transport is dominated by the diffusion mechanism. Charge carriers generated within this region, where no electric field occurs, diffuse toward the depletion region.

The region A is appreciable only for the two Micron sensors, due to the peculiar pinned diode doping profile (*pn*). This effect does not occur in the RAPS03 sensors, which features standard (*n+np*) doping profile related to the sensitive regions (photodiodes).

The region B occurs mainly in the Micron sensors, due to the presence of the epitaxial layer and to its low doping concentration; actually, in this region most of the charges generated are completely collected and a plateau in the CCE profile comes out. The thickness of this region is completely comparable to the nominal thickness of the epitaxial layer given from the Micron datasheets. A region with complete charge collection does not appear clearly for RAPS03 sensors. The ESAL sensor, taking advantage of a larger *n+* well and of an higher electric field with respect to the ESAS sensor, shows CCE values close to 100% in the region just below the photodiode. The ESAS is not able to efficiently collect all the charge and hence for all the depths shows an incomplete CCE due to the recombination process which involves the minority carriers.

Eventually, the C region is common to all the four sensors. The CCE tends to decrease because the deeper generation point and the consequent greater recombination probability, so that less electrons will reach the photodiode. The interpretation of such curves is based on the extension of Ramo's theorem as applied to induced charge in semiconductor detectors [7.9].

The excess (Δn) of minority carriers (electrons) generated in the C region by the incident particle is given by

$$\frac{\partial \Delta n}{\partial t} = D_n \frac{\partial^2 \Delta n}{\partial x^2} - \frac{\Delta n}{\tau_n} \quad (7.5)$$

where D_n is the electron diffusion coefficient and τ_n is the carrier lifetime. The boundary conditions state that Δn is zero at the edge of the depletion region ($x=w_2$) and at the back electrode ($x=D$). The initial condition states that $\Delta n=N\delta(x-x_0)$ at $t=0$ where δ is the Dirac's delta function and N the electron/hole pairs generated by a single particle at a distance x_0 from the top electrode.

The solution of Eq. (7.5) is then given by [7.10]:

$$\Delta p(x,t) = N \frac{\exp[-t/\tau_n]}{2\sqrt{\pi D_n t}} \times \left\{ \exp\left[-\frac{(x-x_0-w_2)^2}{4D_n t}\right] - \exp\left[-\frac{(x+x_0+w_2)^2}{4D_n t}\right] \right\} \quad (7.6)$$

and the current j entering the depletion region is

$$j(x = w_2, t) = D_n \left. \frac{\partial \Delta n}{\partial x} \right|_{x=w_2} = N \frac{\exp[-t/\tau_n]}{2\sqrt{\pi D_n t^3}} \exp\left[-\frac{(x_0 - w_2)^2}{4D_n t}\right] \quad (7.7)$$

Supposing that all the carriers entering the depletion layer are totally collected the induced charge at the electrodes is given by:

$$\begin{aligned} q(x_0, t) &= A \int_0^t j(w_2, t') dt' = \\ &= \frac{N}{4} \left[2 \cosh\left(\frac{x_0 - w_2}{L_n}\right) - \exp\left(\frac{x_0 - w_2}{L_n}\right) \times \operatorname{erf}\left(\frac{x_0 - w_2}{2L_n} \sqrt{\frac{\tau_n}{t}} + \sqrt{\frac{t}{\tau_n}}\right) \right. \\ &\quad \left. - \exp\left(-\frac{x_0 - w_2}{L_n}\right) \times \operatorname{erf}\left(\frac{x_0 - w_2}{2L_n} \sqrt{\frac{\tau_n}{t}} - \sqrt{\frac{t}{\tau_n}}\right) \right], \end{aligned} \quad (7.8)$$

where A is the electrode area, $L_n = \sqrt{D_n \tau_n}$ the electron diffusion length and $\operatorname{erf}()$ is the error function. If the integration time of electronic read-out chain is much longer than the electron lifetime, the induced charge measured at the electrode as a function of the incident particle position is

$$q(x_0) = N \exp\left(-\frac{x_0 - w_2}{L_n}\right) \quad (7.9)$$

The charge collection efficiency is then an exponentially decaying function with the distance between the generation point (x_0) and the edge of depletion layer (w_2). The theory, just briefly recalled, explains all the features of the experimental profiles as shown in Figure 7.11.

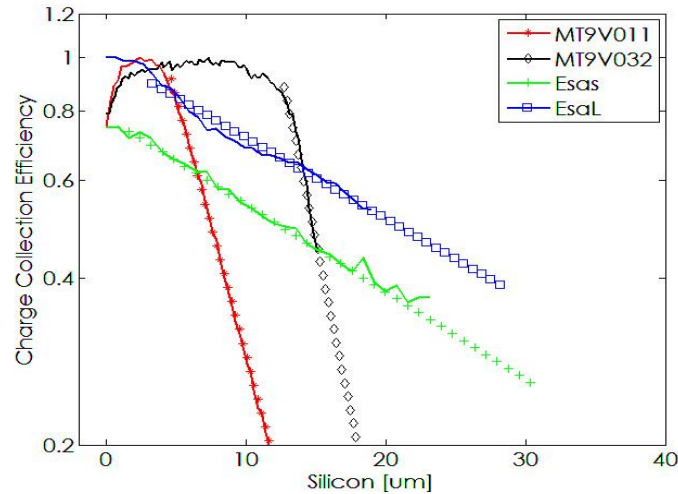


Figure 7.11 Charge collection Efficiency profile of four sensors (dots) with related exponential fits (continues lines)

From Figure 7.11 it is clear how the two RAPS03 sensors are able to collect charge at greater depth with respect to the two Micron sensors. This is due most likely to the lower substrate doping concentration of the RAPS03.

The exponential tail can be fitted with the function described by Eq.(7.9). The fitting procedure gives for the Micron sensors MT9V011 and MT9V032 respectively a minority diffusion length value in the sensor substrate of $4.6 \pm 0.2 \mu\text{m}$ and $3.5 \pm 0.5 \mu\text{m}$ while for the ESAS and ESAL sensors those values are equal to $27.8 \pm 1.1 \mu\text{m}$ and $29.1 \pm 2.1 \mu\text{m}$, respectively.

We have checked that the extracted value of the minority diffusion length does not change as a function of the thickness of the region which we use for the fit. If we assume an electron diffusion coefficient in the substrate equal to $36 \text{ cm}^2/\text{s}$, the effective electron lifetimes for the MT9V011 and MT9V032 read to $5.9 \pm 0.1 \text{ ns}$ and $3.4 \pm 0.2 \text{ ns}$ while for ESAS and ESAL read to $214 \pm 0.4 \text{ ns}$ and $230 \pm 1.2 \text{ ns}$. It is worth noting that the integration times of the electronic read-out circuit used in this work are much longer than the carrier lifetime.

The minority carrier diffusion length measured with this method appears in good agreement with the other results showed in the former chapters. In particular, an equivalent collecting charge thickness has been measured for MT9V011, ESAS and ESAL sensors, reading values of $5.7 \pm 0.7 \mu\text{m}$, $22 \pm 1 \mu\text{m}$ and $38 \pm 7 \mu\text{m}$ respectively. However this thickness should not be simply considered as the collection depth of the chip beyond which the photodiode is no longer able to collect; it can be only asserted that this kind of sensors, from the point of view of the ability to collect the charge, can be compared to an ideal (i.e. fully depleted) detector which is able to collect all the charge deposited within this thickness.

Table 7.1 Sensor results

Sensor Name	Region with maximum CCE	Diffusion Length	Lifetime
<i>MT9V011</i>	4 μm	$4.6 \pm 0.2 \mu\text{m}$	$5.9 \pm 0.1 \text{ ns}$
<i>MT9V032</i>	12 μm	$3.5 \pm 0.6 \mu\text{m}$	$3.4 \pm 0.2 \text{ ns}$
<i>ESAS RAPS03</i>	Not defined	$27.8 \pm 1.1 \mu\text{m}$	$214 \pm 0.4 \text{ ns}$
<i>ESAL RAPS03</i>	2 μm	$29.1 \pm 2.1 \mu\text{m}$	$230 \pm 1.2 \text{ ns}$

7.1.2 Grazing angle method for the sensitive region thickness measurement

In order to estimate the thickness of the sensitive region of the MT9V011 pixel sensor and validate the measurements shown in the former paragraph, another technique has been developed.

By varying the inclination of the sensor with respect to the direction of the incident beam, from simple geometrical considerations (see Figure 7.2(a)), it is possible to define the extension of the sensitive region of the sensor. Estimating the average length R of the detected traces at a defined angle α we have that:

$$d = R \tan(\alpha) \quad (7.10)$$

where d is the sensitive region of the sensor.

In Figure 7.12 the track length distribution, measured with the MT9V032 sensor, for two different values of α is plotted. In both figures a Gaussian distribution appears; the mean value represents the average track length R while the sigma represents the accuracy of the measurement. At low value of α the Gaussian distribution tends to have a higher standard deviation and the measurement of the average track length becomes very difficult.

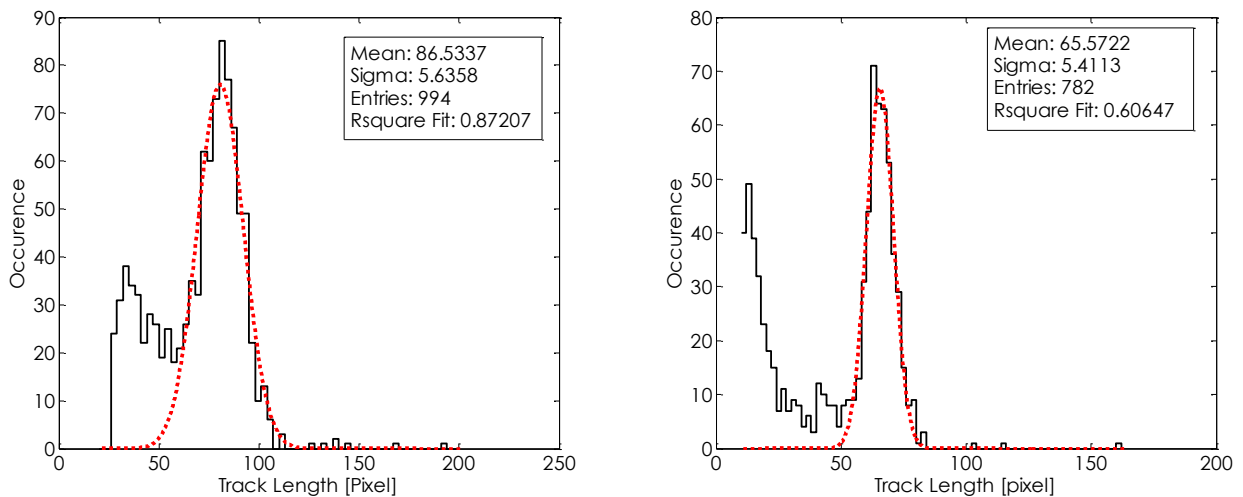


Figure 7.12 Track length distribution for two different incident angles: (a) -1° and (b) $+3^\circ$.

Other measurements, with other value of α , for the MT9V011 and MT9V032 sensor have been carried out and are shown in Figure 7.13, where the average track length has been plotted as function of the α angle. Overlapped to the experimental data there is a fit according the function $|d/\tan(x+offset)|$ where d represents the sensitive thickness and $offset$ is the difference between the beam direction and the tilt angle when α is put in the nominal zero position. Each point used for the fit procedure has been weighted according the standard deviation of the Gaussian distribution, minimizing the measurement uncertainties.

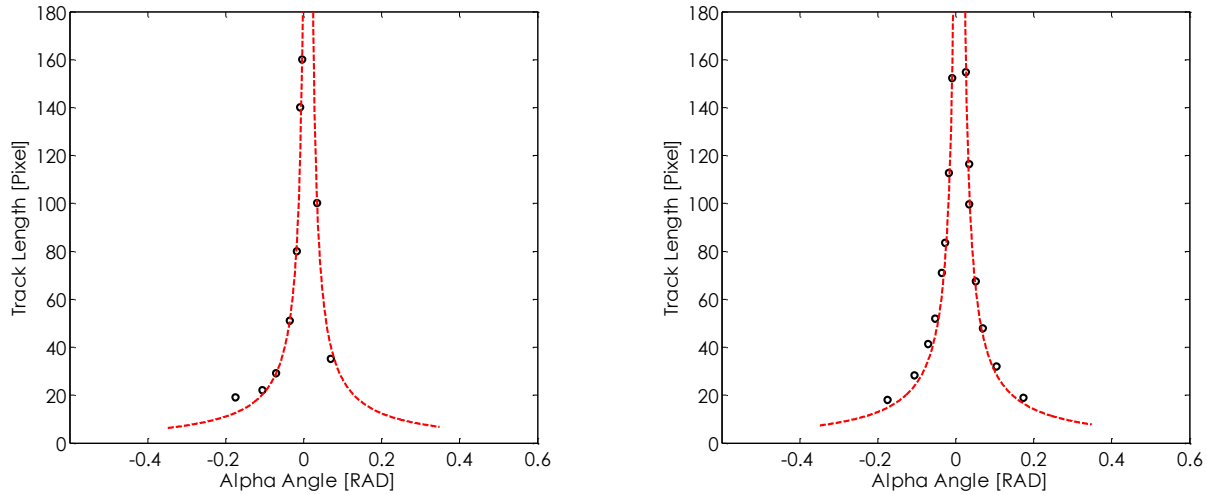


Figure 7.13 Track length as function of the α angle for the (a) MT9V011 and (b) MT9V032

For the sensor MT9V011 the value of d is $12.8 \pm 1.1 \mu\text{m}$ while the estimated *offset* is $10 \pm 1.8 \text{ mRad}$. For the MT9V032 the value of d is $15.4 \pm 0.4 \mu\text{m}$ while the *offset* is $8 \pm 0.5 \text{ mRad}$. The sensitive thickness measurements achieved with this technique are comparable with the ones showed in the former paragraph (see Figure 7.10), confirming the accuracy of our setup and the validity of grazing angle approach to perform this kind of measurements.

7.1.3 Grazing angle method for energy loss measurement

In the future, the requirements for particle tracking systems will be even more stringent, in particular in terms of low material budget [7.11]. The reduction of the detector thickness decreases the signal rise time, increases the radiation resistance and reduces the material budget and the associated multiple scattering effects. Therefore it is important to investigate the energy loss distribution $f(\Delta)$ due to the passage of ionizing particles through thin layers of matter. To accomplish the $f(\Delta)$ measurement, the charge generated by ionizing particles crossing a silicon layer of known thickness is collected and measured. To perform a comprehensive study, a large number of detectors, each one with different thickness, is needed. This procedure is intrinsically time-consuming and very difficult to accomplish, especially for small thicknesses.

In this paragraph a new method to accomplish the $f(\Delta)$ measurement for several silicon's thicknesses, relying only on one CMOS pixel sensor in a grazing angle configuration has been developed [7.12]. With this configuration, the passage of a charged particle is detected by several pixels pertaining to the single planar detector by forming a track (see Figure 7.2). The amount of silicon crossed by the ionizing particle is a function of the particle incident angle ($R=d/\tan(\alpha)$), allowing to perform the $f(\Delta)$ characterization at various thicknesses just selecting tracks of different length (detected by the sensor).

The commercial Micron MT9V011 sensor featuring $5.6 \times 5.6 \mu\text{m}^2$ pixel size and few micrometers epitaxial layer has been used to perform the measurements.

The only region used in the investigation of the $f(\Delta)$ is the one ranging from $1 \mu\text{m}$ to $3.5 \mu\text{m}$ in depth (the

B region in Figure 7.14), where almost all the generated electron-hole pairs are collected. Because the generation point in this region is close to the photodiodes, the charge diffusion is limited and the charge sharing among pixels belonging to the same track is negligible.

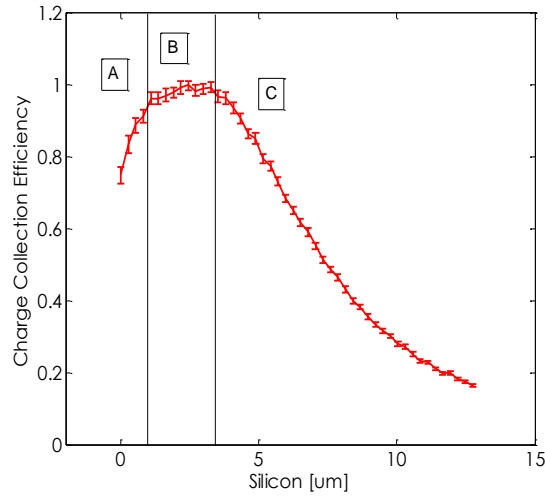


Figure 7.14 CCE profile of the MT9V011, sensor used for the energy loss investigation

Tracks with different pixel length can be used, knowing that for a longer track there will be more pixels in the B region and then more crossed pixels at maximum CCE. Selecting segments with a different number of pixels it is then possible to build an energy loss function for several silicon thicknesses.

In the present study, energy loss distributions were obtained for 100 MeV electrons and 12 GeV protons. Due to the particle energy used in our investigation, the value of k will be always less than 0.01. Consequently, the observed energy loss distributions are expected to be well represented by Eq. (2.19), in which a Gaussian function convolves a Landau distribution. The standard deviation σ_{tot} of the Gaussian part should take into account also the detector and electronic noise σ_{noise} :

$$\sigma_{tot}^2 = \sigma_{noise}^2 + \delta_2 \quad (7.11)$$

Therefore, the experimental energy loss distributions for each momentum and type of particle were fitted to the Landau convolved with a Gaussian with three free fitting parameters: σ_{tot} , ξ and LA_p .

In Figure 7.15 are shown the energy loss distributions for 12 GeV protons and 100 MeV electrons passing through 5.6 μm of silicon.

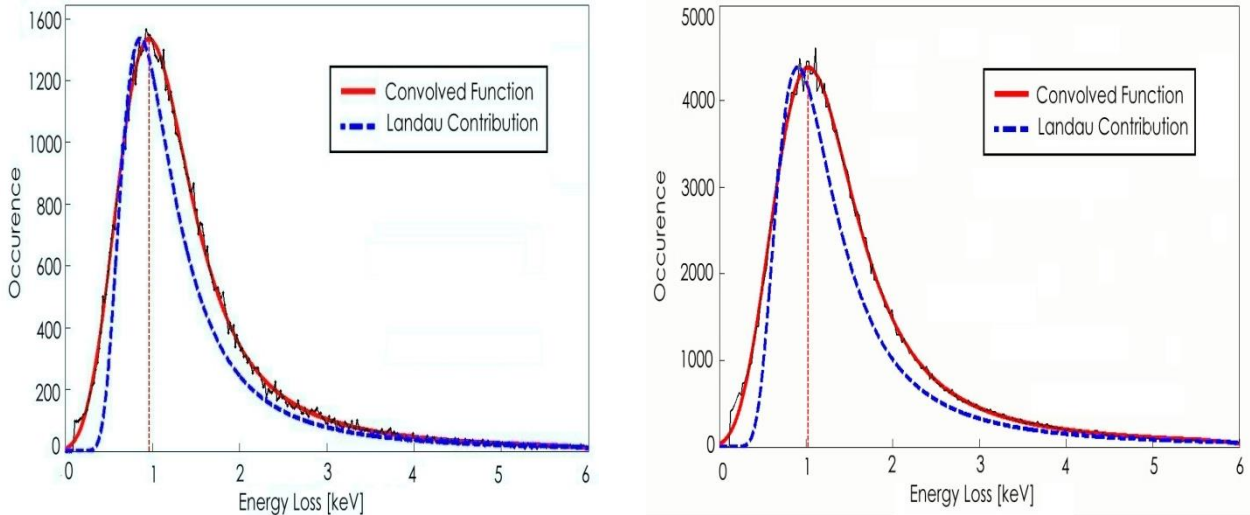


Figure 7.15 Energy loss distribution for (a) 12 GeV protons and (b) 100 MeV electrons passing through 5.6 μm of silicon with convolved function fit and Landau contribution of this fit.

Superimposed on the experimental data are the energy loss distribution fitted using a convolved function according to Eq. (2.19) and a Landau distribution extracted from this fit. Both figures show the importance of electronic binding effects, which tends to broaden the energy loss distribution.

The Δ_p is equal to 0.966 ± 0.035 keV for the 12 GeV protons and 1.018 ± 0.050 keV for 100 MeV electrons, corresponding to 262 ± 10 and 277 ± 14 electron-hole pairs. The extracted value for w is 1.04 ± 0.012 keV for the protons and 1.12 ± 0.018 keV for the electrons while the value for δ_2 is 0.27 ± 0.18 keV for the protons and 0.31 ± 0.23 keV for the electrons.

The shift of the most probable energy loss of the straggling function (Δ_p) respect to ${}_L\Delta_p$ is about 12%. The Landau fit fails to correctly model these experimental data because the theory of Landau assumes that the typical energy loss in an absorber should be large compared to the binding energy of the most tightly bound electron, a condition which is not satisfied for this thickness. In fact for the validity of the Landau approach, ζ should be much more than the atomic binding energy, which means $x/\beta^2 \gg 100 \mu\text{m}$.

Varying the thickness of the silicon absorber the distributions change noticeably. In Figure 7.16(a) are shown several energy loss distributions obtained for 12 GeV protons in silicon absorbers of different thickness. For each distribution, the fit using Eq. (2.19) reproduces well the experimental data.

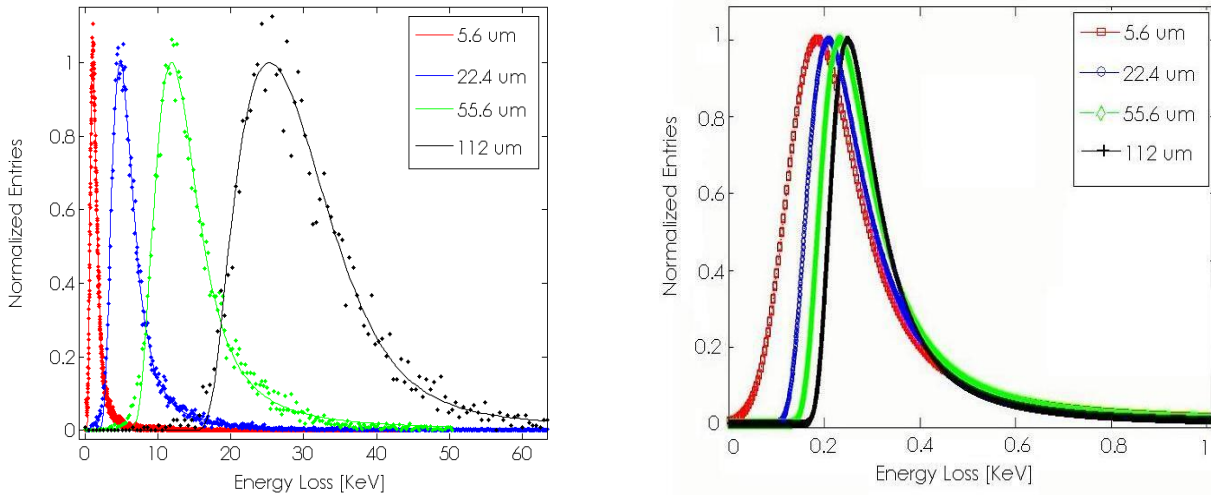


Figure 7.16 (a) Energy loss distributions with fits for 12GeV protons passing through several silicon thicknesses. (b) Fit to energy loss per unit length distribution for 12 GeV protons passing through several silicon thicknesses.

To better understand the Δ_p dependence from the thickness of crossed silicon, in Figure 7.16(b) are shown the fits obtained from several distributions of the energy loss per unit length of crossed silicon. The position of the peak of the normalized distributions tends to increase with the silicon thickness, while the distribution broadens for thinner layers. In fact, for small values of k , the Landau width w_L is proportional to the thickness while the width of the convolution Gaussian δ_2 is proportional to $\sqrt{\text{thickness}}$.

In Figure 7.17 the Δ_p/x as a function of the silicon thickness for respectively 12 GeV protons and 100 MeV electrons is plotted. The circles represent the measured values Δ_p/x with their error bars coming from the peak error of the energy loss fit, while the line represents a logarithmic fit performed on these data according the Eq. (2.19). A very good agreement could be observed in all the studied range (5.6 to 120 μm).

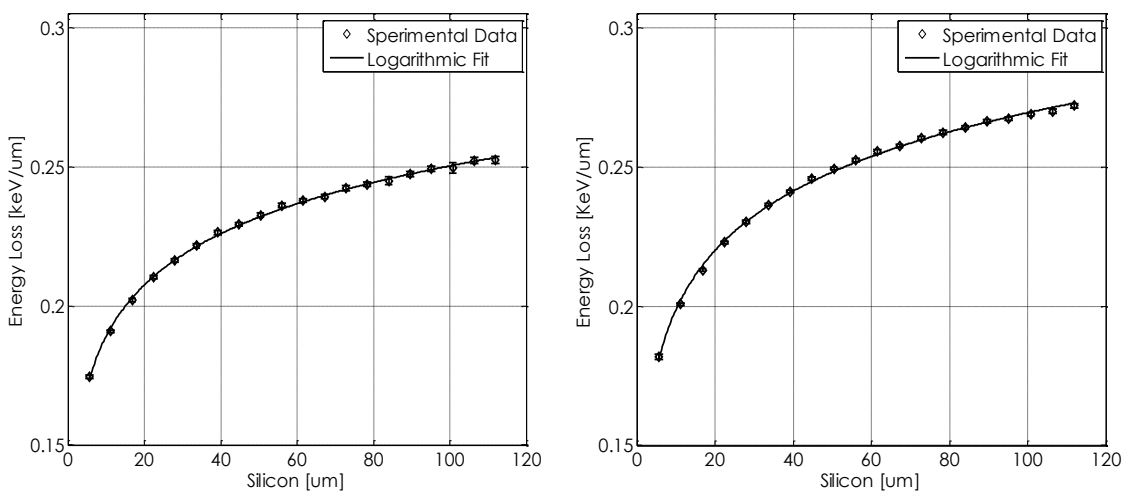


Figure 7.17 Energy loss for (a) 12 GeV protons and (b) 100 MeV electrons passing through several silicon thickness

In Table 2 we compare the results for specific values of silicon thickness with theoretical predictions and other experimental measurements. The data obtained with the grazing angle method, using 12 GeV proton

($\beta\gamma = 12.3$), are compared with experimental data reported in [7.13] obtained using pions having a $\beta\gamma$ equal to 14, and with theoretical data reported in [7.14] obtained by the convolution method for highly relativistic particles.

Table 7.2. Comparison between our results obtained with 12 GeV protons and other experimental and theoretical results.

x [μm]	32	51	100
Δ_p [keV] this work	7.04	11.81	24.75
Δ_p [keV] theoretical [7.14]	7.092	11.840	25.283
Δ_p [keV] experimental [7.13]	6.91	11.79	25.96
Δ_p/x [e-h/ μm] this work	60	63	67
w [keV] this work	4.98	7.22	13.17
w [keV] theoretical [7.14]	5.172	7.201	12.929
w [keV] experimental [7.13]	5.26	7.25	13.29
σ_{noise} [keV] this work	0.14	0.16	0.23
σ_{noise} [keV] experimental [7.13]	0.78	0.73	2.0

The general observation is that the results obtained through the grazing angle method closely follow the experimental data and agree with the predicted values within the experimental errors. The small Gaussian error σ_{noise} due to the electronic and sensor characteristics allows a precision in the experimental measurements significantly better than the other methods.

7.1.4 Grazing angle method for spatial resolution measurements

To measure the intrinsic spatial resolution of silicon pixel sensor is usually a non trivial task, especially if small pixel sizes are involved and hence the multiple scattering may be the limiting factor. In this paragraph we outline a new measurement method to put upper limits to the intrinsic spatial resolution of a silicon pixel device. The method relies on the capability of the device, hit by a charged particle incoming at a grazing angle, to record the passage of the track over several tens or hundreds of pixels. The track will then be fitted and the residuals of the fit will give an estimate of the intrinsic spatial resolution.

The lower limit on the achievable spatial resolution, in case of binary read-out and signal collected by just one pixel, is given by:

$$\sigma_1 = \text{pixel size} / \sqrt{12} \quad (7.12)$$

To obtain a lower spatial resolution, the information on the signal collected by each pixel has then been used (analog read-out) to better reconstruct the impact position of the charged particle on the pixel, either via the Center of Gravity method than with more sophisticated algorithms.

The extraction of the sensor intrinsic spatial resolution using the telescope method, presents several difficulties, especially if a resolution of the order of $\sim \mu\text{m}$ or less is expected (less than 10 μm pixel size).

Just to name the most important factors to be taken into account:

- multiple scattering of single charged particle;

- intrinsic spatial resolution of the telescope points;
- telescope particle finding efficiency;
- telescope geometrical acceptance;
- enough valid triggers (possibly millions) to align the DUT and the telescope to correct, within small errors, for offsets and relative angles.

The general expression for the width of the residual distribution is:

$$\sigma_{Residual}^2 = \sigma_{Intrinsic}^2 + \sigma_{MultipleScattering}^2 + \sigma_{Telescope}^2 \quad (7.13)$$

The minimization of the multiple scattering term has a direct consequence on the type and energy of the beam to be used. Charged particle beams with hundreds GeV momentum are needed, but they are available just in few places in the world, and the beam intensity reduces with the beam momentum. To minimize the telescope term instead, detectors with small intrinsic spatial resolution, and a long lever arm are needed. The last requirement will however reduce the solid angle acceptance and hence the trigger rate, while the precision of the predicted position should be at least of the same order of magnitude of the one measured by the DUT.

In this work we have used a method based on grazing angle charged particles to reduce the multiple scattering effects, to use medium momentum beams (from 100 to 500 MeV electrons) and to avoid the use of a telescope with all the associated analysis complications.

Let's now discuss the relation between the track position in our setup and the intrinsic spatial resolution of the sensor, considering a 3x3 pixels submatrix. The intrinsic spatial resolution is usually measured from the response of the 9 pixels to a track perpendicular to the sensor surface, passing inside the central pixel. The signals collected by the different photodiodes hence depends on the position of the incident particle on the pixel surface and on the charge generation along the track.

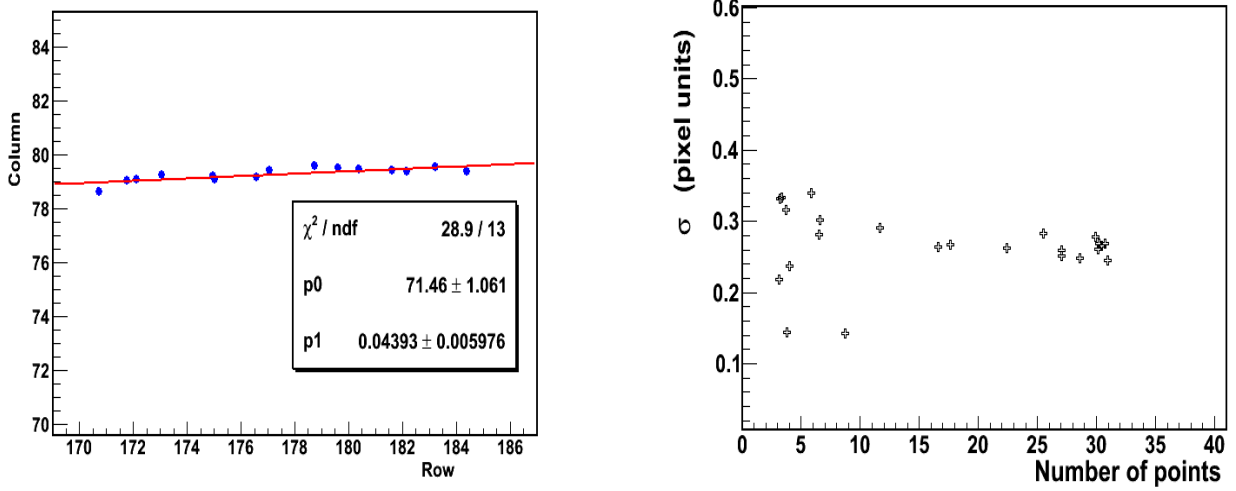


Figure 7.18 (a) Single track recorded by a sensor with superimposed a linear fit. (b) Dependence of σ from the number of points used in the fit, when the track length remain constant (140 pixels in this case).

If we switch to our setup, due to the limited thickness of the sensitive region, it is possible to consider each pixel as a parallelepiped, with the three edges roughly of the same dimensions. Hence if we have tracks almost parallel to one of the coordinates (row or column) the track will cross each sensitive volume approximately at the same depth (see Figure 7.2) and at the same position along the other matrix coordinate (column or row). So the same charge sharing mechanism will be working. It is then possible to obtain, for each coordinate (pixel) along the track direction, the measured coordinate in the other axis, using the Center of Gravity. The track could then be described using the Eq. (7.14), where y_i and x_i are respectively the column and row coordinates of each track point and ε_i collects all the possible error sources. For each track it is then possible to apply a linear fit to extract its parameters and the corresponding errors (Figure 7.18(a)).

$$y_i = Ax_i + B + \varepsilon_i \quad (7.14)$$

The errors on the fit parameters, on the hypothesis that all the errors on the y_i measurements belongs to the same distribution, are linked to the average variance of the set of track points by the relations:

$$\sigma^2 = \sum (y_i - Ax_i - B)^2 / N \quad (7.15)$$

The variance of the set of the track points sums up several potential contributions, among which: the intrinsic resolution of the sensor, the multiple scattering effects, the number of track points.

$$\sigma^2 = \sigma_{Intrinsic}^2 + \sigma_{MultipleScattering}^2 + \sigma_{Fit}^2 \quad (7.16)$$

The term due to the fit uncertainty in principle should decrease with the number of points used, while the multiple scattering term should increase with the number of points, due to the thicker material crossed by the particle. The intrinsic resolution term will also depend on the number of points because of the different charge collection efficiency at different generation depths, even if it not so clear in principle how the

dependence will go. We could expect a minimum in σ as a function of the number of points used to define the track.

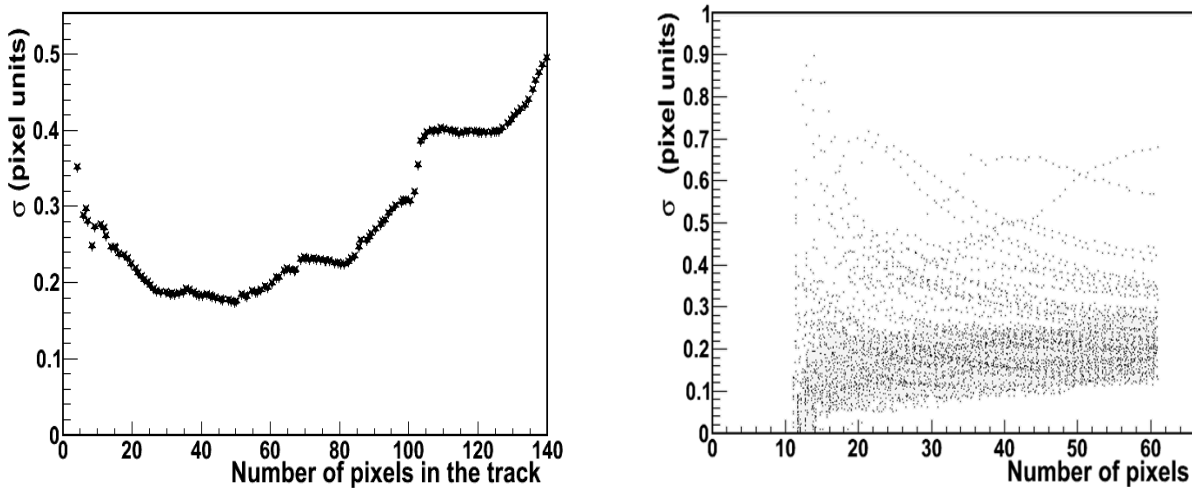


Figure 7.19 (a) Evolution of the σ for a single track as a function of the number of pixels used. (b) Evolution of the σ for a set of tracks of 140 pixel length, as a function of the number of pixels used for the fit; the first pixel is the pixel on the sensor surface.

Let's now discuss the importance of the fit uncertainty. We are using a typical track of 140 pixel length to discuss how σ varies if we use a different number of points for the fit. The thickness of the silicon traversed by the particle will remain the same, to allow the same multiple scattering effect, while the number of points to be used in the fit will vary from the total number of pixels to just a fraction, taking care of using always the first and last points of the track. In Figure 7.18(b) is shown the variation of σ . If we choose a number of points greater than 20-30, there is essentially no dependence on the number of points used for the fit, being the variation of the fit results quite small.

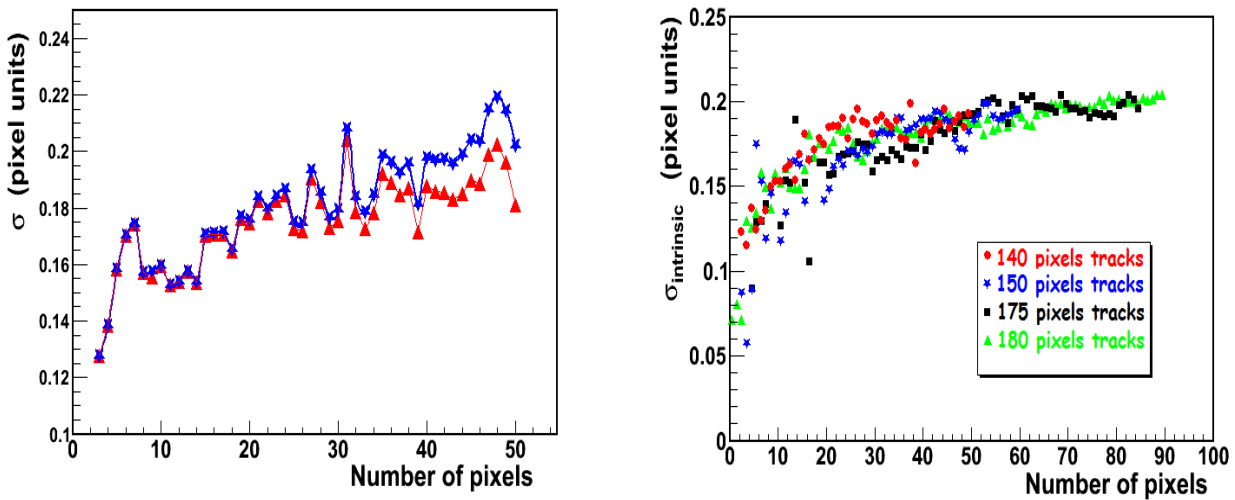


Figure 7.20 (a) Evolution of s as a function of used track length with (blue stars) and without (red triangle) multiple scattering contributions. (b) σ evolution for 4 sets of track having different length after subtraction of multiple scattering effects.

Concerning the multiple scattering issue, using a set of 140 points track we have built the distribution of the σ as a function of the track length starting from the first 5 pixels near the sensor surface, and extending the track inside the silicon bulk up to the entire track length (Figure 7.19(a)). The presence of the

minimum suggest to use for the analysis only the pixels in the range 10-60, to avoid the region too close to the surface, and to choose the maximum charge collection efficiency region. In Figure 7.19(b) is shown the superimposition of the σ evolution of several tracks having the same length. There is a trend toward the stabilization of the σ and the reduction of its spread as the number of pixels used increase.

Now we can subtract the multiple scattering contribution for each track length to evaluate the upper limit of the intrinsic spatial resolution of the sensor; in Figure 7.20(a) is shown the evolution of the σ with (blue stars) and without (red triangles) the multiple scattering contribution. The flattening of the curve at higher thicknesses of crossed silicon is an index that most of the effects have been removed.

In Figure 7.20(b) is shown the σ evolution after the multiple scattering subtraction for 4 sets of track with different length (140, 150, 175 and 180). The evolutions superimpose well demonstrating that the results do not depend on the specific set of tracks used.

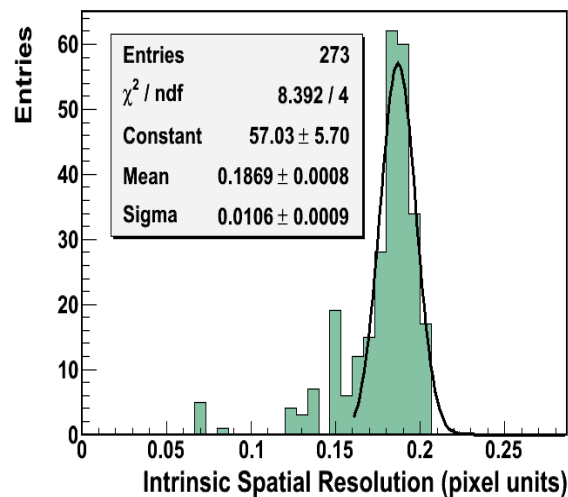


Figure 7.22 Distribution of the σ after subtraction of multiple scattering effects.

In Figure 7.22 is finally shown the distribution of the σ after the correction for multiple scattering effects; the superimposed Gaussian fit allows to find the estimated intrinsic spatial resolution of the sensor which reads 0.187 ± 0.011 pixel unit, value which for the MT9V011 sensors means an upper limits to the intrinsic spatial resolution measurement of $1.04 \pm 0.06 \mu\text{m}$.

References

- 7.1 S. Meroli et al., *A grazing angle technique to measure the charge collection efficiency for CMOS Active Pixel Sensors*, Nucl. Instr. and Meth. A (2010)
- 7.2 D. Passeri, et al. *Tilted CMOS Active Pixel Sensors for Particle Track Reconstruction*, IEEE Nucl. Sci. Symp. Conf. Rec. NSS09 (2009) 1678. July 2006.
- 7.3 M. Mikuz, et al., *Study of anomalous charge collection efficiency in heavily irradiated silicon strip detectors*, Nucl. Instr. Meth. A 636 (2010) 50.
- 7.4 B. Henrich and R. Kaufmann, *Lorentz-angle in irradiated silicon*, Nucl. Instr. and Meth. A 477 (2002) 304.
- 7.5 E. Vittone et al., *Measurements of charge collection profiles in virgin and strongly irradiated silicon diodes by means of the micro-IBICC technique*, Nucl. Instr. Meth. A 476 (2002) 607.
- 7.6 I. Gorelov, G. Gorfine, M. Hoeferkamp, S. Seidel, A. Ciocio, et al., *A measurement of Lorentz angle and spatial resolution of radiation hard silicon pixel sensors*, Nucl. Instr. and Meth. A 481 (2002) 204.
- 7.7 L. Landau, *On the Energy Loss of Fast Particles by Ionization*, J. Phys. USSR 8 (1944) 201
- 7.8 Particle Data Group PDG, *Passage of particles through matter*, Nuclear and Particle Physics, vol. 33, no. 27, pp. 258-270, July 2006.
- 7.9 G. Cavalleri et al., *Extension of Ramo's theorem as applied to induced charge in semiconductor detectors*, Nucl. Instr. and Meth. A 92 (1971) 137.
- 7.10 J.W. Mayer, *Performance of Germanium and Silicon Surface Barrier Diodes as Alpha-Particle Spectrometers*, J. Appl. Phys. 30 (1959) 1937.
- 7.11 SUPERB collaboration, *The SuperB silicon vertex tracker*, PoS(RD09)038.
- 7.12 S. Meroli, D. Passeri and L. Servoli, *Energy loss measurement for charged particles in very thin silicon layers*, 2011 JINST 6 P06013.
- 7.13 J.F. Bak et al., *Large departures from Landau distribution for high-energy particles traversing thin Si and Ge targets*, Nucl. Phys. B 288 (1987) 681.
- 7.14 H. Bichsel, *Straggling in thin silicon detectors*, Rev. Mod. Phys. 60 (1988) 663.

Conclusion

This PhD work has been focused on the characterization of several classes of pixel detectors and on their use for precision measurements. Several classes of pixel detectors have been successfully tested, demonstrating their capability of detecting charged particles and x-rays, even if some were not designed for this purpose (the Micron CMOS imagers). For all detectors a complete characterization has been carried out: noise analysis, calibration with fluorescence x-rays, charged particles response. An extensive analysis of the SNR, spatial resolution and charge collection efficiency have been carried out exploring, from the statistical point of view, the implications of different analysis procedures.

The CMS Hybrid Pixel Detectors have been tested using the standard test and calibration procedures and algorithms to extract the calibration parameters necessary to successfully operate them. A functional test setup has then been implemented and will be used to qualify all the pixel barrel modules needed for the upgrade of the CMS Pixel Detector after the coming long shut down of LHC.

The possibility to use MAPS detectors fabricated with a standard CMOS process for implementing a high precision system for charged particle detection has been studied using a prototype detector RAPS03 realized in a non epitaxial CMOS technology. This monolithic pixel detector allows a very precise determination of the spatial position of the charged particle, and the integrated read-out electronic on the same substrate of the sensitive volume allows a reasonable SNR even if the sensitive thickness is much reduced respect to the standard Hybrid Pixel Detectors. The measured experimental performances show a remarkable intrinsic spatial resolution for MIP (order of 1 micrometer), needed for a subsequent good pattern recognition, required in most of the future tracking applications. There are further studies needed, like the radiation damage and the acquisition rates for large systems, but the achieved results are promising.

Commercial CMOS imagers from Aptina Technology, based on the epitaxial layer technology have been studied as ionizing radiation detectors. Some remarkable results have been obtained: $\text{SNR} \geq 30$, efficiency close to 100% with very small fake hit probability, small pixel occupancy (~ 5). The soft x-ray detection is also very good with energy resolution ($\sim 4\%$) and sensitivity (≥ 1 keV). We conclude that commercial imagers could be a very interesting option to be considered at least for some applications where the radiation damage or the read-out speed are not crucial.

The last prototype sensor studied is RAPS04, a stack of two MAPS layers, connected via the 130 nm 3D-IC Chartered/Tezzaron technology. The detector concept has been simulated and, despite several problems to obtain the chip from the foundry, some characterization has been obtained.

The importance of redundant interconnection schemes between the two layers has been recognized after the misalignment in the superposition of the two layers. Both tiers are fully functional: different test structures and matrix structures have been characterized. Clear coincidence responses between bottom and top matrices have been obtained with laser stimuli and 3 MeV protons; an x-y misalignment between top and bottom tiers between 10 μm and 20 μm (depending on the direction) has been estimated. By means of 3 MeV protons has been possible to estimate the thickness of the sensitive area and the SNR expected from a MIP. Encouraging results have been found, fostering the suitability of the adopted 3D-IC vertical scale fabrication technology and of the proposed approach for particle tracking applications. Using these silicon pixel detectors precision measurements of the interaction between radiation and matter have been performed. An innovative method, with the sensor parallel to the particles beam, has been developed and tested in order to characterize the MAPS and, more generally, silicon pixel detectors. The method has been used to study in detail the charge collection efficiency profile, the energy loss of charged particles in silicon and the mechanism of charge carriers diffusion in silicon.

Very encouraging results have also been obtained on the intrinsic spatial resolution characterization. The grazing angle method allows to extract that value using medium energy charged particle beams, instead of the high energy beams available in few places in the world. A micrometer resolution with the MT9V011 sensors disposed edgewise to the beam has been measured. This result, if validated by a measure in the conventional telescope arrangement, would be a state of the art resolution limit for the solid state detector to be used for the particle tracking.

Finally the most important conclusion of this work is that indeed the pixels sensor concept is a powerful tool to perform precision measurement, even of very basic physics phenomena like ionization mechanisms, while a valuable collateral result is the amount of test infrastructures and procedures developed, that will be very useful in future investigations.